UNIVERSITY OF BIRMINGHAM

# Synthesis of metal alloy nanoparticles by cathodic corrosion and their use in electrochemical oxidation of small organic molecules

Elizabeth Bennett

**Supervisor: Dr P Rodriguez**

**Masters Thesis**

MSc by Research

School of Chemistry, University of Birmingham, Edgbaston, UK, 2015.

# Dedication

I would like to dedicate this thesis to my father Stephen, an engineer. He taught me that hard work is the key to achieving what we want in life and encouraged me to pursue STEM subjects further.

# Acknowledgements

This work would not have been possible without contributions from the following. I would firstly like to thank my supervisor Dr Paramaconi Rodriguez for his guidance, support and the opportunity to carry out this project and publish my first paper.

My regards also go to Javier Monzo for helping me with experimental studies during my research.

On a more personal note, I would like to express my gratitude to my parents Susan and Stephen for their love, encouragement, wise words and belief in me.

# Abstract

The proton exchange membrane fuel cell (PEMFC)[1,2,3] is a type of fuel cell that is commonly used for transport systems along with the direct methanol fuel cell (DMFC).[4,5] PEMFCs are one of the most promising electrochemical devices for energy generation for use in automotive and portable devices. The materials to be discussed in this work were prepared as potential candidates for PEMFC applications.

In this thesis, binary and ternary platinum alloy nanoparticles were applied in different fuel cell reactions with the aim to investigate the effect on activity and stability of the catalysts.

Binary PtBi, PtPb, PtTa and ternary PtRhPd nanoparticles were synthesised via the cathodic corrosion method. It has therefore been demonstrated that cathodic corrosion is an efficient method for preparation of metals,[6] binary[7] and ternary alloys and oxides.[8] Addition of the alloy metal to platinum resulted in a decreased the onset potential, increased the catalytic activity and elevated durability of the catalyst when compared to pure platinum nanoparticles in the PtBi and PtPb catalysts. In particular, the PtBi and PtPb alloy catalysts exhibited extraordinary activity in the formic acid oxidation, whereas the PtRhPd alloy was an effective catalyst towards the electro-oxidation of glycerol showing decreased onset and elevated activity upon addition of the alloy metals.

**Key words:** Alloy nanoparticles, formic acid oxidation, glycerol oxidation, CO oxidation, PtBi, PtPb, PtTa, PtRhPd, cathodic corrosion

# Contents

**Chapter 3: PtBi and PtPb nanoparticles as catalysts in the formic acid oxidation**



**Chapter 4: PtRhPd nanoparticles as catalysts for the glycerol oxidation**



**Chapter 5: Preparation of PtTa nanoparticles**

# List of abbreviations

The following table lists the abbreviations and acronyms used throughout this thesis. For abbreviations that are not in common use, the full term is also mentioned in the text where it is first used.

| Abbreviation | Meaning |
|---|---|
| AC | Alternating current |
| ATR-SEIRAS | Attenuated total reflection-Surface enhanced infrared absorption spectroscopy |
| CA | Chronamperometry |
| CV | Cyclic voltammetry |
| DAFC | Direct alcohol fuel cell |
| DEMS | Differential electrochemical mass spectrometry |
| DFAFC | Direct formic acid fuel cell |
| EDX | Energy dispersive X-ray analysis |
| EELS | Electron energy loss spectroscopy |
| fcc | face-centred cubic |
| GC | Glassy carbon |
| HAADF | High angle annular dark field |
| HOR | Hydrogen oxidation reaction |
| LEIS | Low energy ion scattering |
| OMC | Ordered mesoporous carbon |
| OLEMS | Online electrochemical mass spectrometry |
| ORR | Oxygen reduction reaction |
| PEMFC | Polymer electrolyte membrane fuel cell |
| PVP | polyvinylpyrrolidone |
| RHE | Reversible hydrogen electrode |
| SCE | Saturated calomel electrode |
| SEM | Scanning electron microscopy |
| TEM | Transmission electron microscopy |

| | |
|---|---|
| XAS | X-ray absorption spectroscopy |
| XPS | X-ray photoelectron spectroscopy |
| XRD | X-ray diffraction |
| XRF | X-ray fluorescence |

## Aims of the project

In this thesis, different alloy catalysts are investigated in fuel cell reactions with the aim to elevate the activity and durability of our catalysts compared to pure platinum and the state of the art.

As will be described in Chapters One and Two, there are many challenges in fuel cell research which must be met before their commercialisation can be achieved. Specifically, some of these include the inefficient methods used to prepare the catalysts and the low poison tolerance and resulting hindered activity of these catalysts. The main purpose of this work was to synthesise nanocatalysts with superior catalytic properties and low ease of poisoning by an inexpensive, one-pot method.

As a result of this work, a peer reviewed manuscript was published in ACS Catalysis 2016 6(3), 1533-1539, DOI: 10.1021/acscatal.5b02598. These results are part of Chapter Three.

# Chapter 1

# Introduction to fuel cells and outline

## 1.1 Introduction

Today we are consuming more energy than ever before, with a world population that reached 7.3 billion in mid-2015 and is projected to reach 9.7 billion by 2050,[9] the issue of being able to meet the increasing energy demands becomes more and more significant. The huge consumption of fossil fuels has put strain on resources and led to increased pollution and climate change, both of which have detrimental consequences both to humans and our planet. Fuel cells have the potential to meet these ever growing energy demands with less environmental impact, since they convert chemical energy into electrical energy with virtually no polluting emissions.

Despite the many possibilities of fuel cells, they are still quite far away from commercialisation. The main obstacles in fuel cell research include operation costs, lifetime and efficiency.[1] High operation costs result from the low availability of the platinum metal catalyst along with the purity requirements of the fuel. Where hydrogen is used as a fuel, impurities such as carbon monoxide and sulfur become adsorbed on the surface of Pt, thereby blocking further oxidation of the fuel. This causes the efficiency of the fuel cell to plummet.[10] For these reasons, there is interest in developing new catalysts to resolve these issues. These catalysts must present improved tolerance towards impurities and catalytic poisons and give higher currents at lower onset potentials. Much research is focusing on reducing the loading of Pt. The two ways in which this can be done are by alloying with another metal and preparing catalysts in high surface area nanoscale dimensions.

In this thesis, four sets of non-conventional alloy catalysts were synthesised, characterised and employed in different fuel cell reactions. The focus was mainly on catalytic activity and stability with the wider goal being to obtain knowledge to help further the development of anode catalysts for polymer electrolyte fuel cells. The vast majority of this work was

performed at the School of Chemistry, University of Birmingham. The Electron microscopy analyses and Energy Dispersive X-ray (EDX) analysis were conducted and the School of Materials and Metallurgy and X-ray Photon Scattering (XPS) data was collected at the University of Warwick.

## 1.2 Catalysis

Catalysis is a huge, ever expanding field, with chemists and chemical engineers around the world conducting research to further understand mechanisms of and find new applications in catalysis. The purpose of a catalyst is to provide a reaction pathway with a lower activation barrier than the un-catalysed reaction, with sought after properties of a catalyst being high activity, stability and selectivity.

Catalysis is essential and important to society since we live in a world with elevating energy demands, limited resources and increasing environmental concern caused in part by the careless overuse of raw materials. Wasteful, inefficient stoichiometric processes are constantly being replaced by catalytic routes which are selective to the desired products. In addition to reducing the amount of waste and making processes more efficient and cheaper, catalysts also have roles in pollution control and therefore are vital for both our economy and the environment. The most widely used application of catalysis is the catalytic converter used in cars to reduce the amount of pollutants leaving the engine. Cars emit noxious chemicals with the main pollutants being carbon monoxide, hydrocarbons, sulphur dioxide and nitrous oxides; the latter two are responsible for acid rain and harm to vegetation. These pollutants can go on to react in the atmosphere to produce even more harmful substances such as peroxyacetyl nitrate (PAN), reported to be a lung toxin in a part per billion (ppb) amount. The catalyst for this contains three active metals Pt, Rh and Pd. It is called a three-way catalyst since it converts the three main pollutants (CO, hydrocarbons and NO) into less harmful substances ($CO_2$, $H_2O$ and $N_2$).[10]

Paul Sabatier showed that chemisorption of reactants was fundamental to catalysis, developing the so called Sabatier principle which states that interaction between catalyst and adsorbent should be neither too strong nor too weak. If the interaction is too weak, the substrate will not bind to the catalyst and therefore no reaction can occur. On the other

hand, if the interaction is too strong, the catalyst will become blocked by the substrate.[11] This principle is applied to surface reactions. If we relate this to an 'optimum' catalyst, it will bind species with an intermediate strength. These three basic steps, adsorption, reaction and desorption constitute the general reactions on heterogeneous catalysts, which leads us onto the next section.

### 1.2.1 Heterogeneous Catalysis

Heterogeneous catalysis can be defined as a process in which the catalyst is in a different phase to the reactants. This type of catalysis has been developing since the first reports of a heterogeneous catalytic dehydrogenation from Martinus van Marum and Joseph Priestly.[12] Developments have been made not only in improvements in catalysts and catalytic reactions, but also in unpicking the underlying principles behind such processes. Notable contributions include those from Langmuir for looking into adsorption, Emmett for research into physical adsorption and Rideal, Boudart and Tempkin for work in the field of kinetics, to name a few.[12]

A heterogeneous catalytic process can be broken up into five stages which include the following; diffusion of reactants to catalyst, adsorption of reactants, formation of an adsorbed complex, decomposition of this complex and finally desorption. How exactly the reactants adsorb on the catalyst surface will vary depending on the type of mechanism followed, for example Eley-Rideal or Langmuir-Hinshelwood. Heterogeneous catalysis is a surface science, with reaction taking place at the catalyst surface. This leads us onto the next sub chapter in which this concept is explained.

### 1.2.2 Catalysis on metal surfaces

A surface contains exposed atoms and free bonds which can interact with incoming reactant molecules. The nature of the surface is essential to performance in heterogeneous catalysis and flat surfaces are used widely in investigations concerning surface science.

Some metals are catalytically active for various different reactions; these include most of the transition metal series and the platinum group metals. An important concept of catalysis was put forward by Taylor[13] in 1925 in which he postulated the existence of active sites. He

articulated that a surface contains active centres which make up only a small part of the whole surface, at which adsorption and reaction take place preferentially. Further to this, he suggested that active centres where adsorption occurs are not necessarily always catalytically active.

Experiments using single crystals show that the coordination of a metal centre and surface structure, affects catalytic activity.[14] These materials are used since they have just a single type of surface coordination. Single crystals are usually prepared by growing them from pure metal melt which is then cut to the desired orientation. Of the three low-index planes that platinum has, the (100) usually displays the highest catalytic activity in reactions that result in formation of new bonds or bond cleavage.[15,16] Certain synthesis methods are known to produce Pt nanoparticles with a preferential (100) orientation, (100) sites as high as 59% have been observed in the literature.[15] Certain catalytic reactions are strongly affected by surface structure.[17,18,19,20]

A catalyst's properties may be manipulated for a specific reaction. The catalytic activity of a surface may be changed by poisoning, sintering, dispersion, alloying with another metal and use of a support.[21] For example with poisoning, it is well known that certain impurities inhibit certain reactions on surfaces. Catalytic activity can be hindered in two different ways; the impurity may block the active sites necessary for essential bond breaking reactions or the surface free energy may be lowered.[14] A background on fuel cells will now be given and these points will be referred back to in the discussions about specific types of fuel cells, their efficiency and types of fuel and their oxidation.

## 1.3 Fuel Cells

In this section, a short introduction to fuel cells will be given. This will consist of a short history, some applications and current challenges in fuel cell research. The types of fuel cell to be discussed in this work are the PEMFC, DFAFC and direct glycerol fuel cell (DGFC). The mechanisms of these reactions and state of the art catalysts will be discussed in detail in Chapter 3 (formic acid oxidation) and Chapter 4 (glycerol oxidation).

The first fuel cell was invented by William Grove in 1839.[22] Grove, inspired by the work on electrolysis of water by Nicholson and Carlisle,[23] decided to try the reverse reaction and produce water from hydrogen and oxygen. The principle of a hydrogen-fed fuel cell is illustrated in Figure 1 below.

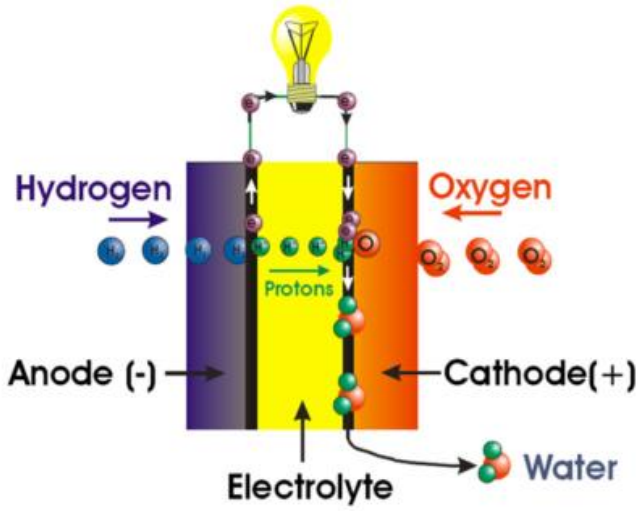


**Figure 1.** Schematic representation of a polymer electrolyte membrane fuel cell.[1]

### 1.3.1 Polymer Electrolyte Membrane Fuel Cells

The history of the fuel cell began with William Grove, back in 1839. He began with improving the electrochemical battery and then went onto build the first working fuel cell, in 1842, to prove his suggestion that since electricity can split water into its constituent elements; it should be perfectly feasible for these elements to recombine to generate electricity. This design contained two strips of platinum metal connected by a wire and partly immersed in sulphuric acid.[24] However, the phrase 'fuel cell' was not invented until later, in 1889, by Ludwig Mond, who, assisted by Charles Langer, used industrial coal gas and air with platinum electrodes in an attempt to engineer the first usable fuel cell. They found difficulty using liquid media and said, "We have only succeeded by using an electrolyte in a quasi-solid form…in a similar way as has been done in the so-called dry piles and batteries".[25] However, their development of a solid electrolyte paved the way for the invention of the membrane in modern PEMFCs.

As far back as the early 19th century, the catalytic properties of platinum were known and it was used to catalyse the ignition of hydrogen. In 1896, after reading about Grove's work, Ostwald commented on this in the journal Electrochemistry: History and Theory, saying that the cell was "no practical importance", however he showed his interest in the theoretical side "It was a puzzle, how gases separated by a thick layer of liquid were able to combine with the help of the catalytic power of platinum."[26]

The first alkaline, practical fuel cell was developed by Francis Thomas Bacon in the 1940s-1950s; this cell comprised of a potassium hydroxide electrolyte and nickel electrodes. It was found that the performance of this electrolyte as comparable to the sulphuric acid used by grove, however Bacon's chosen electrolyte was not as corrosive to the electrodes. The reliability of his fuel cells received the attention of the American aerospace company, Pratt and Whitney, who authorised Bacon's work to be used in the fuel cells on the Apollo spacecraft (1968) to provide electricity and drinking water for the crew. The technology of PEM originated from the company General Electric, through the work of Niedrach and Grubb in the 1960s. This technology was used in NASA's project Gemini (1966). The electrolyte was initially sulfonated polystyrene membranes; however these were later replaced by Nafion. The PEMFCs were replaced by alkaline fuel cells for use in the Space shuttle program at NASA.

The PEMFC operates at relatively low temperature (around 80 °C), meaning there is less thermal damage to components, it has quick start-up (in minutes) and is suited for use in back-up power, mobile phones and vehicles. However, its limitations include the ease of poisoning of the precious catalyst; (this will be discussed in more detail in later sections) and the difficulties arising from hydrogen storage.

Since then, significant improvements have been made in increasing the power density and significantly decreasing catalyst loading, and therefore cost. Electrons produced from the oxidation of hydrogen at the anode carry electricity through the external circuit. Protons move in the same direction but across the proton exchange membrane where they combine with the electrons and oxygen at the cathode to take part in the reduction of oxygen to water. Other fuels can be oxidised at the anode instead of hydrogen, for example, alcohols.

In this instance, carbon dioxide is also produced as a product (see Section on DAFCs). The hydrogen oxidation reaction (HOR) will be discussed in Chapter 2 Section.3.

There are many different types of fuel cells; these are generally classified by the electrolyte used. This dictates the type of chemical reaction, catalyst used, operating temperature, fuel and ultimately the applications of the fuel cell. Different types of fuel cell therefore exist to suit different applications, as will be briefly discussed below.

The fuel cells to be described in this work are the formic acid fuel cell (FAFC) and the direct glycerol fuel cell (DGFC). Other types of fuel cell exist such as the solid-oxide fuel cell (SOFC), phosphoric acid fuel cell (PAFC), molten carbonate fuel cell (MCFC) and alkaline fuel cell (AFC). Some of these operate at relatively high temperatures, particularly the SOFC and MCFC and are more suited to larger applications such as use in power generators. In this work, we wished to focus on fuel cells which can operate under more ambient conditions and that are suited to applications in portable electronics and transport. Advantages, disadvantages and applications of the FAFC and DGFC will be summarized in the following sections.

### 1.3.2 Direct Alcohol Fuel Cells

Two of the main drawbacks in the utilisation of fuel cells driven by hydrogen are the lack of hydrogen infrastructure and the implementation of high pressure tanks in automotive applications.[27] Therefore, many efforts have been put into the development of fuel cells that use liquid alcohols as fuels.[11] Among all the alcohols, methanol, ethanol, 2-propanol and ethylene glycol are the most promising fuels due to their low molecular weights meaning they are easy to store, transport and handle.[28] Additionally, they have relatively high mass energy densities comparable to those of gasoline and hydrocarbons.[28]

#### 1.3.2.1 Direct formic acid fuel cell

Reforming is not necessary for use of formic acid as a fuel and there is no need for high pressures or low temperatures as it is a liquid at room temperature. Formic acid has the

added advantage over methanol that it does not cross the membrane and therefore the DFAFC has a higher efficiency than the DMFC. Drawbacks of using formic acid are that it is only suited to small applications and it has a lower energy density of 2.1 kW/l, which is less than half that of methanol. We chose to study this system in order to improve its limitations of catalyst poisoning and low current density through synthesis and application of alloy catalysts prepared by the cathodic corrosion method. The oxidation of formic acid has attracted attention in the literature both as a fuel and due to its role as an intermediate in the methanol oxidation. Electrochemical analysis of this intermediate can help deepen understanding of the methanol electro-oxidation and aid in catalyst design for this reaction.

In the following, a brief introduction on the oxidation of formic acid will be given, to include the value and production of the chemical, its uses, an overview of the various reaction pathways involved in the mechanism and the associated energy barriers of these pathways. The reader should refer to Chapter Three for a more extension discussion of the reaction mechanism, including the active intermediate, previous catalysts used for this reaction, related theory and a more in depth look at relevant literature.

Formic acid is a colourless, clear liquid at room temperature; it has a distinct smell and is corrosive at high concentrations. Besides its uses as a fuel in fuel cells, it has many other applications. Its main uses are as a silage additive, preservative in animal feed, food and drinks, involvement in textile dyeing and leather tanning. Other uses include as a miticide,[29] de-icing agent, its use in electroplating and the rubber industry.[30,31]

Formic acid is known to exist in nature, such as in stinging nettle, ants and as a product from oxidation of terpenoids emitted from plants in tropical and boreal forests.[32] In addition to its natural origins, it can also be produced synthetically via several different methods, some of which will be discussed briefly below. The main industrial producers of formic acid include companies such as BASF, LC Industrial, Eastman Chemical Company and Feicheng Acid Chemicals.[33] Possible routes to synthesis are through the hydrogenation of carbon dioxide, heating of oxalic acid in glycerol, oxidation of biomass, a two-step synthesis via reaction of carbon monoxide with methanol or through oxidation of biomass.[31,34,35,36,37]

In 2009, the global production of formic acid was 720,000 tonnes, with around 370,000 coming from China alone. The price of formic acid, like many other chemicals, is dependent upon purity. In Europe, 2009 prices for commercially available 85-99 w/w % formic acid were around € 650/tonne, whereas in the US it was priced at $ 1250/tonne.[33]

Moving onto the oxidation of formic acid, many studies have been conducted on this molecule because it is small and has bonds that are common in organic molecules (C-H, C=O, C-O and O-H), making it an ideal model for study. Its oxidation has been studied on many metals, with platinum found to be the most effective catalyst. There are three proposed pathways for the oxidation of this molecule; the direct, formate (also known as the direct) or indirect pathway.

Direct: $HCOOH \rightarrow COOH + H^+ + e \rightarrow CO_2 + 2H^+ + 2e$ (1)

Formate/direct: $HCOOH \rightarrow HCOO + H^+ + e \rightarrow CO_2 + 2H^+ + 2e$ (2)

Indirect: $HCOOH \rightarrow CO + H_2O \rightarrow CO_2 + 2H^+ + 2e$ (3)[38]

Figure 2 illustrates the calculated barriers for each step of the pathways mentioned above.

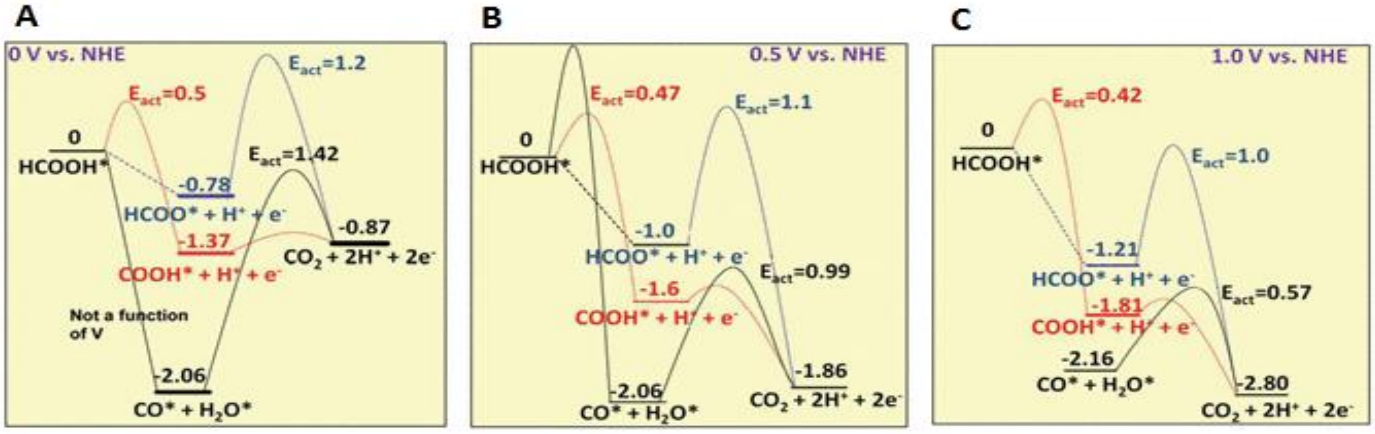


**Figure 2.** Computationally calculated energies for the three pathways of the oxidation of formic acid on Pt(111) held at constant potential. A) 0 V vs NHE B) 0.5 V vs NHE and C) 1.0 V vs NHE.[38]

At 0 V, the first steps of the formate and indirect pathway have low activation barriers and are therefore favourable, however their second steps have large activation energies; this results in stability of the poison intermediate on the surface of platinum. The activation

barrier of the second step at 1.0 V is significantly lower than the barriers for this same step at lower potentials, because at 1.0 V, the poison intermediate has been oxidised and therefore removed from the surface of the metal. Another small organic molecule is glycerol, which has also been investigated as a fuel.

### 1.3.2.2 Direct glycerol fuel cell

Advantages of the direct glycerol fuel cell include the fact that glycerol is a readily available, non-toxic, 'clean' fuel source with a theoretical energy density (5.0 kWh $kg^{-1}$) comparable to that of methanol (6.1 kWh $kg^{-1}$). However, this system is not without its drawbacks which include problems controlling selectivity of products formed during the oxidation and poisoning of catalysts by species formed during the reaction. Despite generating power comparable to that of a DMFC, it must be noted that this is still far less than can be produced from a hydrogen fuel cell (33 kWh $kg^{-1}$), meaning a much higher mass of glycerol is needed to achieve a certain amount of power. This suggests DGFCs are good for applications in small portable devices such as GPS units, iPods, phones or stationary applications.[39] Despite this, it was reported in the literature of a DGFC which had five times the energy density of a comparable DMFC, however this was using an alkaline anion-exchange membrane which will not be covered in this work.[40] We decided to study this system in order to try and overcome the disadvantage of catalyst poisoning and low current densities by applying our own alloy nanoparticle catalysts to this reaction.

Glycerol is produced in large amounts as a by-product during synthesis of biodiesel, for every tonne of biodiesel, 0.1 tonnes of crude glycerol by-products are also produced.[41] The surplus glycerol presents a large disposal problem; therefore it is necessary to determine uses for this compound not only in terms of waste but to also improve the economics of biodiesel production. One current challenge in the glycerol oxidation is that catalysts must be able to tolerate the impurities present in crude glycerol.

Glycerol is a simple polyol with three hydroxyl groups. The uses of glycerol are many, with over a thousand uses of the compound as an end product. Many of these uses can be found in the literature.[42,43] The main uses can be broken down into several categories; these include an additive in the food industry (E422), cosmetics industry, pharmaceuticals,

synthesis of other compounds such as polyols and preparation of materials such as tobacco and explosives.[42,43,44,45] In discussing a molecule as a potential fuel, it is also necessary to evaluation its abundance, methods of production, cost and products upon oxidation.

Production of glycerol

Natural glycerol can be either animal or plant derived. Glycerol can be obtained from animal fat or vegetable oil such as that from palm, soya or coconut. Animal derived glycerol is generally avoided by vegetarians whereas vegetable derived glycerol is also not without its drawbacks. Palm oil is known to be one of the biggest causes of deforestation in countries such as Indonesia; therefore glycerol production from palm oil contributes to this.[46] However, glycerol may also be produced synthetically from petrochemicals through a variety of routes.

Glycerol as a fuel

Glycerol is desirable as a potential fuel since it has a high energy density, it is non-volatile and non-toxic. It is also widely available since it is formed as a by-product from biodiesel production.[47,48] Approximately 950,000 tonnes of glycerol is produced in Europe and the U.S. each year.[49] A legal act of the European Union, known as the Biodiesel Directive, required member states to replace 5.75 % of petrol and diesel with biofuels such as glycerol for transport, by 2010. Past attempts in electrochemical oxidation of glycerol have resulted in poor results due to difficulty in combining glycerol with the Pt catalysts.[47] Oxidation of glycerol produces compounds of high value, which is beneficial economically. This will be discussed in detail below.

Figure 3 shows a simplified schematic of the oxidation of glycerol. It illustrates that the reaction is a complicated process which takes place in many steps and through many different compounds, which will be shown and explained in greater detail in Chapter 4 (Section 4.1). Due to the structure of glycerol being highly functionalised, bearing two secondary OH groups and one primary OH group, a large variety of compounds can be formed. What is formed depends on the number of oxidised sites, the type of oxidised sites, the degree of oxidation and any side reactions that may occur (such as hydration, isomerisation, polymerisation, decarboxylation and decarbonylation).[45] The reaction may

take one of two routes; the first goes via dihydroxyacetone (DHA), a valuable product, whilst the second goes via glyceraldehyde. Upon complete oxidation, glyceraldehyde is converted to glyoxalic acid and then ultimately both pathways join to form oxalic acid and carbon dioxide as the final oxidation products. Many factors affect the selectivity towards a particular product; these include particle size of the catalyst, along with pore size of the catalyst support and pH of the reaction media.[45] The selectivity towards a desired product has important economical implications.

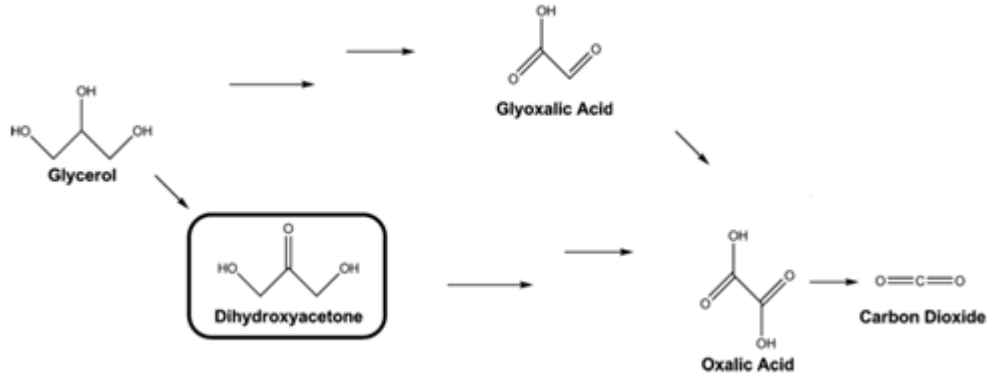


**Figure 3.** A simplified schematic showing the oxidation of glycerol as a multi-step process with some of the oxidation products illustrated, schematic adapted from Hu et al.[50]

The catalytic oxidation of glycerol has not yet reached industrial scale. The main important oxidation products include DHA, MA and TA. Katryniok et al[45]. provided an approximate estimation of production costs (taking into account expense of reagents, including catalyst). They concluded that around 55-86 % of the total costs are estimated to be from the catalyst. It was estimated that the value (sales price) of DHA is approximately 150 US $ per kg, whereas the values of purified and crude glycerol are around 0.6 and 0.3 US $ per kg, respectively. This means that production of DHA via glycerol oxidation is commercially feasible. Competitive pricing can be increased as technology advances and more research is conducted to produce more active catalysts with higher stabilities.

Dihydroxyacetone has been chosen as the product to be discussed, since this one is the most economically viable due to its significant market in the cosmetics industry. Routes to

synthesis involving heterogeneous catalysis along with uses and economic viability of the product will be included.

Dihydroxyacetone, commonly abbreviated to DHA, is an important product of the glycerol oxidation due to its use in sunless tanning agents. Tanning of skin by DHA occurs via the Maillard reaction with amino groups on skin.[51] Alternatively, commercially available DHA is produced by a fermentation process by companies such as Merck. Synthesis of DHA by heterogeneous catalysis will be discussed and summarised in the following.

In 1995, Garcia et al.[52] confirmed the findings of Kimura's et al.[53] that Pt on C displays weak activity towards the oxidation of glycerol to DHA in acidic conditions. Since the yield of DHA was very poor (4 %), the next step was to focus research on optimisation of the Pt on C by use of promoters.[53] The highest yield of 20 % was obtained when using Bi as promoter. While Kimura et al.[54] observed effects of promoters, Garcia et al.[52] focused on optimising the reaction conditions, achieving a slightly higher yield than Kimura et al. of 28 %. Groups such as Bradner,[55] Xie[56] and Hu et al.[50] also looked at optimisation of this reaction through Pt and Bi ratio. To summarise these findings, it was found that the selectivity to DHA is unaffected by the amount of Pt and addition of Bi increases catalytic activity when the amount of Pt is kept constant (at 5 wt %). Gold catalysts were also investigated for this reaction;[57] however they will not be discussed as part of this work.

Since platinum alone has limited ability towards alcohol oxidation due to its difficulty in breaking the C-C bond, we chose to synthesise a ternary alloy to use in the oxidation of glycerol. Palladium is much cheaper and more abundant than platinum and is used for C-C bond cleavage, often as an oxidation catalyst[58] where it has shown good activity in DFAFC.[59] Rhodium is also often used as an oxidation catalyst and has a higher tolerance towards poisons, aiding the oxidation of CO to $CO_2$. Platinum-rhodium catalysts make effective oxidation catalysts if a third element is added to speed up the kinetics.[60] For this reason, we chose to prepare the ternary alloy PtRhPd for use in the glycerol oxidation.

# Chapter 2

# Nanoparticles as Electrocatalysts

## 2.1 Introduction

Nanoparticles are particles with one dimension of 100 nm or less in size, they usually lie within the range of 1-20 nm.[61] They encourage wide scientific interest for many reasons, some of which will be mentioned in the following. These materials bridge the gap between atomic and bulk structures. As the size of a material approaches the nano range, its properties change and a much larger proportion of its atoms are present at the surface compared to a bulk material. The high surface area to weight ratio of nanoparticles means they are often more reactive than their bulk counterparts and have unique properties. Such unique and interesting properties of nanoparticles make them suited to many applications, for example since nanoparticles are small enough to confine their electrons, they can produce quantum effects. These effects, through a change in energy levels (described by the Fröhlich-Kubo approach),[62] result in modified thermodynamic and electronic properties.[63]

Nanoparticles can be thought of as consisting of three layers; the core (the centre of the nanoparticle responsible for most of the properties), the shell (the second layer which has a different structure from the core) and a surface which can be functionalised with surfactants, polymers and small molecules or ions.[61] Their high surface area and metal dispersion makes them well suited to applications in fuel cell catalysis. Fuel cell reactions have been shown to be sensitive to both structure[18,19,64] and particle size[65,66,67] of nanoparticles. This chapter includes a section on nanoalloys followed by a brief discussion of the fundamental reactions of electrochemistry, synthesis techniques and introduction to the characterization methods used in this study and concludes with a summary and outlook.

## 2.2 Alloys and Nanoalloys

Nanoparticles can be formed from many metals, including s, p and d block metals. When nanoparticles involve two or more metals (known as bimetallic or multimetallic, respectively), they are called nanoalloys. This means that many metallic element combinations and compositions are possible. The structure and properties of nanoalloys often differs from their pure elemental counterparts of the same size.

Bimetallic nanomaterials can take up a number of different structures depending on how the two metals mix; two of these are alloy and intermetallic structures.[68] These two groups both have a homogeneous mixture of the two metals in which metal-metal bonds form. The difference between alloys and intermetallics is that alloys have random atomic orders whereas intermetallics exhibit long range atomic orders.[69] Evidence of alloying can be seen from XRD in which new Bragg reflections from alloy M-M bonds appear and peaks of individual metals are absent.

In this thesis, non-conventional alloys of platinum are prepared. Previously, high temperature methods such as induction melting,[70] vacuum arc melting[71] and electron beam melting[72] were used to create such alloys. Such methods are time consuming and energy inefficient. It is very difficult to prepare these alloys at ambient temperatures, as can be seen from the phase diagrams (see Chapter 5 for PtTa and Chapter 3 for PtBi). On the other hand, our method is much more efficient since it is performed at room temperature and takes as little as a few minutes to obtain enough sample for use in catalysis. Other previous synthesis methods will be discussed in Section 2.4.1.

As mentioned in Chapter One, reduction of the platinum content of a catalyst can be achieved by alloying with other metals such as Bi,[73,74] Pb[75,76] and Pd[77] and by preparing the catalyst in high surface area nanoparticle form. Use of co-catalysts not only has the advantage of decreasing cost, but also increases activity through electronic effects, (also known as the bifunctional mechanism)[73] and the third body effect.[73] Preparation and application of alloy nanocatalysts has enjoyed much attention in the literature[61,77,78,79] and in this work, a versatile method for preparation of not just alloy nanoparticles, but also single metal nanoparticles and oxides will be presented.

As stated previously, though nanoparticles are reactive due to low coordinated surface atoms, an advantage of nanoalloys over monometallic nanoparticles is the ability to tune adsorption strength and catalytic activity. Catalytic activity may increase upon addition of an alloying metal due to synergistic effects.[68,80,73] In addition to synergistic effects, there are many other factors that come into play in affecting the activity of nanoalloys. These include magic sizes,[81,61] along with segregation and surface structure.[82,83]

Adsorption and reaction on nanoalloys

The surface is the site of reaction and surface reaction occurs in the chemisorbed state; this adsorption can be either dissociative or non-dissociative. In dissociative adsorption, the small adsorbing molecule breaks up into separate atoms which bind to the alloy surface. An example of this is the non-dissociative adsorption of formic acid on platinum.[84] On the contrary, in non-dissociative adsorption, the small adsorbent remains intact. Whether dissociative or non-dissociative adsorption takes place can depend on the size of the cluster.[62]

Adsorption of CO

As explained previously, CO is a well-known catalyst poison. Though it is isoelectronic with diatomic nitrogen, it adsorbs much more strongly; this is because $N_2$ usually binds via a single metal atom whereas CO can bind up to four metal atoms (due to its $\pi^*$ antibonding orbitals). Binding of CO has been reported to give higher stability to metal clusters by preventing aggregation.[62] Theoretical calculations by Jellinek et al.[85] showed that restructuring of a metal is possible upon binding of CO. It is proposed that if the binding energy is greater than the rearrangement energy of the cluster, then the cluster may be prone to rearrangement upon binding of CO.[62] For a more comprehensive review of the use and analysis of nanoalloys in fuel cells, above that which is provided throughout this work, in-depth reviews can be consulted.[86,87]

## 2.3 Fundamental reactions

The most studied reactions in electrocatalysis are the fuel cell reactions described below, therefore a brief introduction to these processes will be given.

## Hydrogen oxidation reaction *(HOR)*

The HOR could be described as the most important reaction in electrocatalysis. Pt catalysts are used in this reaction, often alloyed with other metals such as Sn, Os, Mo and Ru in order to increase the catalyst's tolerance to CO. Despite the simplicity of this reaction, the mechanism and kinetics are still not fully understood; there has been disagreement in the literature about the mechanism (whether it follows a Tafel-Volmer or Heyrovsky-Volmer route) and the intermediate present.[88,89] The generally accepted three-step mechanism is the Tafel-Volmer-Heyrovsky mechanism[90] as shown in Schemes 1 to 3 below, where M is a Pt atom and e is an electron:

- The Tafel step, involving chemisorption of hydrogen atoms:

  $2M + H_2 \leftrightarrow 2H_{ad}$ (4) (rds)
- The Heyrovsky step, involving hydrogen adsorption:

  $M + H_2 \leftrightarrow H^+ + H_{ad} + e$ (5)
- The Volmer step, in which the H adatom desorbs and is oxidised:

  $H_{ad} \leftrightarrow H^+ + e$ (6)[91]

Skúlason et al.[92] concluded that the Volmer-Tafel reaction is dominant on any type of electrode (at 0 V applied potential) due to faster kinetics (by several orders of magnitude) compared to the Volmer-Heyrovsky pathway. However it was observed by Markovic et al.[93] that different faces of Pt facilitated different reaction pathways; for example for the Pt(110) surface, the Tafel-Volmer mechanism was observed whereas for the (111) surface of Pt, the Volmer-Heyrovsky mechanism was more feasible.

## 2.4 Synthesis

When preparing nanoparticles, a compromise between size and stability is desired. Small nanoparticles, although highly active due to a large surface area, have a high surface energy and can therefore be unstable. In contrast, larger nanoparticles are less active and have a lower surface energy (and hence higher stability) due to a larger proportion of atoms on the surface. Understanding the links between size, shape and reactivity are key to establishing structure-property relationships.

### 2.4.1 Previous synthesis methods

Old fashioned routes to synthesise nanocatalysts in high yield include colloidal,[94] wet-impregnation,[95] gas phase synthesis[63] and micro-emulsion.[80] The first two of which carry the disadvantages of using organic solvents, capping materials and/or surfactants in order to control particle size, shape and composition of the catalyst.[96] High temperature and chemical cleaning procedures are able to overcome the organic contamination; however this is at a price which causes both surface orientation and size distribution of the nanoparticle to be affected. Whereas gas phase synthesis suffers from low yields and the wet-impregnation method produces large, non-uniform nanoparticles.[6] For these reasons, we used a novel method, cathodic corrosion, to prepare our catalysts.

### 2.4.2 Cathodic corrosion

Cathodic corrosion is a relatively new method for preparation of catalytically active nanoparticles with unparalleled control over parameters such as particle size distribution, shape, chemical composition and surface structure.[6,7,16,97] Variation of the cation in solution allows the shape and size of the nanoparticles to be modified, the cation choice can also slightly affect the charge on the Pt anion (i.e. $Pt^-$ or $Pt^{1.3}$)[98,99]

This method has been shown to be advantageous for production of alloy-nanoparticles where previously segregation of metals was an issue.[7] In comparison with previous methods, time, process cost and loss of precious metal associated with the multi-step

processes are reduced. The absence of organics in our method also means that the resulting nanoparticles are clean and therefore directly usable as catalysts.

Figure 4 below shows the experimental setup for cathodic corrosion.

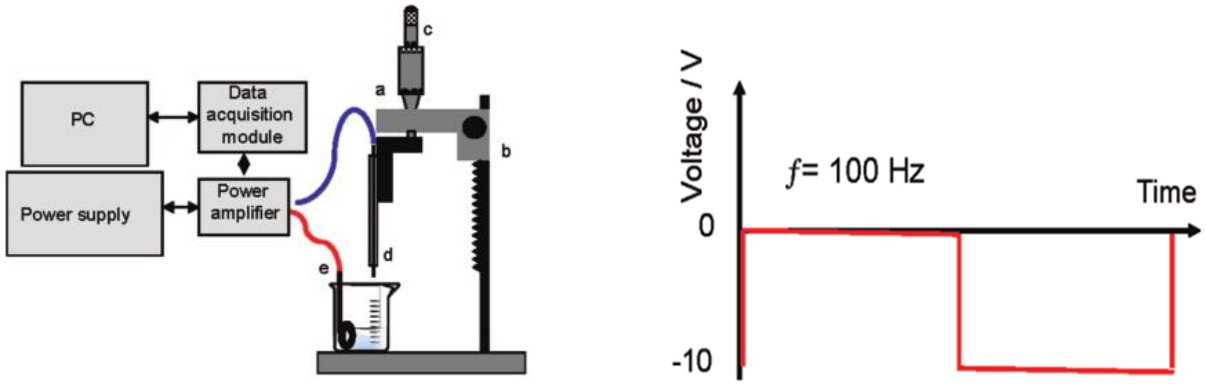


**Figure 4.** (**left**) Diagram to show the experimental setup of a cathodic corrosion experiment where (a) corresponds to the support which is also attached to the coarse screw. (b) A fine micrometric screw (c) is used to lower the working electrode (d) into the solution. The solution is also in contact with a high surface area electrode (e). (**right**) the AC wave function used to prepare the nanoparticles. Figure adapted from Rodriguez et al.[7]

On application of a negative AC potential, a metal electrode is converted into nanoparticles. The setup consists of a power supplier and power amplifier which allow the control of potential and frequency. Typical conditions used in this work were a frequency of 100 Hz, duty cycle 50 %, amplitude of 5 V and an offset of -5 V in order to keep the potential negative, see Figure 3, right. The offset refers to offsetting the waveform from 0,0. If the AC is offset, it means that the metal is cathodic during the full AC cycle.[6]

Figure 5 below shows a plot of the current versus time plot during nanoparticle synthesis using the cathodic corrosion software.

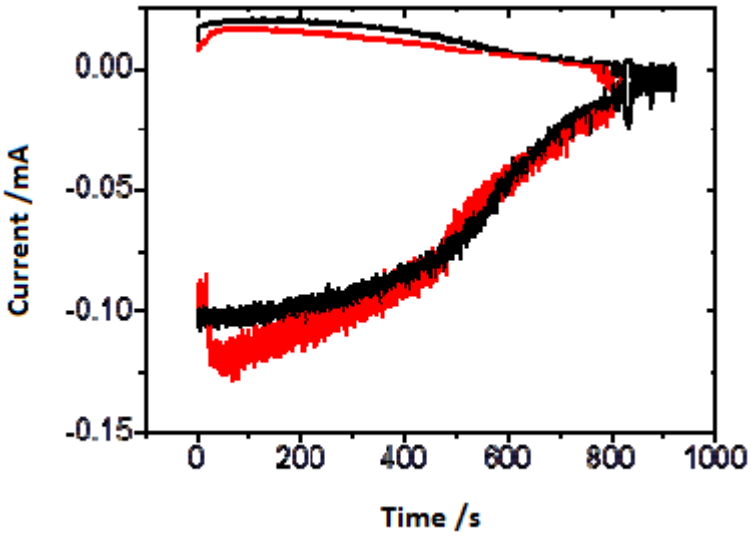


**Figure 5**. Example Origin plot of AC current (5 V square wave AC voltage with offset-5 V, 100 Hz) versus time obtained for a sample of PtBi (red) and PtPb (black) nanoparticles preparation under steady conditions.[100]

The proposed mechanism[16] for synthesis of nanoparticles via decomposition of a metal wire under negative potential is as follows:

1. Protons and/or water molecules at the electrode undergo reduction.
2. The 'Zintl phase' precursor to nanoparticle formation is formed.
3. This short-lived Pt intermediate is oxidised back to its metallic state
4. Nanoparticles are formed.

The negative potential causes protons and/or water molecules at the electrode to undergo reduction; this creates an aprotic layer of high pH at the electrode-solution interface containing very little free water. The electrolyte cation stabilises the Pt metal anions. The metal-alkali compound is known as a 'Zintl phase' and is a precursor to nanoparticle formation. The short-lived, moisture sensitive, ionic Pt intermediate is oxidised back to its metallic state by free water molecules and other oxidative species. Nanoparticles are formed by an agglomeration of these metal atoms.

During the formation of binary nanoparticles, the method and mechanism is slightly modified, as depicted in Figure 5 below. The main metal, Pt, for instance, is used as the working electrode whereas the alloy metal is added to the solution in the synthesis vessel. The schematic below shows production of a metal-alloy complex, preceded by formation of a surface alloy from two metals. The diagram shows the positive alloy metal attaching to the surface of the negative Pt metal electrode, this surface alloy then undergoes etching as part of the corrosion process and agglomeration occurs, resulting in formation of alloy nanoparticles leaving the electrode.

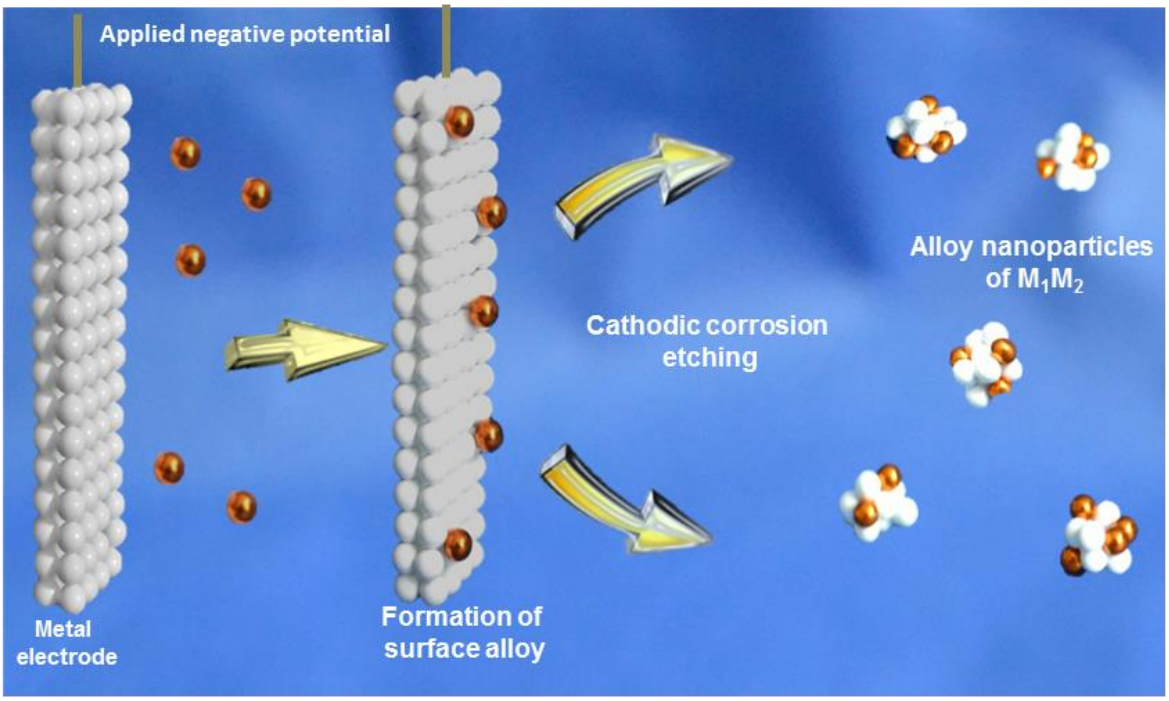


**Figure 6.** Schematic representation showing the formation of alloy nanoparticles, taken from Bennett et al.[100]

Zintl phases are a class of intermetallic in which alkali metal cations are taken up into the matrix of a metal.[101] They are formed upon reaction of a group 1 or 2 metal with a post-transition metal element (i.e. one from group 13-16). Group four and five elements such as Pb and Bi, respectively, can be reduced electrochemically to form intermetallic phases.[98] Typical properties of these types of intermetallic include high melting point, poor conductivity and brittle in nature. They are ionic and involve electron transfer from the

more electropositive metal to the less electropositive metal. The Zintl-Klemm concept states that the polyanionic structure of the Zintl phase should be similar to an isoelectric element.

Although platinum most commonly exists in the +2 and +4 oxidation states and less commonly in the +1 and +3 where it is stabilised by metallic bonding, platinum is able to form negative oxidation states under certain circumstances. Observation and evidence of these have been reported in the literature.[98,99,102] In agreement with our mechanism, Ghilane et al.[98] also proposed formation of a negative platinum species from a metal electrode subjected to a negative potential. The existence of this negative platinum phase was observed via X-ray photoelectron spectroscopy (XPS) (see Section 2.6.1); due to the relationship between binding energy and atomic partial charge of a material, the oxidation state of the atoms can be elucidated. The Pt($4f_{7/2}$) level was observed by this group to shift to lower binding energy (from 71 to 69 eV) upon application of a negative potential. This is indicative of an increased electron density on the Pt, compared to elemental Pt and is therefore evidence of the formation of the negative Pt species.

The positions of Pt and Au in the periodic table could be the cause of these observations, their position means that relativistic effects come into play; as atomic number increases, the 1s electrons gain velocity resulting in them gaining mass and making the orbital contract towards the nucleus. This has a knock-on effect, resulting in higher energy s and p orbitals also contracting with the end effect being that the 6s orbital becomes smaller than it would have been without the contraction. While Pt and Au have the configuration 6s1 with an additional 5d electron compared to most other metals in the 5d period, this means that the additional 5d electron results in an increased contraction of the 6s orbital. The low energy and resulting stabilisation of the 6s orbital in Au and Pt means that these metals are capable of gaining an electron. Upon doing this, they are said to be behaving as 'pseudohalogens'. Stabilisation of the 6s orbital results in properties such as resistance to corrosion and high ionisation energy. On examination of the Pauling scale of electronegativity, Pt and Au have the highest Pauling numbers out of all the metals, so this is hardly surprising.[101]

Simonet[103] provided evidence for a reversible charge on Pt metal under super-dry conditions. Pt existed in an iono-metallic structure as the species $Pt_2^- M^+$, MX in a solution of DMF and *t*-n-butylammonium iodide as observed by coulometric studies, dynamic EQCM

analysis and voltammetry.[103] Simonet also discussed the corrosion of platinum in the cathodic potential range. Though platinum is known for its stability, even at oxidising potentials, due to the weak hydrogen overvoltage, the same does not stand for high cathodic potentials. He formed clusters of platinum of the following proposed general formula: $[Pt_2^-, (1 + n)\ NR_4\ , nX^-]$ where R is an alkyl and X is a halogen.[104] Platinum commonly exists in unusual, negative oxidation states in compounds called platinides, where it is combined with another metal, similar to an ionic substance. These substances share some of the chemical and physical properties of platinum, such as resistance to corrosion, high melting point and reasonable electrical conductivity.

Platinides

In addition to interpreting structures, quantum chemical calculations can predict whether certain compounds could exist, therefore inspiring experimentalists to synthesise them. Band structure and molecular orbital (MO) calculations can be carried out to predict electronic structure and estimate the oxidation state of particular atoms. Various platinides reported in the literature will be discussed below. The preparation and isolation of such species need extreme experimental conditions due to the strong reducing environment in which the salts were obtained. The platinides to be discussed will include the caesium-platinum system, barium-platinum system and more complex platinides involving several other elements.

$Cs_2Pt$

A caesium platinide showing complete charge separation was reported by the Jansen team.[105] This structure was formed using high temperatures (700 °C) and was found to be air and moisture sensitive, yet resistant to thermal decomposition up to 200 °C. The crystals formed took a hexagonal arrangement in which a Pt atom was surrounded by nine Cs atoms (see Figure 7) and were dark red in colour and transparent. The transparency and red colour are indicative of charge separation (and ionic structure) due to presence of a band gap. This evidence of 6s stabilisation and negative metal oxidation states is further supported by

quantum chemical calculations on band structure.[102]

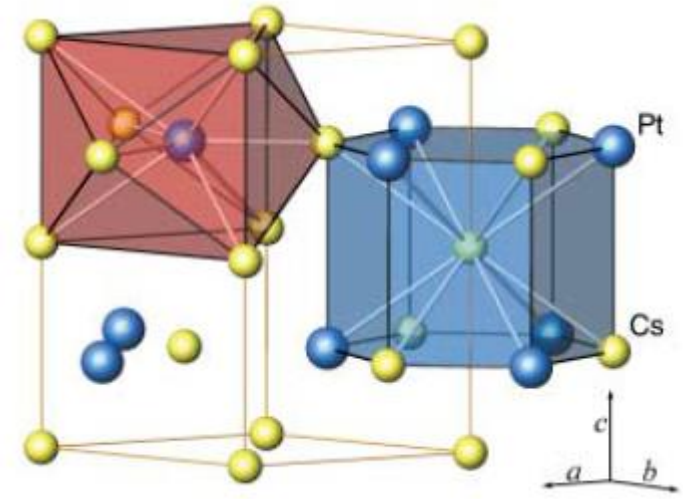


**Figure 7.** Representation of the crystal structure of $Cs_2Pt$ (red: $PtCs_9$ polyhedron, blue: $(Cs1)Pt_6(Cs2)_6$ polyhedron), taken from Jansen et al.[102]

Ba-Pt systems

These results mentioned were in agreement with the electron spectroscopy for chemical analysis (ESCA)[106,107] spectra recorded for platinum-barium compounds conducted by the Karpov team.[99] They also observed a shift in binding energy to lower values.

Figure 8 shows the crystal structure of BaPt, it is taken from an article published by Jansen [99] which provides evidence for the formation of both platinum and gold anions. Negative states of platinum in barium platinides was confirmed by XPS. This molecule is an example of a Zintl phase. The main points put forward in this article include the following:
The electron configurations of Pt and Au are Pt [Xe] 4f14 5d9 6s1 and [Xe] 4f14 5d10 6s1, respectively.[108]

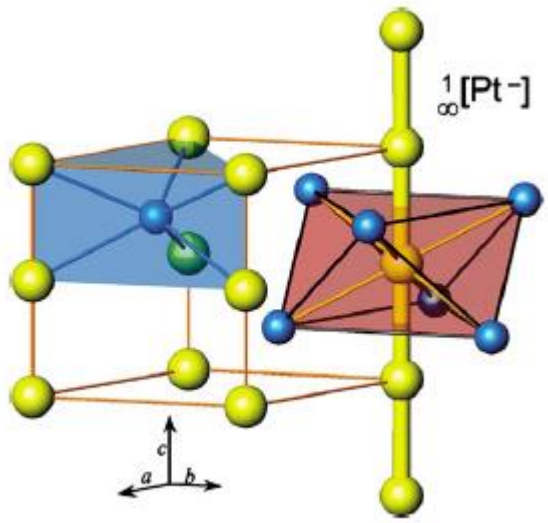


**Figure 8.** Crystal structure of barium platinide with coordination polyhedral shown where blue spheres are Ba atoms, yellow spheres are Pt atoms and orange lines are the edges of the unit cell. Taken from Jansen et al.[102]

More complex platinides

Clusters containing fluoride are difficult to obtain, for a long time, $Nb_6F_{15}$ had been the only cluster containing fluoride to be discovered. However, in the last decade, Pt containing species such as $PtIn_7F_{13}$ [109, 110] and $Pt_3In_{22}F_{40}$ [111] have been discovered. An example of a more complex platinide is the $Pt_2In_{14}Ga_3O_8F_{15}$ species prepared by Kohler et al.[112] The oxyfluoride prepared by this team was found to contain a positive cation $[PtIn_6]^{10+}$ in which the Pt was in a negative oxidation state. This material was prepared using high temperatures of 600 °C over a long time span (480 h), with the resulting product observed to be air stable. The structure was analysed by X-ray crystallography, electronic structure was obtained from quantum chemical calculations (LMTO). The oxidation state of Pt was estimated to be -2 from the MO diagram.

To conclude, the mechanism of cathodic corrosion has been discussed, which proceeds through a negative Pt species, evidence of which has been given in the discussion of platinides. Following synthesis, nanoparticles must be cleaned before use, since they contain excess reactants such as the electrolyte and solution of the alloying metal. The simple cleaning method used in this work will be discussed in the next section.

## 2.5 Cleaning of nanoparticles

The cleanliness of nanoparticles is commonly evaluated by use of X-ray diffraction and running blank cyclic voltammograms. Cleaning steps are essential when surfactants are used, particularly proceeding synthesis of colloidal nanoparticles.[94] Vidal-Iglesias et al.[113] reported a UV/ozone treatment as a methodology of cleaning nanoparticles. This method was initially reported by the Somorjai team[114] as increasing the activity of colloidal catalysts in the gas phase. However, it was found that although this method did not alter the shape and size of the nanoparticles, surface rearrangement of atoms took place resulting in altered catalytic properties.[113] In contrast, the absence of organics in our method means that the resulting nanoparticles are clean and therefore are directly usable as catalysts.

The Koper group[94] observed that polyvinylpyrrolidone (PVP) could be removed from Pt nanoparticles with a mixture of dilute sulfuric acid and hydrogen peroxide. This cleaning method, in contrast to the UV/ozone treatment, does not change the surface structure of the nanoparticles. It's thought that the molecules of PVP are removed by bubbles on the surface of the nanoparticles generated from decomposition of the $H_2O_2$.

The method used in this work involved adding the nanoparticle suspension to Milli-Q water, centrifuging this mixture and then decanting in order to remove unwanted ions from the electrolyte. This process was repeated until the pH became reached neutral. This will also be mentioned in the experimental sections of the following chapters.

## 2.6 Characterisation of nanoparticles

Following synthesis and necessary cleaning, the nanoparticles were characterised via various physical and electrochemical methods. There are many ways of determining the physical and chemical information about catalysts, some of which will be discussed below.

## 2.6.1 Physical Characterisation

The physical methods of characterisation for nanoparticle electrocatalysts that will be discussed in this section include X-ray diffraction (XRD), X-ray fluorescence (XRF), X-ray photoelectron spectroscopy (XPS) and the microscopy related techniques, transmission (TEM) and scanning electron microscopy (SEM) and energy dispersive x-ray analysis (EDX).

## X-ray diffraction *(XRD)*

XRD is one of the oldest yet most common and useful techniques employed to provide an approximation of particle size and determine crystalline phases. Diffraction of X-rays by crystals was discovered by Max von Laue, for which he was awarded the Nobel Prize in 1914. W. H. and W. L Bragg then devised an explanation for the technique, now known as the Bragg Law.[115]

X-rays are energetic enough to penetrate solids, which makes them suited to investigating internal structure. XRD operates by firing a beam at the sample, some X-rays are absorbed and some are diffracted. X-rays are diffracted from the crystal at an angle of 2θ and the distribution of scattered rays is affected by electrons in the sample. The diffraction pattern (diffractogram) observed is produced by elastic scattering of X-rays (scattered rays have the same wavelength as those in the beam) by atoms in a lattice. Constructive interference arises from monochromatic scattered X-rays which are in phase. A typical diffraction pattern of a sample with a crystalline structure will display many sharp peaks; these correspond to different crystal planes, based on the Bragg Law (equation 7). There are several equations describing the relationship between sample structure and the diffraction pattern observed. The Bragg Law is one of these; a peak is observed when the Bragg condition is met:

$$n\lambda = 2dsin\theta \qquad (7)^{68}$$

where:

λ= wavelength

n= the order of reflection, an integer

d= the d-spacing, distance between adjacent crystal planes

θ= the Bragg angle, at which a peak is observed

The Bragg relation describes how lattice spacing can be derived from diffraction of X-rays by crystal planes. Lattice spacings are characteristic of a certain material. XRD is used to identify different crystalline phases within a material, to give an indication of purity, as a fingerprint and to give an estimate of particle size which can be confirmed by TEM. Another equation relevant to this study is the Scherrer equation (equation 8) which relates line width to crystal size and was used as the basis to estimate particle size in this project.

$$D_{hkl} = K\lambda/(B_{hkl}\cos\theta) \qquad (8)$$

where:

$D_{hkl}$ = crystallite size

K = crystallite shape factor

λ = wavelength of X-rays

$B_{hkl}$ = peak width at half maximum

θ = Bragg angle

The Scherrer equation can be used to determine particle size and can be applied to particles up to 100-200 nm in size.[117] Since the width of the peak provides information on the dimensions of crystal planes, it can only provide clear, defined peaks for a sample with sufficient long range order. This is the limitation of XRD. For example, for crystals less than 100 nm in size, such as those analysed in this work, broad peaks are observed caused by incomplete destructive interference.[118]

A derivative of the Scherrer equation, the Debeye-Scherrer equation, was used by the XRD software to find the average particle size from the width of the diffraction peak:

$$d = \frac{K\lambda}{FWHM\cos\theta} \qquad (9)[119]$$

where:

λ = wavelength of the X-ray

θ = the angle at the maximum of the peak

K = a numerical constant with a value close to 0.9

FWHM = full width at half maximum of peak, in radian

Lattice parameters ($a_{fcc}$) are calculated using the equation:

$$a_{fcc} = \frac{\sqrt{2}\lambda}{sin\theta} \qquad (10)^{119}$$

A derivation of the Scherrer equation is Vergard's law (equation 9). This equation describes the relationship between the composition of an alloy and its lattice parameter; for example if an element with larger atoms is substituted into a pure metal to create an alloy, this alloy will have a larger lattice parameter than the initial pure metal and this value will increase linearly with increasing concentration of the substituent element. This law simply states that the cell parameters are a consequence of the atomic size of the component metals.

$$a = a_A^0\,(1 - X) + a_B^0\,(X) \qquad (11)^{120}$$

where:

$a_A^0$ and $a_B^0$ = the lattice parameters of the pure components A and B

X = the mole fraction of component B

## X-ray fluorescence *(XRF)*

X-rays characteristic of specific elements are emitted by an atom when a bound electron is ejected from an orbital by an incident electron. The atom is then unstable and may decay via either X-ray fluorescence or Auger decay; these are competing processes.[118] XRF occurs when an electron from a higher shell fills the core hole, for example an electron from an L shell fills a hole in a K shell. $E_K$-$E_L$ describes the energy change for this process and this energy is used to emit an X-ray characteristic for the atom from which it has been emitted (see Figure 9). The process results in release of a photon of energy equal to the difference between the two orbitals. The energies of orbitals are characteristic for certain elements, therefore XRF can give the amounts of each element present in a sample; this technique was used to obtain accurate percentages of Pt and alloy metals in the nanoparticles.[121]

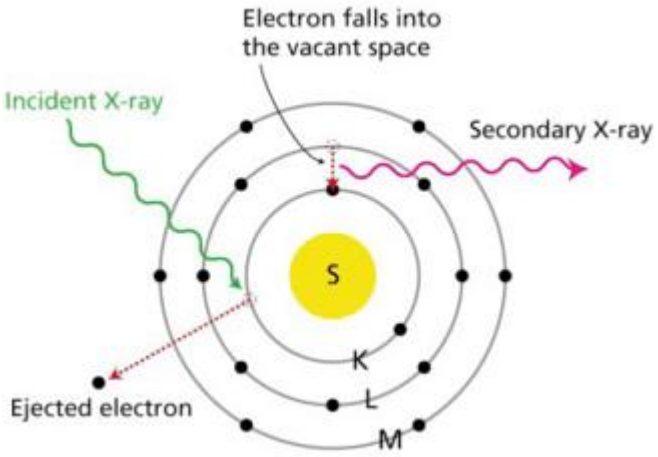


**Figure 9.** Diagram to show the process of X-ray fluorescence.[122]

## X-ray photoelectron spectroscopy *(XPS)*

Herz was the first to report a photo emission experiment in 1887. Since this was prior to the discovery of the electron, it was not fully understood at the time. A decade later, Thomson proposed that electrons were causing the observed radiation in Herz's experiments. Matter emits electrons when irradiated with light of a short wavelength; this is known as the photoelectric effect (equation 9) and is the basis of photo emissive techniques such as XPS. This effect can be described by the following equation (and Figure 10), which basically states that a photon with energy of $hv$ is absorbed by an atom and an electron of binding energy $E_b$ is ejected.

$$E_k = hv - E_b - \varphi \qquad (12)^{118}$$

where:

$E_k$ = kinetic energy of a photo electron

$h$ = Planck's constant

$v$ = frequency of exciting radiation

$E_b$ = binding energy of the photo electron with respect to the Fermi level of the sample

$\Phi$ = the minimum energy needed to remove an electron from a solid

Information obtained from XPS includes elemental composition and oxidation state. Composition may be analysed since binding energies are characteristic of certain elements. Binding energies also change with oxidation state of the element; in general they increase with increasing oxidation state since electrons feel a higher attractive force from the nucleus in a more positively charged ion.

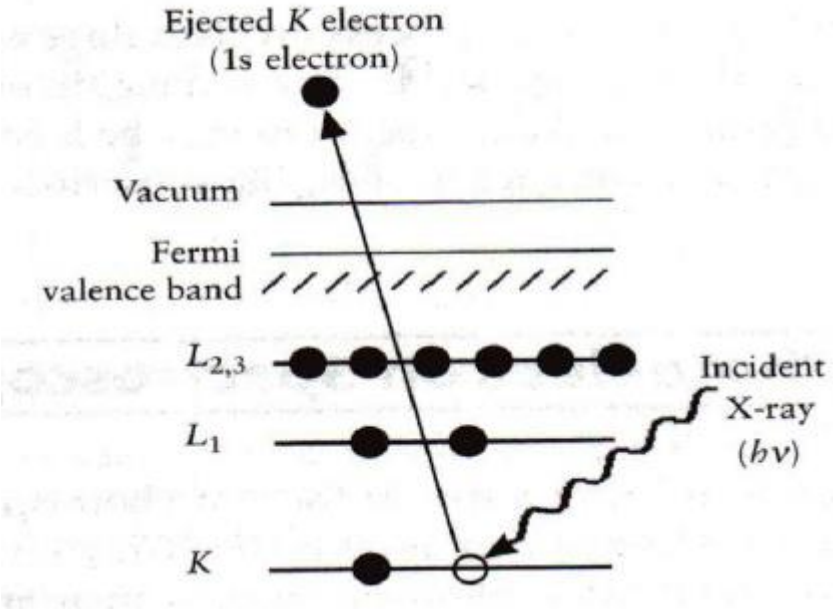


**Figure 10.** Diagram to show the principle of XPS.[123]

The expression for describing the intensity of an XPS peak is shown by equation 13 as follows:

$$I = F_x\, S(E_k)\, \sigma(E_k) \int_0^\infty n\,(z) e^{-z/\lambda(E_k)cos\theta}\; dz \qquad (13)^{118}$$

where:

$I$= peak intensity

$F_x$= X-ray flux

$S(E_k)$= Transmission function (efficiency of spectrometer for detecting the electron of kinetic energy, $E_k$)

$\sigma(E_k)$= photoemission cross section

$n\,(z)$= concentration (number of atoms per unit volume)

$z$= depth below surface

$\lambda(E_k), z$ =mean free path of photoelectron of energy $E_k$through the material at depth $z$

$\theta$= angle between emission of photoelectron and surface normal

### 2.6.2.1 Microscopy and related techniques

Electron beams are more useful than optical microscopy in the field of catalyst analysis, since optical microscopes cannot detect features less than 1 µm in size due to the long wavelength of visible light. Over the past half century, developments in electron microscopy have resulted in improved magnifications of $10^6$ times with a resolution of 0.1 nm. Electron microscopy is a technique used to determine shape and size of particles; it may also give additional information of elemental composition and internal structure. The properties of metals and alloys are affected by their structure. For this reason, electron microscopy is an important tool for analysis.[118] Electron microscopy has enjoyed much attention through various applications in the literature and some very good reviews are available.[124,125]

### Transmission electron microscopy *(TEM)*

A TEM emits a beam of electrons, which are accelerated through an electromagnetic field, helping to focus the beam. The electrons produced are from a heating filament (usually tungsten) at a voltage of 60-120 kV and are fired through a vacuum towards the sample. Samples must be thin enough (<100 nm) to allow electrons to pass through, after passing through the sample the electrons can then produce an image. Attenuation of the beam is affected by thickness and density of the sample, therefore the transmitted electrons result in a two-dimensional image. Bright areas correspond to those where the sample is less dense, as more electrons are able to pass through, whereas dark areas correspond to areas of higher density. TEM allows the arrangement of atoms in a sample to be seen due to its resolution of 0.2 nm, which is smaller than the size of most atoms.[118] For this work TEM was used to help understand catalyst composition and morphology. Features such as dispersion and nanoparticle size and shape can be obtained; this allowed us to correlate such properties to catalytic activity.

## Scanning electron microscopy *(SEM)*

In contrast, SEM involves an electron beam being scanned over a surface and the amount of backscattered electrons as a function of the beam position is recorded, (see Figure 11). This gives information about composition, since heavier elements scatter more electrons than lighter elements. Orientation of the surface of the sample causes contrast; those parts facing the detector look brighter than those facing away.

Unlike the TEM, where the electrons in the primary beam are transmitted through the sample, the SEM produces images by detecting secondary electrons which are emitted from the surface due to excitation by the primary electron beam. In the SEM, the electron beam is scanned across the surface of the sample. Because the SEM image relies on electron interactions at the surface rather than transmission it is able to image bulk samples and has a much greater depth of view, and so can produce images that are a good representation of the 3D structure of the sample. SEM images are therefore considered to provide us with 3D, topographical information about the sample surface.[118]

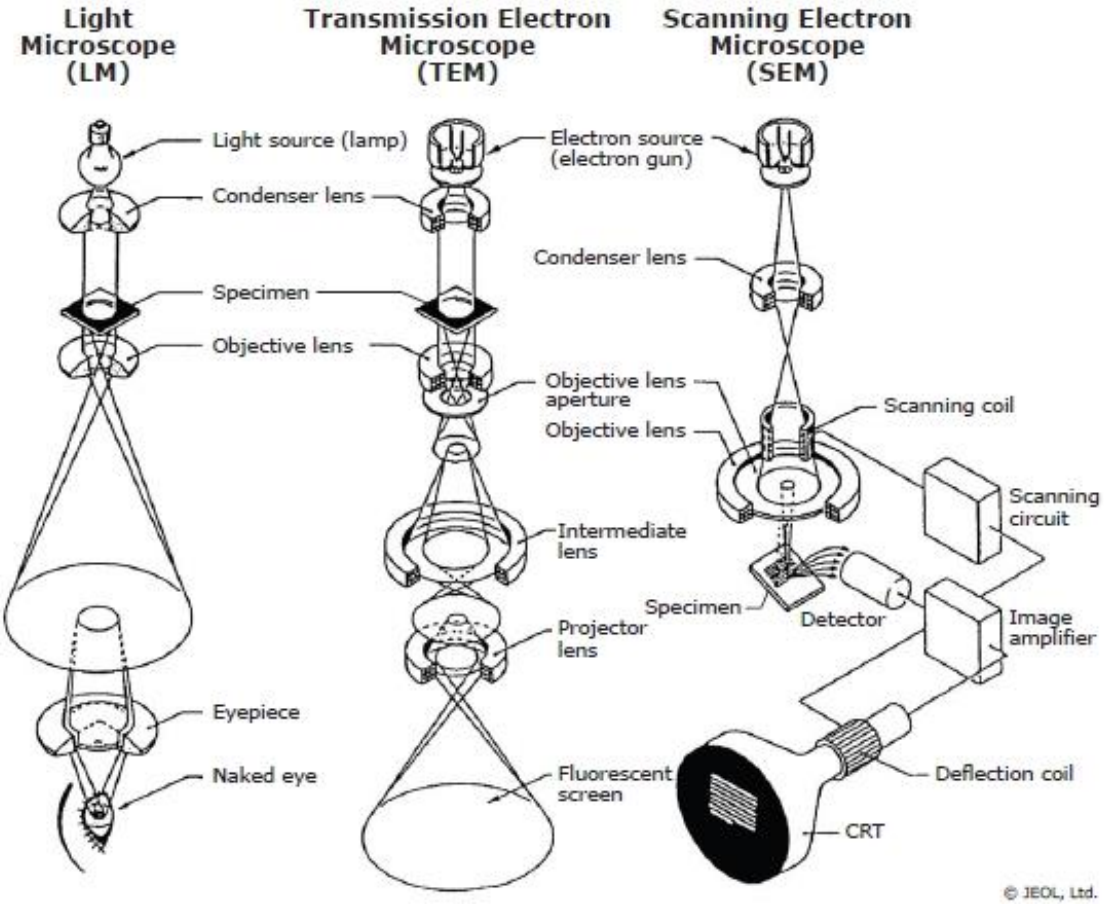


**Figure 11.** Schematic representation of the cross-sections of a light microscope compared with a transmission and scanning electron microscope (JEOL).[126]

## Energy dispersive X-ray analysis *(EDX)*

An additional feature of an electron microscope is that it is able to collect diffraction patterns. Similarly to XPS (Section 2.6.1.1.3), elemental composition may be determined since the X-rays emitted are characteristic of certain elements. EDX was used in this study to investigate whether all areas of catalyst had the same elemental composition and to confirm results from XRF analysis.

Figure 12 below shows the internal set up of an EDX experiment. The energy dispersive detector is made of semi-conducting lithium doped silicon and is at a fixed position in relation to the sample. Upon conversion of an X-ray into an electron, the electron's energy is dissipated by creation of electron hole pairs in the detector. The amount of electron hole pairs is shown by the pulse height of the current, which can be measured upon application

of a voltage over the detector. Therefore pulse height is a measure of the $E_k$ of the photoelectron. The crystal, which is usually quartz or lithium fluoride, separates the emitted X-rays. Both crystal and detector are moved over the Rowland circle in order to produce a spectrum; this circle allows a range of Bragg angles to be covered.

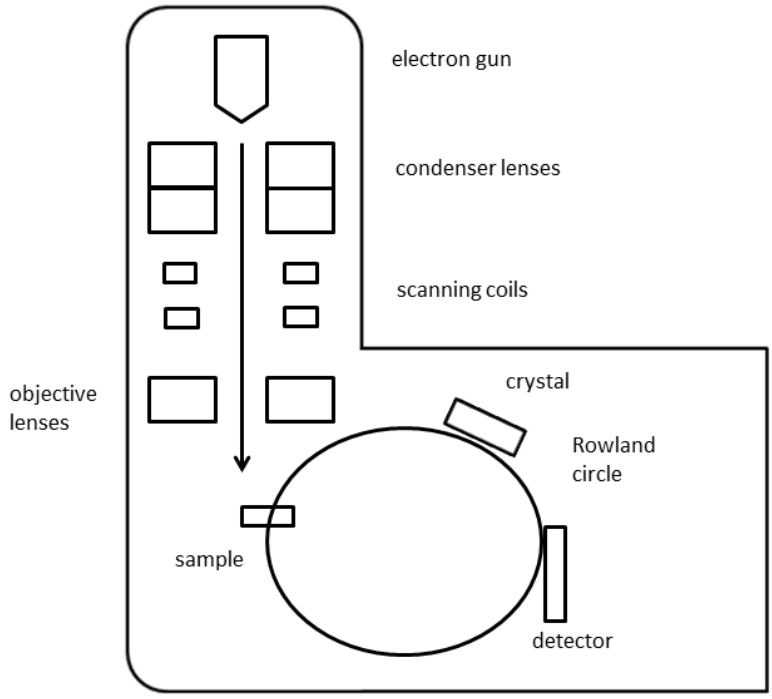


**Figure 12.** Schematic representation of the set up for EDX analysis.

## 2.6.2 Electrochemical Characterisation

After initial physical characterisation, catalyst samples were characterised electrochemically. Electrochemical characterisation involves study of the chemical response, in particular the gain or loss of electrons in a system, as a response to an electrical stimulus. Electrochemical experiments involve measurement of one of four parameters including current, time, charge and potential. The techniques discussed here will include potentiostatic techniques cyclic voltammetry (CV) and chronoamperometry (CA), in which the controlled parameter is potential, whereas current is the parameter being measured. A brief introduction to electrochemical mass spectrometry will also be covered.

## Inner Sphere reactions

Inner sphere (IS) and outer sphere (OS) reactions were distinguished by Taube in 1970.[127] These processes both involve electrons transfer, but the mechanism by which they do this differs. For outer sphere reactions, electron tunnelling occurs between two un-bonded species. Whereas inner sphere reactions involve the presence of an activated complex in which a shared ligand is present between donor and acceptor. Following this general explanation, it is more noteworthy to apply this to heterogeneous reactions such as those studied in this work. These explanations can be adapted as follows.

Another way these two processes differ is by the strength of interaction of reaction species with the electrode and the dependence of the reaction on the particular electrode material. In outer sphere reactions, no such strong interaction is present and the reaction is insensitive to the electrode material, whereas in inner sphere, species interact with the electrode strongly and exhibit strong dependence on the specific electrode material.[128]

When an intermediate is adsorbed strongly to an electrode surface, the potential is shifted by an amount related to the free energy of adsorption. In IS reactions, reactants can interact strongly to the extent that bonds are broken and formed. This explains why the multi-electron pathway is thermodynamically feasible even though the direct pathway is not, due to high ionisation potentials.

Inner sphere reactions will now be discussed in terms of the formic acid oxidation. It is known that CO adsorbs strongly on Pt and does not dissociate due to the strength of the triple bond. This means that other species must be formed on the surface to complete this oxidation of CO. OH radicals and adsorbed O atoms may be produced through oxidation of $H_2O$, which are capable of reacting with adsorbed species on the electrode through reactions which are independent of ionisation potential. In a similar sense, CO stripping on Pt is known to occur via the Langmuir-Hinshelwood mechanism since two different adsorbents react.[128]

### 2.6.2.1 Cyclic voltammetry *(CV)*

CV is a commonly used technique for characterisation of an electrode surface. This technique involves use of a potentiostat to measure the current response between the counter and working electrode as a function of applied potential between the reference and working electrode which is increased linearly with time. The reference electrode controls the potential of the working electrode. One advantage of using a three electrode cell is that errors due to Ohmic and iR losses are minimised.[129] The potential applied across the reference and working electrodes is called the excitation signal, this is in the form of a linear scan with a triangular shaped waveform. As can be seen from Figure 13, this triangular signal is responsible for sweeping the potential between two values; these values are called the switching potentials. In this case it is 0.8 and -0.2 V and the reference used is a saturated calomel electrode (SCE).

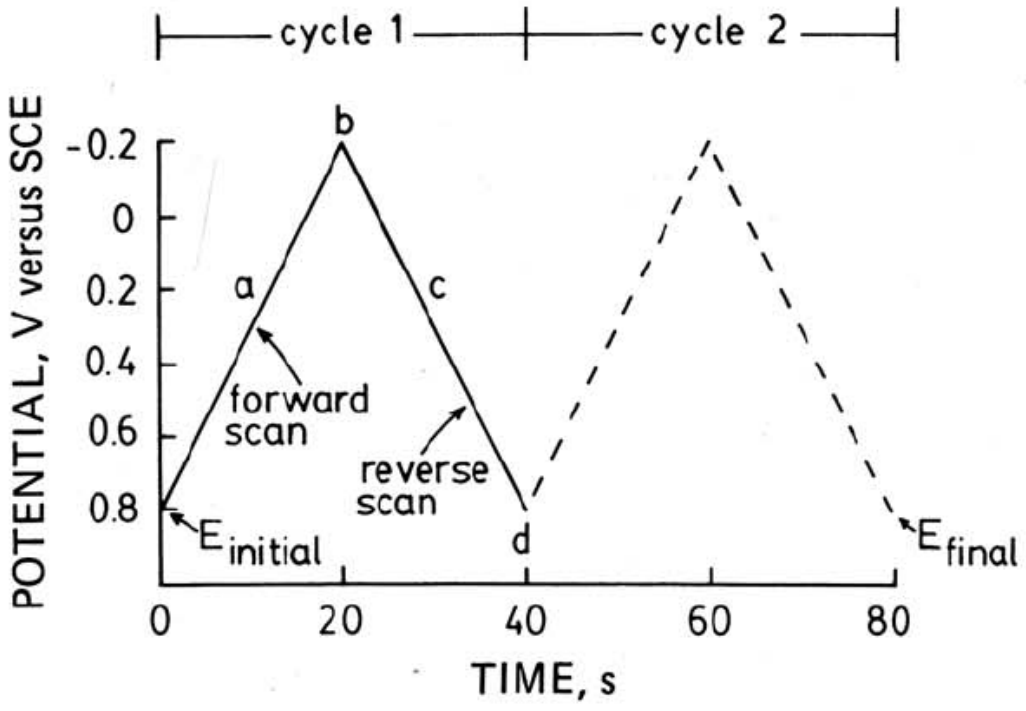


**Figure 13.** Figure to show the excitation signal for cyclic voltammetry with the triangular waveform and switching potentials.[130]

The current response at the working electrode is measured as the potential is scanned to produce the voltammogram, a plot of current (y axis) versus potential (x axis). The maths behind a cyclic voltammetry experiment is complex, however Fick's First Law of Diffusion

tells us that at time, t, the current will be proportional to the concentration gradient of the reactant, as in equation 14:

$$i_t = n\,FAD_0\,(\partial C_0/\partial x)_x\ = 0, t \qquad (14)^{129}$$

Where:

$n$ = number of electrons transferred per molecule

$F$ = Faraday's constant

$A$ = area of electrode

$D_0$ = diffusion coefficient of oxidised species

$C_0$= concentration

$x$ = distance from surface of electrode

#### 2.6.2.1.1 Reversible and irreversible systems

Electron transfer can be rapid or slow. In electrochemistry, the term reversible can be used to describe a system in which electron transfer is rapid enough to maintain the equilibrium concentration of the oxidised and reduced species at the surface of the electrode. At a certain potential, the equilibrium ratio of these species is given by the Nernst equation in equation 15:

$$E = E^{0\prime} - \frac{RT}{nF} ln\left(\frac{[R]}{[O]}\right)\ x = 0 \qquad (15)^{129}$$

where:

$R$ = the gas constant

$[R]$ = concentration of the reduced form

$[O]$ = concentration of the oxidised form

One feature of a reversible system is relationship between the peak height and the square root of the scan rate. At 25 °C, it is shown by the Randles-Sevcik equation (equation 16) that:

$$i_p = (2.69 * 10^5) n^{3/2} A D_0^{1/2} v^{1/2} C_0^* \quad (16)^{129}$$

where:

$i_p$= peak current, in Amperes when A is in $cm^2$

$C_0^*$ = bulk concentration

V = scan rate in Volts/s

(units of D are $cm^2$/sec)

The formal reduction potential for a reversible process is given by equation 17:

$$E^{0\prime} = (E_{pa} + E_{pc})/2 \quad (17)^{130}$$

For a quasi-reversible system, peak height is not proportional to the square of scan rate apart from in the situation where the peaks are widely separated enough for the system to be more accurately described as irreversible. Electrochemical irreversibility is caused by slow electron exchange between the working electrode and redox species. Such a system is characterised not only by slow electron transfer, but also by a larger separation of peak potentials than given by the following equation in equation 18:

$$\Delta E = E_{pa} - E_{pc} \cong \frac{0.059}{n} \quad (18)^{130}$$

where:

$E_{pa}$= anodic peak potential

$E_{pc}$ = cathodic peak potential

For irreversible systems, the Randles-Sevcik equation does not apply, equally the following relationship between the anodic and cathodic currents also applies exclusively to reversible systems. It states that the values for each of the currents should be around identical, therefore giving a ratio equal to 1 (Equation 19):

$$\frac{i_{pa}}{i_{pc}} = 1 \qquad (19)^{130}$$

With a completely irreversible electrode reaction, just one peak, for example the reduction peak, when the oxidized form is present in the solution, will be visible. The following equation (equation 18) shows how the cathodic peak potential is affected by the formal potential:

$$E_{pc} = E_c^{\circ} - \frac{RT}{\propto nF}\,(0.780 + 0.5\ln\frac{\propto nD_{ox}Fv}{RT} - \ln k_s \qquad (20)^{131}$$

where:

$k_s$ = the standard rate constant of the electrode reaction

α = the transfer coefficient

$D_{ox}$ = the diffusion coefficient

### 2.6.2.1.2 Blank voltammograms

So called 'blank' voltammograms recorded under controlled conditions in the absence of reactants give information on the purity of the electrode-electrolyte interface and composition of the electrode (for example, pure metal or alloy and characteristic shapes for different metals).

The current response is characteristic of a certain material but can also depend on the electrolyte to some extent. Peaks and troughs in the current signal correspond to oxidation and reduction, respectively, at the voltage at which the species experiences these reactions. Figure 14 below shows a voltammogram typical of a polycrystalline Pt electrode recorded in 0.5 M $H_2SO_4$ using a reversible hydrogen electrode.

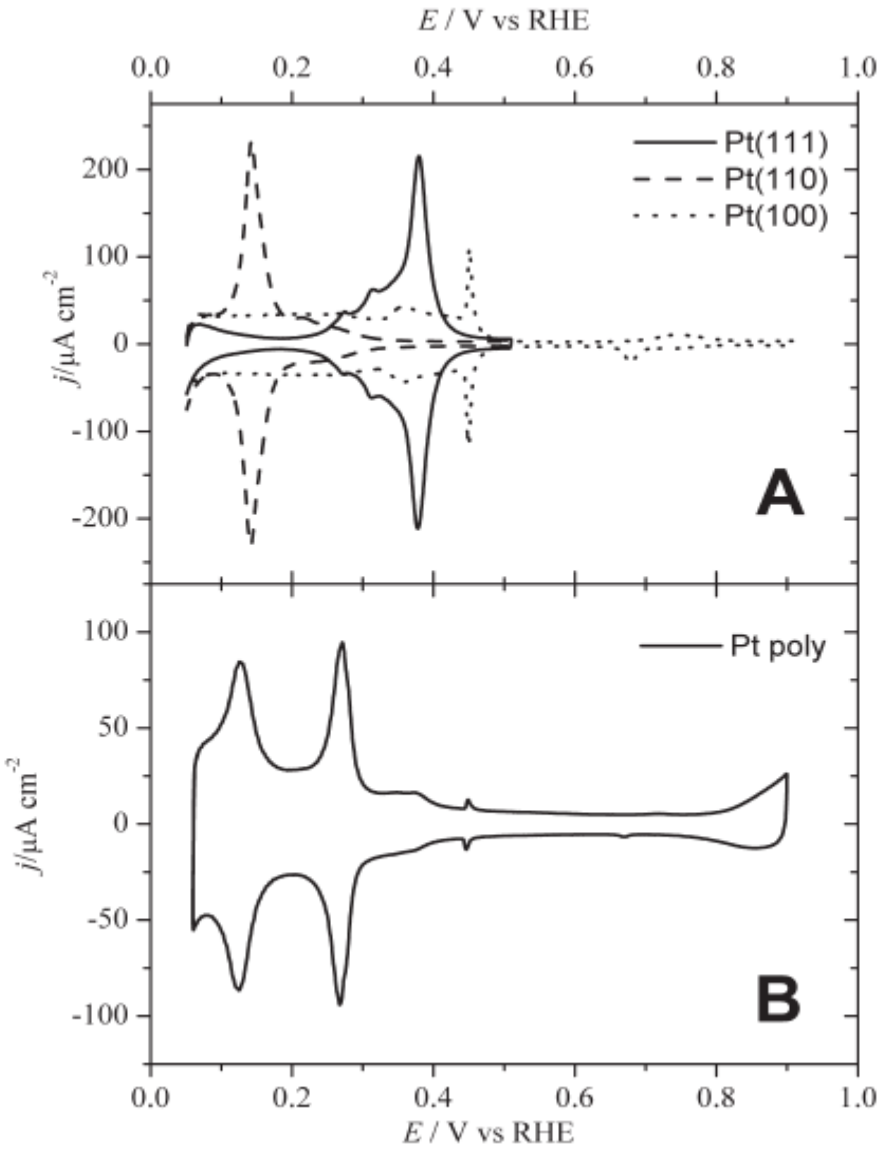


**Figure 14.** Voltammetric profiles of the Pt(111), Pt(100), Pt(110) and polycrystalline Pt electrodes in 0.5 M $H_2SO_4$ at a scan rate of 50 mV/s.[132]

In Figure 14, the various peaks corresponding to hydrogen adsorption and desorption are due to the different surface arrangements of Pt (100), (110) and (111) sites. This is because the different orientations result in different adsorption peaks which can then be correlated to the different sites present on the polycrystalline platinum (see Figure 14, A). Two pairs of reversible redox peaks can be seen which are due to the stripping of a monolayer of hydrogen. The first redox couple appears at 0.12 V which shows weakly adsorbed hydrogen, whereas the second redox couple at 0.28 V vs RHE is indicative of strongly adsorbed hydrogen.[132]

Figure 15 below depicts the setup used for a cyclic voltammetry experiment in this study with the electrodes clearly labelled. A three electrode cell (~60 ml) controlled by an Autolab potentiostat was used for the experiments, nanoparticles are deposited on a glassy carbon working electrode and this is in contact with the solution in the meniscus configuration.

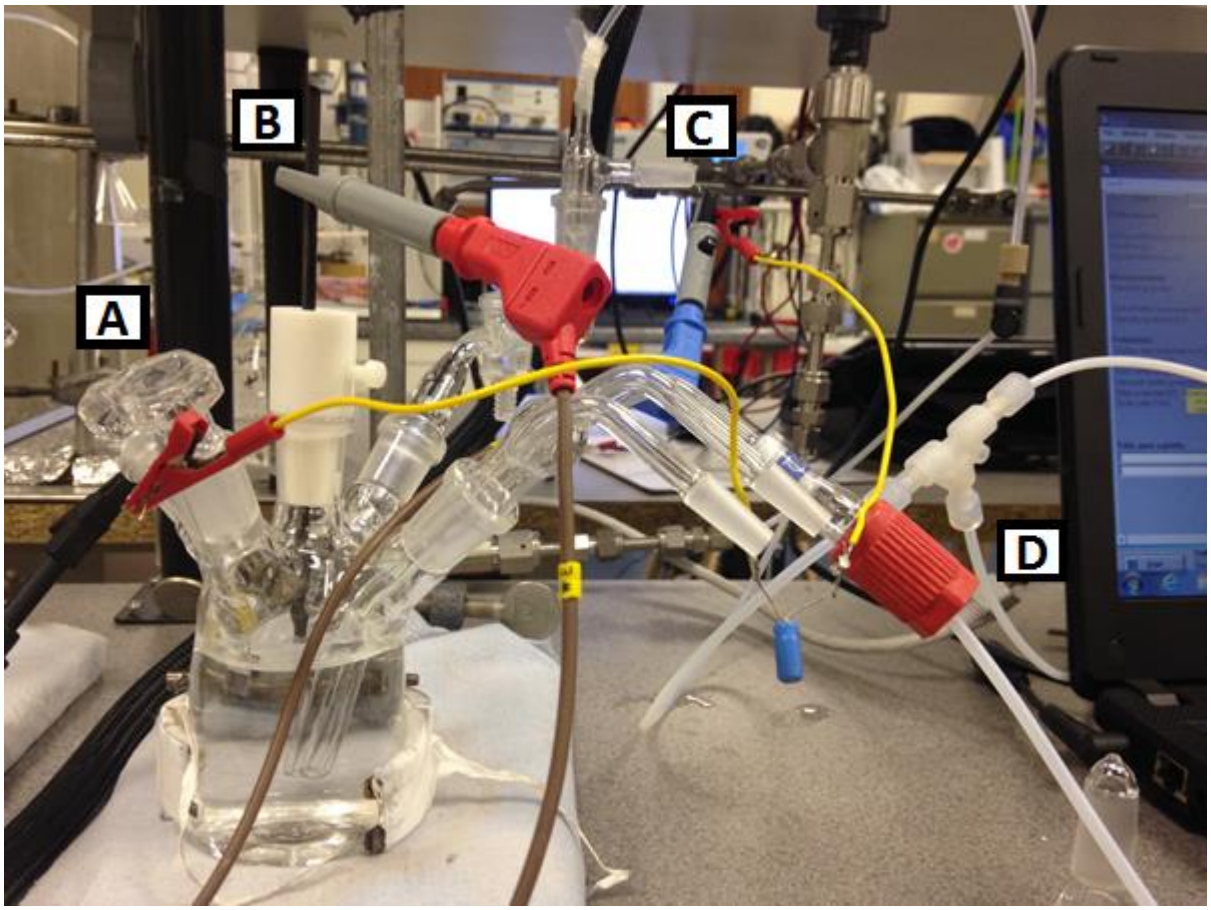


**Figure 15.** Experimental setup of a cell for cyclic voltammetry experiments showing (A) the gold counter electrode, (B) the working electrode, (C) the reference electrode which is a platinum wire with hydrogen gas bubbled through the solution and (D) the argon gas inlet which is connected to the bubbler.

#### 2.6.2.1.3 Cyclic voltammograms

Voltammograms in the presence of reactants provide information on how a catalyst affects onset potential and current of a particular reaction.

### 2.6.2.2 Online electrochemical mass spectrometry

Online electrochemical mass spectrometry (OLEMS) can be used to detect products and intermediates formed in Faradaic reactions, in this work the technique was used to detect the gaseous products formed. In an OLEMS experiment, the ion current corresponding to the species of interest is measured along with the Faradaic current; this produces the resulting mass spectrometric cyclic voltammogram (MSCV). All mathematical analysis in this section (equations 21-24) is adapted from work by Baltruschat.[133] The ion current provides information on the rate of formation of products and the ion intensity from the MS is related to the incoming flow as shown by the expression in equation 21 below:

$$I_i = K^0 J_i \qquad (21)^{133}$$

where:

$I_i$= ion intensity

$K^0$= accounts for setting of MS and the ionisation probability of the species

$J_i$ = incoming flow in mol/s

The equation below shows the relationship between the mass spectrometrically determined ion current and the Faradaic current (equation 22):

$$I_i = (K^*/z)\, I_F \qquad (22)$$

where:

$I_i$ = ion current

$I_F$ = Faradaic current

$z$ = number of electrons

And

$K^* = K^0 N/F$ (23)

where:

$K^0$= the ionisation probability and takes into account the setting of the MS

$N$= transfer efficiency (ratio of the species detected by the MS to the amount produced in the cell)

$F$= Faraday constant

N can be smaller than 1 since some of the species will diffuse into the electrolyte.

The ion intensity determined by the MS is directly proportional to the partial pressure of the species concerned:

$$I_i = ap_i = aJ_i' /S = RTJ_i\, a/S = K^0 J_i$$ [133] (24)

where:

$a$ = the proportionality constant which accounts for the settings of the MS and the ionisation probability

$p_i$ = partial pressure of species i

$J_i'$= the inflow rate

$S$ = pumping speed

## 2.6.3 Chronoamperometry

Chronoamperometry (CA) is the study of current as a function of time, for a diffusion-controlled current, the current-time (i-t) curve is described by the Cottrell equation (equation 25):

$i = nFACD^{½}\pi^{-½}t^{-½}$ (25) [129]

where:

n = number of electrons transferred per molecule

F = Faraday's constant (96,500 C $mol^{-1}$)

A = electrode area ($cm^2$)

D = diffusion coefficient ($cm^2\ s^{-1}$)

C = concentration (mol $cm^{-3}$)

The waveform used for this technique is a very simple one, the potential step. Only single potential step experiments were conducted in this study, during a single potential step experiment, the potential is changed from an initial potential to a first step potential, and it is held at this value for an amount of time, t. Our initial potential was 0.06 V and after 5 seconds, the potential was increased to 0.3 V and held at this potential for 2700 s. The potential was then decreased back to 0.06 V for 10 seconds before the experiment was stopped.

Applications of CA include determining the diffusion coefficient of the electroactive species, determining the surface area of the working electrode, study of mechanisms of electrode processes and study of the stability of a catalyst over time. CA was used for the latter application in this thesis. For a process that is under diffusion control, current decreases with $t^{-1/2}$. The diffusion coefficient can be calculated from the gradient of a plot of current versus $t^{-1/2}$.

With this technique, it is essential that current is monitored over a relatively long time span as this ensures that results obtained are reliable since at short time windows, non-Faradaic currents dominate due to charging of the double layer capacitance. The non-Faradaic current is current that is not as a result of a redox process. This current exhibits an exponential decay as shown below in equation 23:

$$I = E\ /R_u\, e^{-t/R_u C_d} \qquad (26)^{134}$$

where:

$R_u$= uncompensated resistance

$C_d$= double layer capacitance

The shortest time needed to perform a chronoamperometric experiment is dictated by the term '$R_u C_d$.' Capacitive processes arise during discharge or charging of an electrode surface which can be caused by variation in the applied potential or from adsorption. Capacitive processes or capacitive current is also referred to as non-Faradaic current or double layer current. This current simply involves the build-up or removal of charge on the electrode and in the surrounding solution. Capacitive current, unlike Faradaic current, flows even when the potential is maintained constant. This can be as a result of fluctuation in temperature or change in adsorption processes. The charging process is usually rapid and the associated current ceases in less than a second unless the electrolyte used has a high resistance. The time taken for this current to lapse is proportional to RC. However, the time must also not be too long as convection caused by concentration and temperature gradients can affect the results. For the experiments in this thesis, times of around 3000 s were used and a rotating disk electrode was used to minimise concentration gradients.

To summarise this section, cyclic voltammetry is a useful method for obtaining qualitative information about electrode processes. Its advantages are its good sensitivity, variable timescale and that it allows a rapid scanning over a large potential range. However, CV is not without its limitations and quantitative information, such as rates, is better gained through methods such as pulse or step techniques. Solid electrodes such as carbon and platinum are frequently used when performing oxidation reactions, however such electrodes are subject to surface oxidation and poisoning by strongly adsorbing species as has been discussed previously. CA and OLEMS are useful complementary techniques that can be compared with voltammetry results to provide a much more complete analysis to better understand the system under study.

# Chapter 3

# PtBi and PtPb nanoparticles as catalysts for the formic acid oxidation

## 3.1 Introduction

### 3.1.2 Discussion of the dual pathway mechanism

The formic acid oxidation takes place via a dual pathway mechanism as proposed by Capon and Parsons in 1973.[135] This shows that the reaction can be considered to go via a direct route via an active intermediate or an indirect route through a poison intermediate, CO (Figure 16).

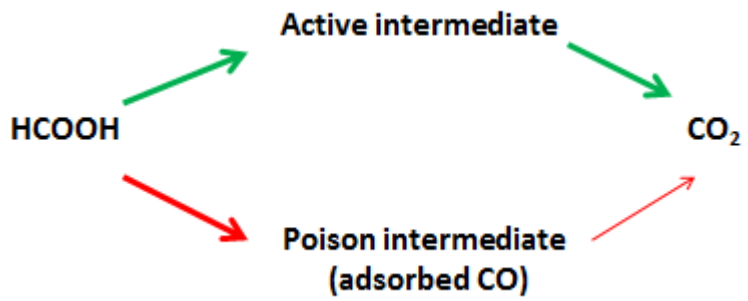


**Figure 16.** Schematic to show the nature of the dual pathway of the formic acid mechanism.

Figure 17 below shows a voltammetric profile for the electro-oxidation of formic acid on Pt, several of the main important features will be discussed.

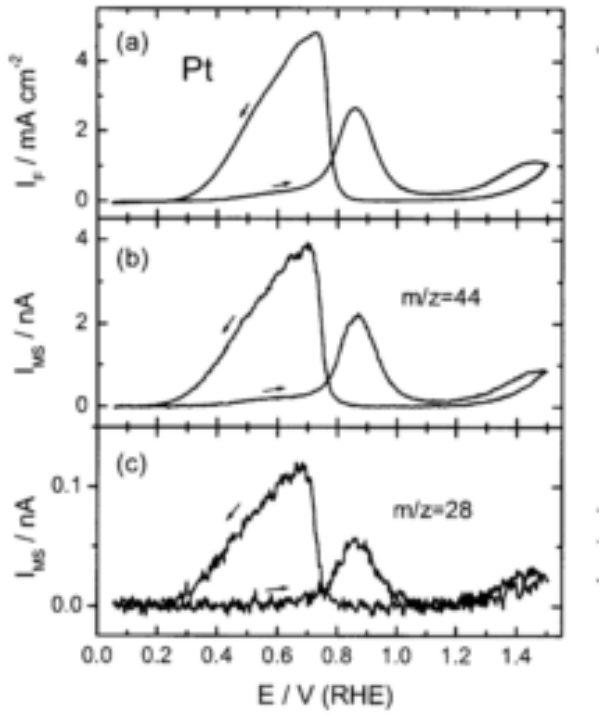


**Figure 17.** Cyclic voltammogram (a) and mass spectrometric cyclic voltammograms at m/z 44 (b) and m/z 28 (c) for the oxidation of formic acid on polycrystalline Pt in 0.1 M $H_2SO_4$ and 0.1 M HCOOH at 10 mV/s.[136]

The oxidation of formic acid can be observed at potentials as early as 0.2 V vs RHE. From the voltammogram we can see several things, firstly that the hydrogen adsorption states in the adsorption/desorption region are not defined; this suggests that they are in fact blocked by adsorption of a species (the poison intermediate) on the surface of the electrode. Further to this, the activity of the forward going scan is less than that of the reverse scan; this can be explained by the fact that CO adsorbs on the surface between 0.2 and 0.7 V in the forward scan. Above 0.7 V, the CO is oxidised to $CO_2$ and on the reverse scan the surface of the Pt is completely fresh since PtO has been reduced back to Pt and the CO has also been removed, resulting in a higher catalytic activity. A hysteresis is also observed on the voltammetric profile, this signifies accumulation of CO at low potential followed by its oxidation at higher potential (above 0.7 V).

The rate of poisoning also differs for each of the Pt surface orientations and follows the order: Pt(110)>(100)>(111).[137] The reaction was further studied in the absence of CO; this was carried out by either modifying the surface in such a way to prevent the formation of

CO or by removing CO before the study. The first study of this type was performed using pulse voltammetry by the Clavilier group.[138] He found that the Pt(100) site was exceptionally active for the electro-oxidation of formic acid.

A discussion of the two separate paths of the formic acid oxidation will now be presented. The mechanism of the indirect path will be examined first. CO was observed by electrochemically modulated infrared spectroscopy (EMIRS) and FTIR and hence it was proven to be the intermediate responsible for poisoning of active sites by the indirect route.[139,140] Evidence that CO is in fact the poison intermediate and not the active one was given by differential electrochemical mass spectrometry (DEMS) studies.[139] In these experiments, $^{13}C$ labelled formic acid was used. The solution was then replaced with $^{12}C$ formic acid after the maximum amount of CO was formed and the potential was increased. It was found that there was a route via an active intermediate which could not be CO, since the $^{13}C$ labelled carbon dioxide was detected later than the $^{12}CO_2$. The reaction scheme via the indirect route can be written:

$$HCOOH + * \rightarrow CO_{ads} + H_2O \rightarrow CO_2 + 2H^+ + 2e + * \qquad (27)$$ [141]

where * is a vacant site.

The rate determining step (rds) of this route is that which produces the active intermediate. Proceeding formation of this intermediate, the reaction to produce $CO_2$ happens a lot more quickly meaning that the intermediate is short-lived thereby making its detection difficult. Pt bonded COOH was the first species proposed as the active intermediate by Sun et al.[140] from EMIRS experiments on Pt(111) and Pt(100) electrodes.

The mechanism of the direct route, in particular the identification of the active intermediate and the role of adsorbed formate, has been at the centre of much debate. CHO, HCOO and COOH have also been suggested as possible intermediates.[142] Cuesta et al.[143] argue that this species is indeed the intermediate for the loss of water from formic acid to form adsorbed carbon monoxide. This paper details the oxidation of formic acid on Au and Pt electrodes using a spectroscopic technique, ATR-SEIRAS (Attenuated Total Reflection-Surface Enhanced Infrared Absorption Studies), to reveal information about the mechanism. The mechanism

of the formation of the poisoning CO on Pt through oxidation of formate followed by reduction to CO is proposed in this article:[143]

$HCOOH_{aq} \leftrightarrow HCOO_{ad} + H^+ + e$ (28) (rds)

$HCOO_{ad} + H^+ + e \rightarrow CO_{ad} + H_2O$ (29)

In summary, Cuesta et al.[143] suggested that the formation of this bridge-bonded formate species is the point where the reaction can branch and go down either a direct or indirect route. This is the place to target for design of new catalysts with higher activity and tolerance to CO.

On the contrary, a paper published by Chen et al.[144] suggests the existence of another active intermediate which was not detected. FTIR and electrochemical methods indicate that this unknown intermediate is responsible for nearly 90 % of the carbon dioxide produced through the direct route. The mechanism of this reaction on Pt is still uncertain and requires further experimental and theoretical studies.[142]

The following will discuss use of DFT theory in the process of elucidating the reaction mechanism of the formic acid electro-oxidation. First of all, a very brief, simple summary of DFT will be given. Density functional theory is a computational method used to investigate electronic structure and validate experimental investigations. It can be used to calculate geometry and energy, model structures and processes, determine mechanisms and spectroscopic properties.[145] A mechanism cannot be validated solely by computed energies from DFT; it should also be backed up by experimental evidence such as spectroscopy. Lastly, before the discussion, it will be stated that the reason behind the mechanism being so elusive is that the intermediates for the direct and indirect pathways compete with each other for adsorption sites and the chance to react with oxidisers such as OH at the surface.

Many theoretical studies have been conducted on the pathways of the formic acid oxidation with the end goal of finding out exactly what the intermediate for the direct route is. The discussion below of how theory links to experimental findings and the results concerning the mechanism of the formic acid oxidation will focus mainly around the work published by

the Jacob team. In these articles, the formic acid oxidation on Pt(111) was studied. First of all, it is worth mentioning that the results of the computational simulations and calculations differ to an extent, meaning the predictions of the mechanism also differ. Differences in the literature have mainly been focused around the prediction of the most stable conformation of HCOOH and the active intermediate. The following will briefly discuss the adsorption configuration of formic acid, the mechanism and the roles of CO and OH.
Gao et al.[146] found the most stable configuration of HCOOH (without water) to be that where the carbonyl oxygen binds in the atop configuration with the OH pointing at the surface. This agrees with other similar theoretical studies in the literature.[147,148] With regards to the exact mechanism, the pathway with the lowest energy barrier is referred to as the minimum energy pathway (MEP). Gao et al. predicted that HCOOH decomposes to $CO_2$ and 2H via the active intermediate HCOO. This pathway was found to be exothermic and therefore thermodynamically favoured, although it is kinetically hindered by a significant activation barrier $Ea_{act}$ = 2.49 eV.[149] This barrier is, however, smaller than that calculated for the reaction HCOOH → CO + $H_2O$, which reaches the conclusion that HCOOH preferentially forms $CO_2$ and 2H. This agrees with experimental results.[150, 151,152, 153]

In summary, the pathway involving HCOO has the smallest activation barrier and is the MEP. This agrees with the results from Osawa[143] and Feliu[154] in the literature. To properly understand the individual pathways, we need to look into the specific roles of the species involved. This next section will discuss the findings of the Jacob team[155] on the roles of adsorbed CO and OH in the formic acid oxidation, as a means to look in more detail at the mechanism. To do this, they co-adsorbed fractional coverages of CO, OH and a mixture of both with solvated HCOOH. The focus was on the kinetically dominant pathways, the direct and formate routes. Different surface coverages of CO and OH result in different possible reaction steps. Focusing on CO first, it may adsorb in either a linear ($CO_L$) or bridge-bonded ($CO_B$) geometry. The coverage of linearly bonded CO is strongly affected by applied potential, whereas the coverage of bridge bonded CO is unaffected by the applied potential. They chose to focus their efforts solely on linear boned CO.

The Jacob team[155] found that surface-bonded OH induces a positive charge across the Pt surface, this is thought to activate HCOOH oxidation by decreasing the energy barrier for C-

H bond cleavage. The positive charge induced by CO is situated directly below that for OH.[147] OH and CO act in synergy through their effect of charge induction and alteration in the hydrogen bond network. Alone, CO is known to have an adverse effect on the oxidation reaction, whereas OH has very little effect. At high potentials, OH is known to oxidise the Pt surface, thereby acting as a poison by blocking active sites. In summary, the findings were that together, OH and CO are thought to facilitate the direct pathway at relatively low coverages between 0.00 and 1.2 V, due to increasing the energy barriers for the formate pathway.[155]

In conclusion, from the evidence gathered, it seems highly likely that the active intermediate is indeed formate (HCOO). The mechanism controversy is not something which can be solved on experimental results alone, more detailed calculations are needed to elucidate the 'true' mechanism. Not many studies have been conducted on the $Pt/H_2O$ system since the modelling of interactions between a solid and liquid interface is fairly difficult. Experiments use rough surfaces, which must be remembered when comparing experiment to theory. In addition to this, not every effect can be considered by DFT and errors exist for certain calculations. However, as technology continues to advance, techniques will improve and better spectroscopic and modelling tools will be available to shed more light on such areas.

### 3.1.3 Oxidation of formic acid on PtBi electrodes

The phase diagram of the PtBi system (Figure 18) was reported by H. Okamoto in 1991.[156] This demonstrates the difficulty of preparing this alloy at ambient temperatures, as can be seen from the figure below, temperatures of ~700 °C were required to obtain the alloy. PtBi and PtPb alloys are difficult to prepare, since they do not exist as alloys in bulk materials. Herein, a novel method for preparation of these non-conventional alloys under room temperature conditions is presented.

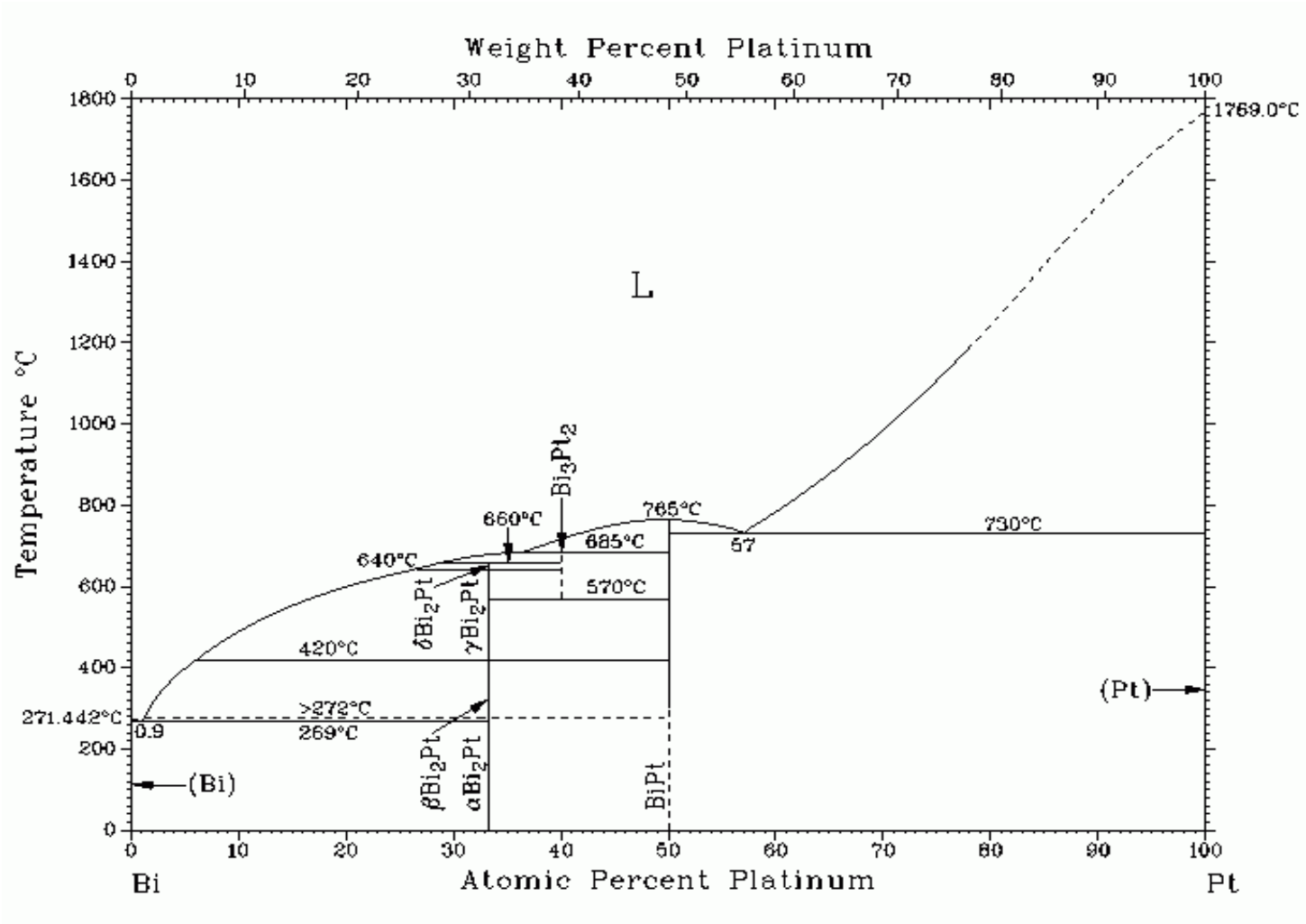


**Figure 18.** Phase diagram of the PtBi system, showing the liquid and solid phases, different compounds and temperatures of formation.[156]

Phase diagrams allow us to visualise the effect of a variable, here it is temperature, on a binary alloy system with varying atomic percentages of Ta. Various phases are observed due to the immiscibility of the two metals in each other, since Pt has a ccp crystal structure whilst Bi has a rhombohedral structure. Nine phases are present, according to Okamoto;[156] these include the liquidus (region labelled 'L'), terminal solid solution of Bi on the far left hand side, $Bi_2Pt$ which consists of four polymorphic forms indicated by α, β,δ and ϒ, $Bi_3Pt_2$ between approximately 32 - 48 % Pt, PtBi and the terminal solid solution on Pt on the far right hand side.

Both PtBi[157,158] and PtPb[159,160] alloys and intermetallics[161,162,163] have been shown to exhibit very high activities for the formic acid oxidation and as such are promising electrocatalysts for this reaction. Electronic effects from the addition of the other metal are thought to

improve adsorption of formic acid while geometric effects are responsible for reduced poisoning by CO.[157] Figure 19 shows the cyclic voltammograms along with the mass spectrometric cyclic voltammograms (MSCVs) of the formic acid oxidation on polycrystalline intermetallic Pt, PtBi and PtPb electrodes, respectively. The oxidation of formic acid on polycrystalline Pt starts at 0.35 V in the forward scan, with three peaks at 0.7, 0.85 and 1.45 V, respectively, corresponding to oxidation reactions. In the reverse scan, an oxidative peak at approximately 0.7 V is observed, which is larger than the corresponding peak in the forward scan due to poisoning of the Pt by CO. From the two alloys, it can be seen that PtPb has both a lower onset potential and achieves a higher current compared to the PtBi electrode.[136]

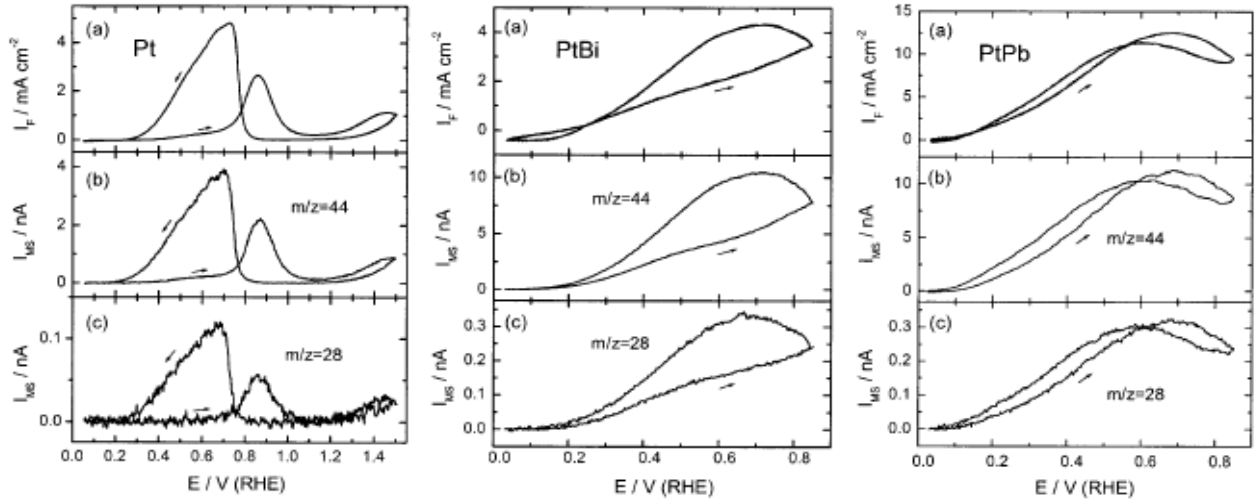


**Figure 19.** Formic acid oxidation on Pt, Pt/Bi and Pt/Pb electrodes in 0.1 M HCOOH and 0.1 M $H_2SO_4$ at a scan rate of 10 mV/s.[136]

The state of the art catalyst for the formic acid oxidation is an ordered mesoporous carbon (OMC) PtBi catalyst prepared by Li et al.,[163] in which the nanocrystallites were embedded within the OMC structure. This catalyst exhibited very high mass activities of 770 mA/mg as can be seen in Figure 20.

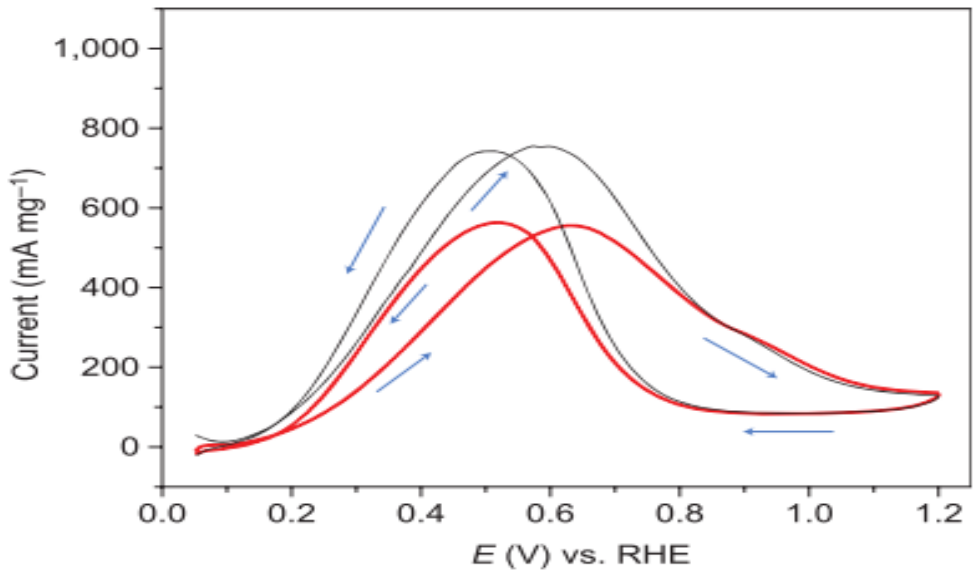


**Figure 20.** Voltammetric profiles of OMC-PtBi- 1 nm (red) and OMC-PtBi-3 nm (black) in 0.5 M sulfuric acid + 0.5 M formic acid at 10 mV/s. [163]

It was noted that the performance of these catalysts almost mirrored that of Pd/C catalysts in the oxidation of formic acid, where use of Pd prevents formation of the catalyst poison. It can be seen that the current curve in both the forward and reverse scans almost match, which contrasts with that of pure Pt. This is indicative that the reaction does not take place via the dehydration path on the OMC-PtBi catalysts. These PtBi catalysts have an onset which is 0.12 V less than the corresponding OMC-Pt catalyst, showing the ease of the formic acid reaction on the alloy catalyst. The OMC-PtBi 3 nm catalyst showed higher activity at lower voltages compared to the corresponding 1 nm catalyst, this higher in performance of the 3 nm catalyst was explained in terms of the higher crystallinity of this catalyst.[163]

The synthesis method for preparation of PtBi nanocrystalline intermetallics reported by Li and co-workers[163] relied on the use of an OMC support. This sulphur-functionalised OMC acted as a metal trap and therefore was a support onto which nucleation of Bi could take place. Despite the reasonable mass activities of these catalysts towards the oxidation of formic acid, their method is inefficient. The catalyst preparation involves multiple steps and is costly in terms of time and energy, with some steps requiring the sample to be heated at high temperatures (up to 600 °C) for long periods of up to 12 hours. Heat treatment also

had to be employed in order to clean the catalysts and remove adsorbed sulphur and hydrogen and also as a means to control particle size along with the use of an OMC support.

A current transient was recorded by Li et al.[164] for their OMC-PtBi-3 nm catalyst as is shown in Figure 21 below. The stability of their catalyst is comparable to the stability of the PtBi catalysts prepared in this work where a decrease in current from approximately 800 to 200 mA/mg was also observed within a similar time frame.

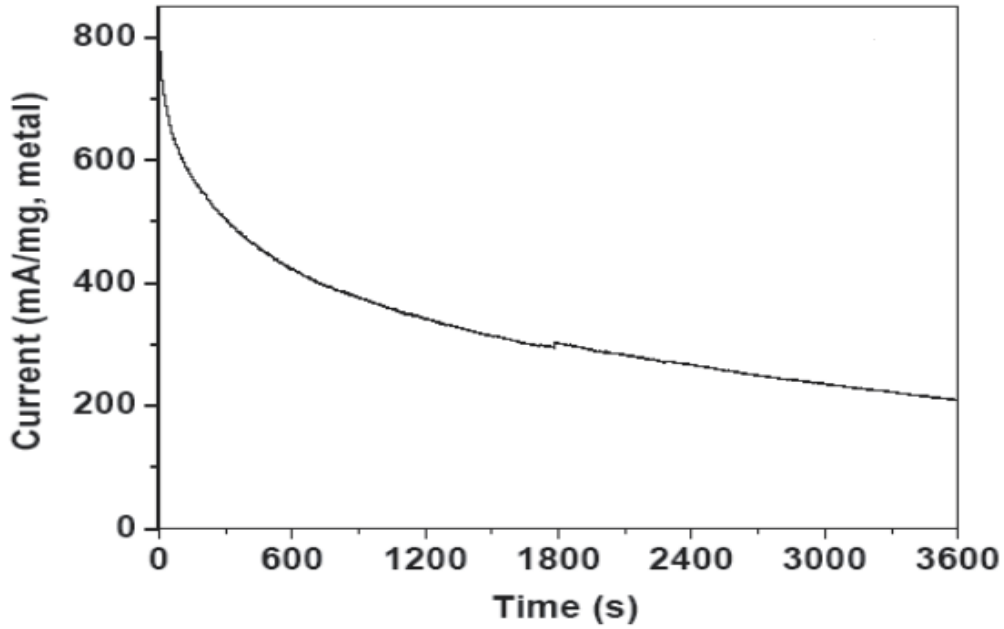


**Figure 21.** Current transient of a OMC-PtBi-3 nm catalyst at 0.3 V vs RHE at 200 RPM.[163]

Maksimuk et al.[165] reported synthesis of PtPb nanorods by a reductive method. *Tert*-butylamine borane (TBAB) was used to reduce the Pt and Pb salts to the corresponding intermetallic structure. The nanorods were on average of the dimensions 45 by 6 nm. On the other hand, Chen et al.[159] prepared a non-intermetallic catalyst by a reduction method which showed over 3 times the activity of a commercial Pd black catalyst and 24 times that of Pt/C for the formic acid oxidation. Their method consisted of two steps, where step one was a co-reduction and step two was a further reduction step after an initial centrifugal separation. This catalyst had a particle size of approximately 4 nm. Figure 22 below shows the current-time transient for their PtPb catalyst compared to the commercial Pd black and

Pt on carbon. This PtPb catalyst can clearly be seen to exhibit a greater stability towards the formic acid oxidation than Pd black and Pt/C.

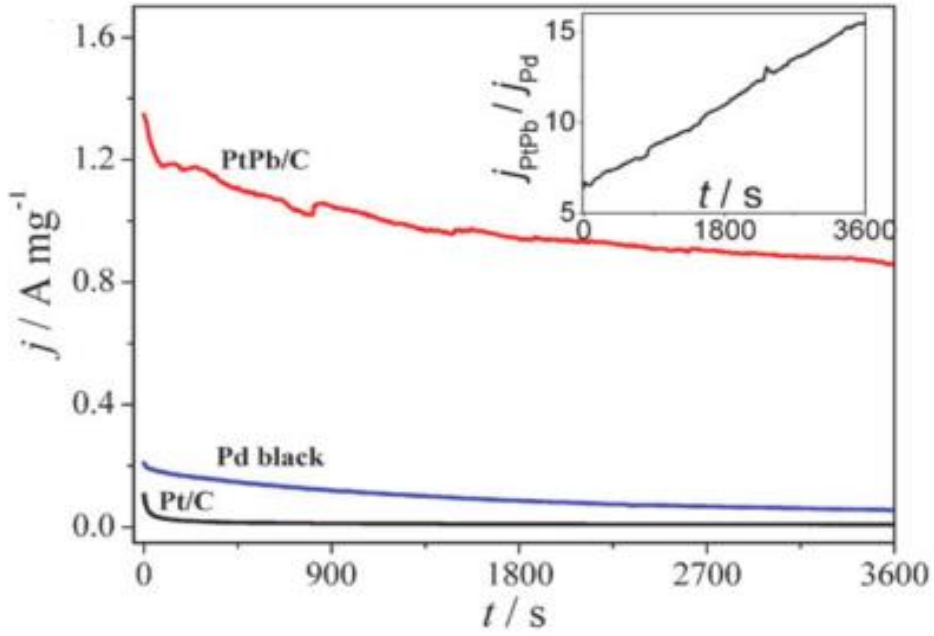


**Figure 22.** Current-time transients of the formic acid oxidation at 0.3 V vs RHE over 1 h in 0.1 M $H_2SO_4$ and 0.5 M HCOOH. The inset shows the current ratio between PtPb/C and Pd black.[159]

## 3.2 Experimental

Synthesis

A mixture of 50:50 calcium chloride (saturated) and MilliQ water (resistivity >18.2 MΩ cm) was used to prepare the catalysts. Clean nanoparticles were prepared following a modified version of the cathodic corrosion method[7] in which a Pt wire (diameter 0.13 mm) was submerged into 10ml of a calcium chloride solution containing either $Bi_2O_3$ (saturated in 0.1 M $HClO_4$) or $PbCO_3$ ($10^{-5}$ M in 0.01 M $HClO_4$) to prepare the PtBi or PtPb nanoparticles, respectively. The wire was rotated at 50 RPM in order to keep the concentration of the alloying metal near the electrode constant. This meant that a homogenous composition of nanoparticles would be more likely to result Various volumes of the alloy metal solution were transferred to the synthesis beaker to form products with different concentrations of the two metals (50, 150, 300, 450 and 750 µl of $Bi_2O_3$ solution and 10, 50 and 100 and 150 µl of $PbCO_3$). An AC, square wave voltage of -10 – 0 V was applied between the platinum

working electrode and the platinum counter electrode. A rotating system was used and rotation set to 50 RPM in order to decrease the amount of bubble formation, thereby preventing drops in conductivity. Following etching of the platinum wire, the resulting suspension was cleaned by centrifuging, decanting and addition of more Milli-Q water until the excess reactants had been removed.

It is of high importance that both the nanoparticles and glassware used for electrochemical experiments were free from any organic contamination. Glassware was cleaned via the method mentioned above and placed in a large beaker, fully immersed in an acidic solution of potassium permanganate and left overnight; this was removed the following day with a 3:1 solution of $H_2O_2$ and $H_2SO_4$ and rinsed with Milli-Q water. This protocol was followed prior to electrochemical experiments in order to ensure clean and reproducible experimental conditions.

Characterisation

X-ray diffraction patterns were collected at an angle range of 20 – 110 ° in 2θ on a Bruker D2 PHASER powder X-ray diffractometer operating at 30 kV and 10 mA and fitted with a Co tube. XRF analyses were run on an S8 TIGER. TEM images were carried out on a JEM-2100. Ethanol suspensions of each catalyst were drop-casted on carbon-coated copper grids and then air-dried to create the resulting samples. XPS was carried out using a Kratos XPS spectrometer with a monochromatic Al Kα source.

Electrochemistry

Suprapur (Merck) reagents and MilliQ water (resistivity >18.2 MΩ cm) were used to prepare solutions and argon gas was bubbled into these before measurements to purge the cell of oxygen. A known amount of nanoparticles was deposited onto a glassy carbon working electrode. An Autolab potentiostat was used, a gold wire was used as a counter electrode and standard hydrogen was employed as the reference. Counter electrodes were flame annealed before use in order to remove traces of organics and all measurements were performed at ambient temperature.

On-Line electrochemical Mass Spectrometry (OLEMS)

Online Electrochemical Mass Spectrometry (OLEMS) was used to detect the gaseous products formed during the reaction. The reaction products at the electrode interface were collected with a small tip positioned close to the electrode. The tip is a 1 mm diameter porous Teflon cylinder (Porex with an average pore size of 5 µm - 1 µm and 45 % - 55 % porosity) in a Kel-F holder. The tip configurations were cleaned overnight in a solution of 2 M NaOH solution (VWR, EMSURE) and rinsed 5 times with MilliQ hot water before use. An SEM voltage of 2100 V was used. The pressure was equilibrated for 1 h prior to each measurement.

## 3.3 Results and discussion

A set of PtBi and PtPb nanoparticles with varying compositions were prepared, as detailed in the experimental section above. The XRD of these two sample sets and the XRF data of the most active catalysts from both sets will be presented and discussed in the following. The XPS, TEM and OLEMS data presented here were collected from previously made samples prepared by other members of the group.

### 3.3.1 Physical characterisation

The following will discuss the XRD, XRF, XPS, TEM and particle size distribution of the PtBi and PtPb catalysts.

Figure 23 below shows the XRD data for the 750 µl and 450 µl PtBi set of catalysts compared to pure Pt, where the legend shows the amount of $Bi_2O_3$ solution added to the synthesis vessel. Other samples were also prepared (not shown here) using 300 µl, 150 µl and 50 µl of the $Bi_2O_3$ solution. The XRD analysis of these samples also showed no shift in peak for the Pt(111) signal.

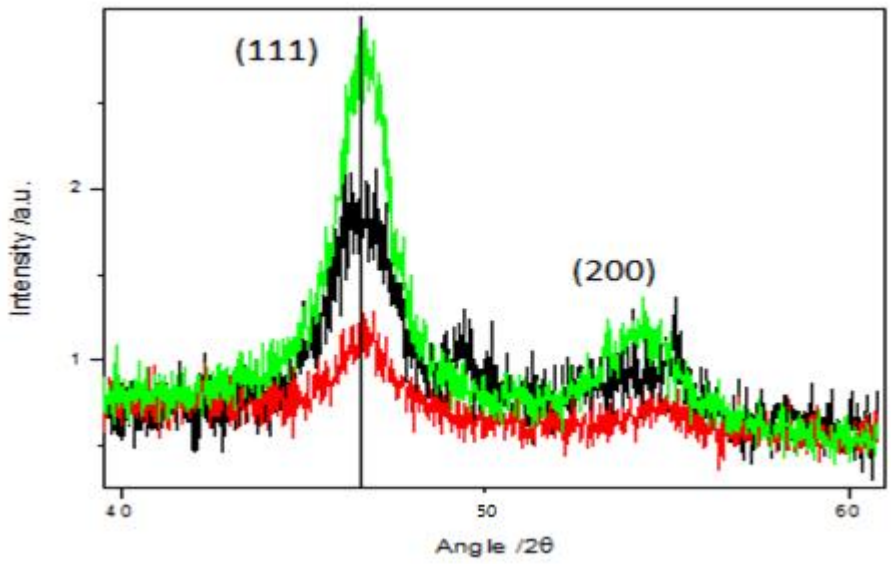


**Figure 23.** XRD diffractogram of the range of PtBi nanoparticles containing differing amounts of $Bi_2O_3$; 450 µl (black), 750 µl (red) and 0 µl (green).

Particle sizes for the PtBi catalysts were obtained from XRD using a derivative of the Scherrer equation via the EVA software on the diffractometer. All nanoparticle samples were 6 nm, compared to 8 nm for pure Pt. This indicates that increasing the concentration of bismuth in the volumes chosen does not affect the particle size, whereas upon alloying Pt with a Bi adatom, a lattice contraction occurs.[166] For the diffractograms of the PtBi nanoparticles, it is observed that the relative intensities of the peaks seem to decrease with increasing amounts of bismuth; this is in agreement with results observed in the literature.[73]

Figure 24 shows the XRD data for the PtPb set of catalysts compared to pure Pt nanoparticles, with the caption showing the amount of Pb added to the reaction vessel.

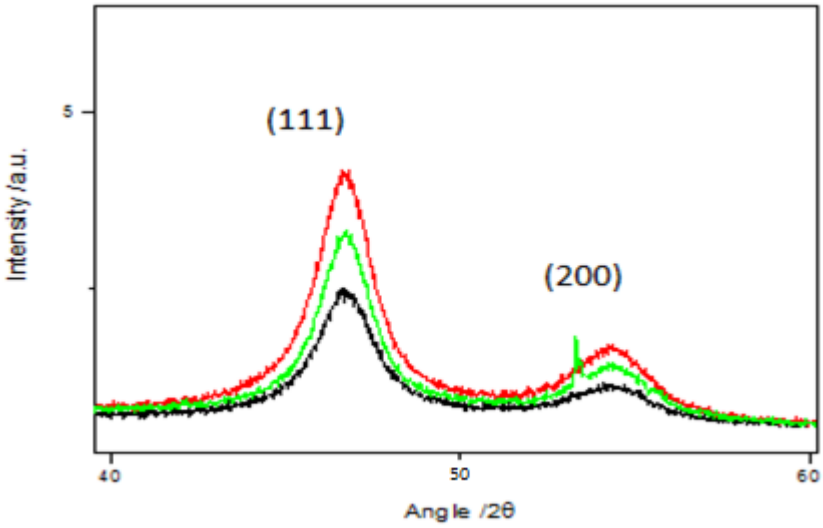


**Figure 24.** XRD diffractogram of the range of PtPb nanoparticles containing differing amounts of $PbCO_3$; 150 µl (black), 50 µl (red) and 0 µl (green).

The particle sizes obtained from XRD for the PtPb nanoparticles were all 6 nm, the same size as the PtBi nanoparticles. This is likely due to the fact that these adatoms are adjacent in the periodic table and that the volumes of alloy metal added in solution were not hugely different.

For both sets of PtBi and PtPb catalysts, no shift was observed of the peak corresponding to Pt(111) (46.6 2Θ in pure Pt, 46.3 in PtBi alloy). As was shown by Vergard's equation in equation 13, a shift in peaks upon alloying should be explained by this law. This would indicate inhomogeneity of the alloy, however, due to the difference in broadness of the peaks, a proper comparison cannot be made to see if there is a clear shift, and therefore it cannot be proven that the alloy is not homogeneous. A very slight shift of around 0.3 2Θ to lower angles of 46.3 would be expected. This is indicative of lattice expansion due to incorporation of Bi atoms during formation of the alloy corresponding to interaction between PtPb and Pt and PtBi and Pt, for example.[160]

**Table 1.** Table to show metals with their associated lattice parameter and crystal system

| **Metal** | **Lattice parameter /$10^{-10}$ m** | **Crystal system** |
|---|---|---|
| Pt | 3.916 | Cubic |
| PtBi[a] | 4.310 | Hexagonal |
| PtPb[b] | 3.926 | Cubic |

[a]Sample created using 400-750 µl of Bi2O3 solution (results were identical for samples in this range)

[b]Sample created using 50-150 µl of Bi2O3 solution (results were identical for samples in this range)

Since X-rays have a wavelength ranging from 0.01 to 10 nm, if we assume the wavelength of the X-ray is 4 nm and use the values for the maximum for pure Pt to calculate the lattice constant using the equation in section we get:

$$a_{fcc} = \frac{\sqrt{2\lambda}}{sin\theta} \quad (30)$$

$$a_{fcc} = \frac{\sqrt{2\ x\ 4}}{\sin\theta} = 3.89 \quad (31)$$

If we compare this value to the value for Pt in Table 1 above, it can be seen that they are very close. These values can be used to prove formation of the alloy due to lattice expansion[119]

X-ray fluroescence analyses were performed on the most active catalyst from both the PtBi and PtPb set, in addition to this, an XRF experiment was carried out for the $Bi_2O_3$ solution used to prepare the PtBi catalysts in order to determine an approximate concentration of Bi in the solution; it was calculated to be $10^{-6}$ M, which is comparable to the conditions used by Kwon et al. in which a Bi saturated solution of around $10^{-5}$ M was used.[74] The formula for the catalyst where 450 µl $Bi_2O_3$ was added, was determined from XRF to be $Pt_{63}Bi_{36}$. The average elemental composition was determined to be 63 % Pt ± 2 and 36 % Bi ± 2 (not shown here).

Below are the XRF and EDX spectra (Figure 25) of the PtBi and PtPb catalysts. The XRF confirms the presence of PtBi and PtPb nanoparticles through peaks at 8.27, 9.45, 11.09,

and 11.25 keV, which relate to Pt. Lines at 10.85, 13.07, and 15.28 keV relate to Bi and those at 10.58 and 12.61 keV are indicative of Pb. The EDX further confirms the presence of these three metals through maxima at 2.05 keV (Pt), 2.41 keV (Bi) and 2.35 keV (Pb).

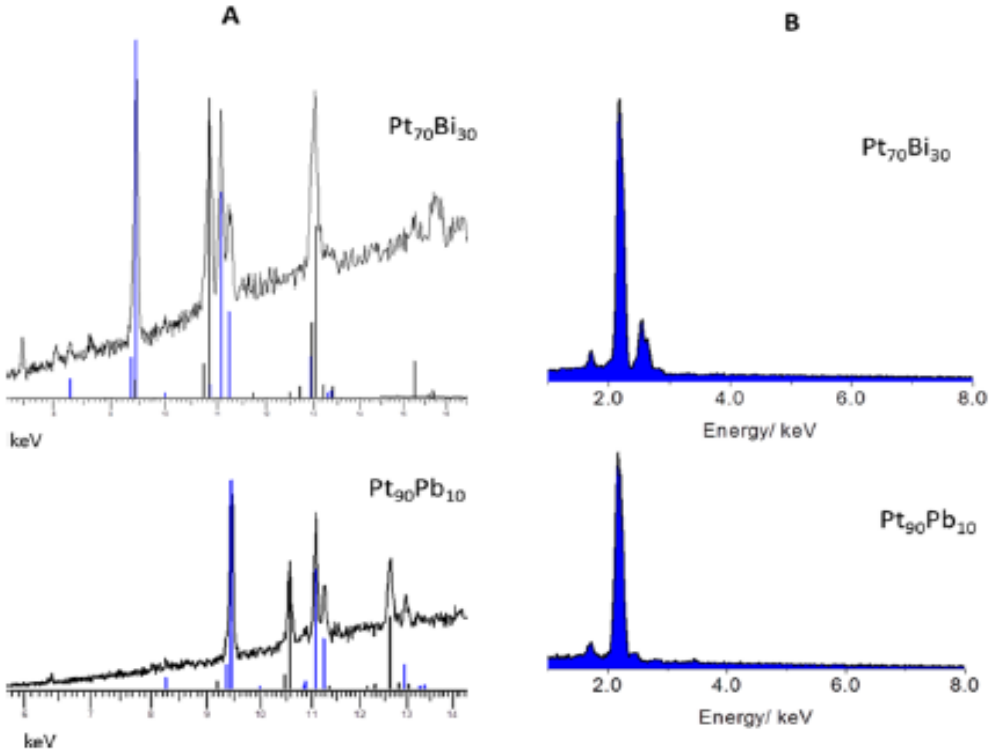


**Figure 25.** XRF (A) and EDX (B) spectra of the $Pt_{90}Pb_{10}$ and $Pt_{70}Bi_{30}$ nanoparticles. In the XRF spectra, blue lines represent Pt whereas black lines represent either Pb or Bi.[100]

The XPS plot in Figure 26 shows characteristic X-rays emitted by the elements Pt, Pb and Bi. Upon comparing the O 1s, Pt 4f, Bi 4f and Pb 4f binding energies of the alloy nanoparticles synthesised in this work to those of the pure elements in the literature, a shift to higher energy is observed, indicative of formation of the alloy. Platinum nanoparticles synthesised under the same conditions as the alloys were analysed by XPS and included in order to make a proper comparison.

Upon observation of the PtBi nanoparticles, bands were observed at 74.18 eV, corresponding to the signal from the Pt $4f_{5/2}$ and 71.35 eV, corresponding to the Pt $4f_{7/2}$ energy level from the PtBi environment. A shift was observed for the band from the Pt $4f_{5/2}$ energy level compared to the pure Pt (74.45 eV) value from the literature.[167] This shift may

be due to interaction with electronegative species, charge displacement from the Pt-Bi bond or presence of a Pt bulk oxide species. The two bands at 159.8 eV (Bi $4f_{3/2}$) and 165.1 eV (Bi $4f_{5/2}$) are indicative of an oxidised form of Bi such as BiO(OH).[168] Additionally, peaks correlated to a Bi-Bi bond are usually expected at 157 and 162 eV, however, here we observed a shift to slightly higher energy (158 and 163 eV), which is thought to be due to displacement of charge.[169]

Moving onto the PtPb nanoparticles, the Pt $4f_{5/2}$ feature was shifted towards a lower energy than pure Pt. Unlike PtBi, there are no surface platinum oxide species present in the PtPb sample. Features at 137.5 eV and 142.2 eV are correlated to the Pt-Pb bonding environment, whereas features at 138.9 eV and 143.5 eV are ascribed to oxidised Pb species. From the relative intensities, it is clear that much of the Pb near to the surface of the material is in the oxidised form. The oxygen binding energy is different in the PtPb sample compared to PtBi. While Bi forms oxides, Pb additionally forms these along with hydroxides ($Pb(OH)_2$) and carbonates ($PbCO_3$) when exposed to air.[170] Formation of Pb oxides is more feasible compared to formation of Pt oxides; this explains the lack of Pt oxides on the PtPb material. Since XPS is a form of thin layer analysis, it tells us about surface composition and therefore whether segregation of a certain element to the surface of an alloy has occurred. In our case, it showed that the surface of the nanoparticles were prone to oxidation and suggested that the Pb had segregated to the surface, since more of this was observed than Pt.

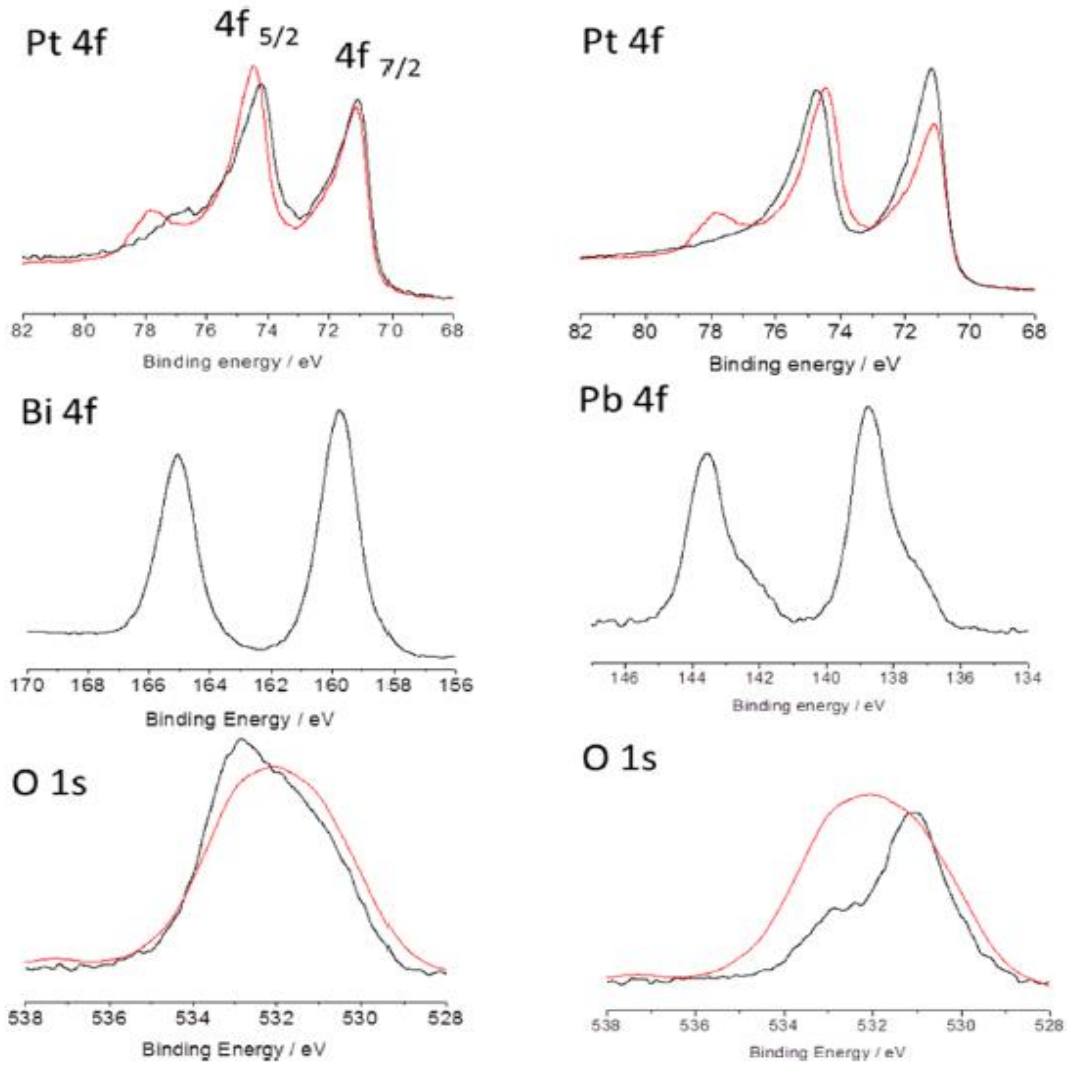


**Figure 26.** XPS spectra of A) $Pt_{70}Bi_{30}$ and B) $Pt_{90}Pb_{10}$ nanoparticles.

Figure 27 presents TEM images and particle size distributions of the $Pt_{70}Bi_{30}$ and $Pt_{90}Pb_{10}$ nanoparticles compared to pure Pt nanoparticles. These images show the homogeneous particle size distribution of the alloy nanoparticles. On counting over a thousand particles, the average particle size of the $Pt_{70}Bi_{30}$ alloy was found to be 5.3 nm ± 1.2, whereas the diameter of the $Pt_{90}Pb_{10}$ particles were found to be slightly smaller, 4.2 nm ± 0.7.

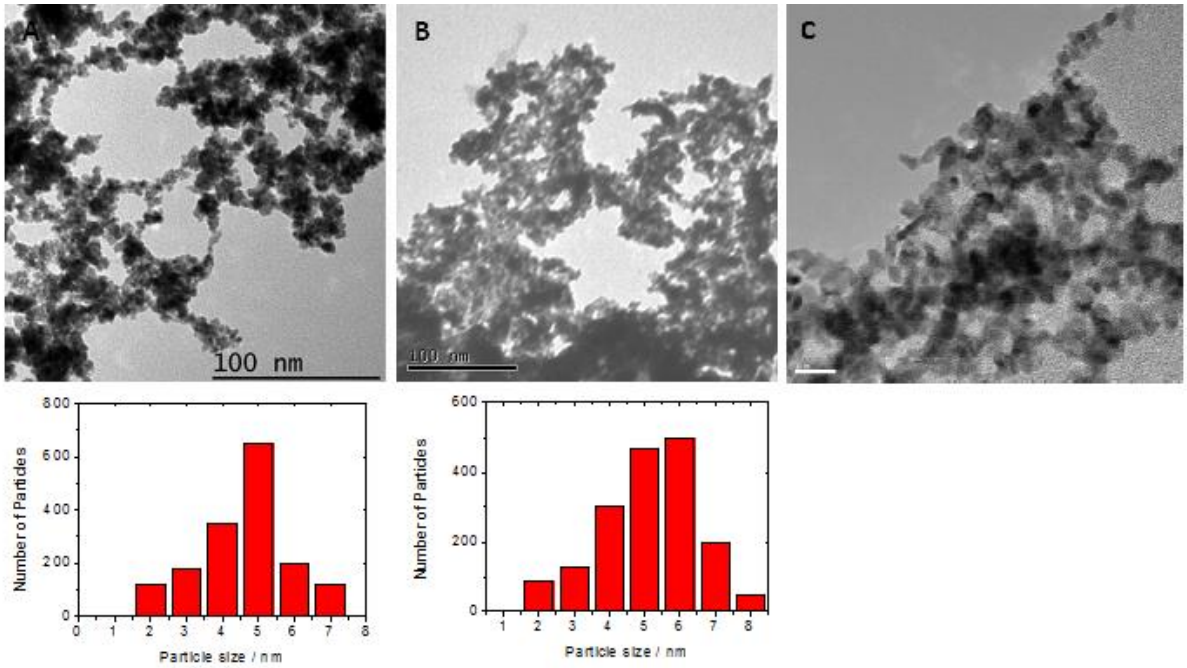


**Figure 27.** TEM images and particle size distribution of A) $Pt_{80}Pb_{20}$ nanoparticles B) $Pt_{70}Bi_{30}$ nanoparticles and C) Pt nanoparticles.

## 3.3.2 Electrochemical characterisation

Following physical characterisation to determine composition, particle size, shape and homogeneity, particles were analysed electrochemically by voltammetry, OLEMS and chronoamperometry with a focus on catalytic activity and durability.

Electrochemical blanks were performed for all catalysts. In addition to providing an initial characterisation, the voltammograms ran in $H_2SO_4$ for the PtPb and PtBi catalysts served to remove the excess of Bi and Pb surrounding the alloy nanoparticle. This excess of metal atoms hinders catalytic activity by blocking active sites.[74,171] The blank voltammograms further illustrated proper alloying within the nanoparticles. The blank of pure platinum nanoparticles displays peaks at approximately 0.12 V and 0.27 V which correspond to hydrogen adsorption on (110) and (100) sites, respectively.[172] The voltammetric profiles of the binary alloy catalysts are in good agreement with previous results obtained for PtBi[173] and PtPb[160] alloys under similar conditions along with the compositional data obtained from XRF, XPS and EDX. The blanks provide confirmation of formation of the alloy as they lack the characteristic features of pure platinum and have gained extra redox behaviour due to the oxidation (0.9 V) and reduction (0.8 V) of Bi atoms.[174] It is known that alloys behave

differently to single crystal electrodes[175] as is evidenced by the differences in the hydrogen adsorption/desorption region on the electrochemical blanks, in addition to variations in the oxidation curves. A blank voltammogram of PtBi nanoparticles in 0.5 M $H_2SO_4$ is shown in Figure 28 below.

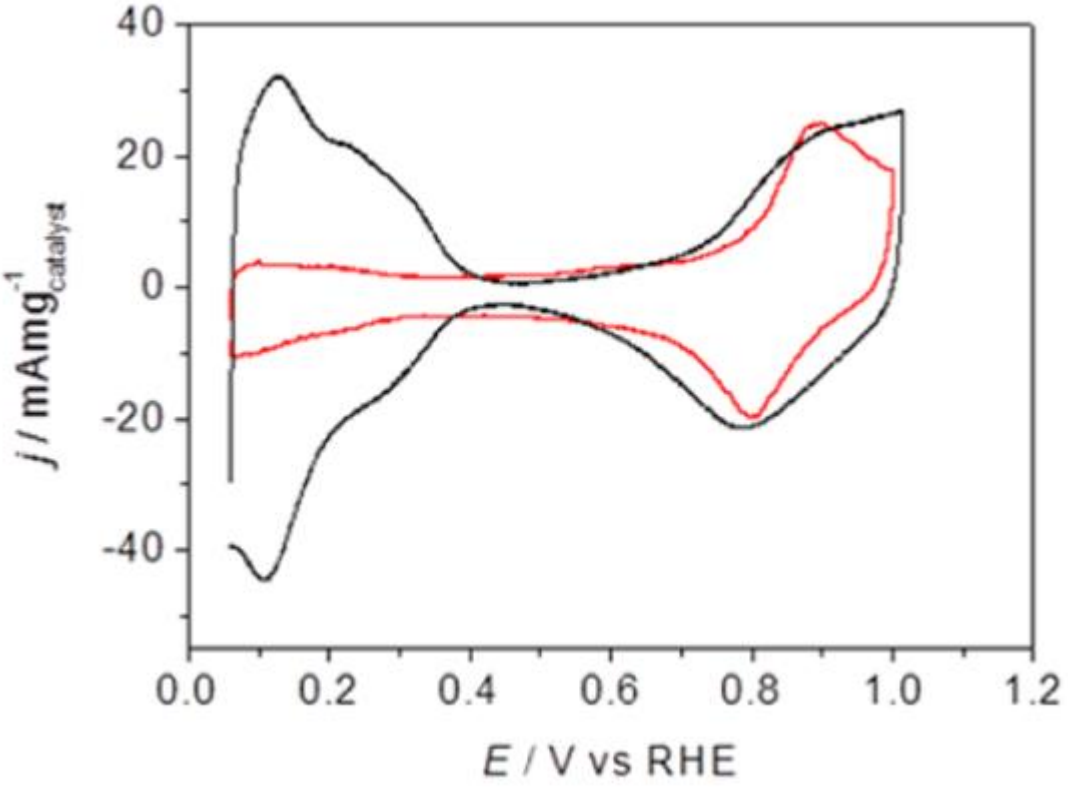


**Figure 28.** Voltammetric profile of $Pt_{70}Bi_{30}$ nanoparticles (red) compared to Pt nanoparticles (black) in 0.5 M $H_2SO_4$ at 50 mV/s.

The 'blank' cyclic voltammogram above (Figure 28) is in good agreement with those observed for PtBi alloys in the literature under similar conditions.[157] After several cycles, the excess of bismuth (which appeared as a peak around 0.25 V) was removed. In the above voltammogram, bismuth oxide formation and reduction is observed in the anodic and cathodic peaks at approximately 0.9 V and 0.8 V, respectively. On comparison with pure Pt, it can be seen that addition of Bi suppresses the hydrogen adsorption/desorption peaks that occur on Pt at early potentials, in addition to this, the surface of the PtBi catalyst is oxidised at later potentials than that for Pt catalysts.[157]

Since the PtPb alloy has a very high percentage of platinum, the characteristic features of this metal can be clearly seen in the blank between 0.12 and 0.27 V (see Figure 29), this

corresponds to hydrogen adsorption/desorption on Pt(110) and (100) sites, respectively. This region is however smaller than it would be for pure Pt nanoparticles and a feature of the PtPb alloy is the onset of surface oxidation which appears to start at approximately 0.75 V.

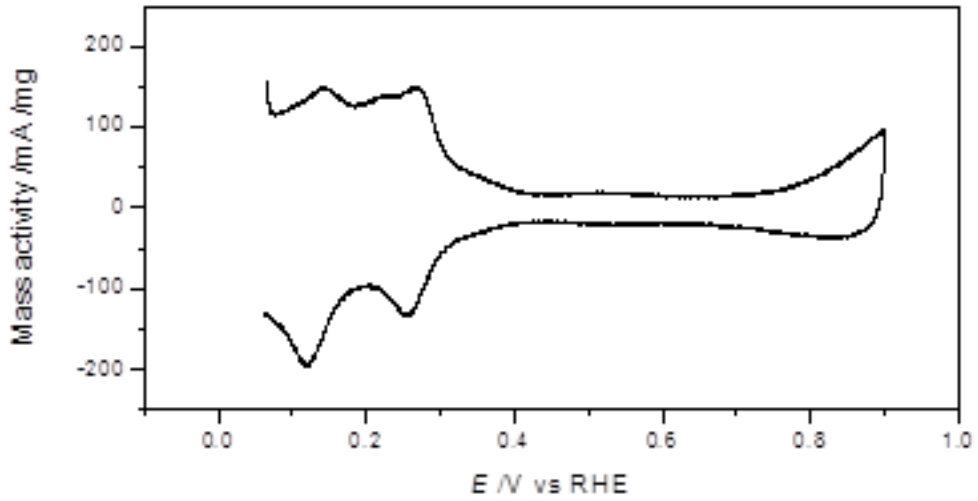


**Figure 29.** Voltammetric profile of $Pt_{96}Pb_3$ nanoparticles in 0.5 M $H_2SO_4$ at 50 mV/s.

Study of the electro-oxidation of formic acid is beneficial to help deepen understanding of electrocatalytic processes in methanol fuel cells, in which formic acid is present as an intermediate. Previous studies on the formic acid oxidation have shown that the PtBi alloy generally shows higher activity,[164] whereas the PtPb alloy exhibits better durability.[160] The highest mass activity for the oxidation of formic acid was reported by the group of Linda Nazar at 770 mA/mg,[164] (Figure 20).

The activity of two concentrations of the PtBi and PtPb nanoparticles are shown in Figure 30 below in the formic acid electro-oxidation and compared to pure Pt, along with the ion current traces for m/z 44 ($CO_2$). The onset for the PtBi nanoparticles is around 0.2 V and the mass activity is two orders of magnitude higher than that of pure Pt. On the other hand, the onset of the formic acid oxidation on PtPb occurs slightly later at 0.3 V, but shows similar mass activity to the PtBi alloy. The onset and decay of these oxidation curves can be correlated with the OLEMS. With the PtBi alloy, the catalyst with the lower concentration of bismuth exhibited higher catalytic activity, in contrast with the oxidation results for the PtPb

catalyst in which the nanoparticles containing the higher amount of Pb displayed higher currents. In order to detect products from the electrocatalytic oxidation of formic acid, we performed OLEMS experiments. Detection of $CO_2$ and the correlation of the oxidation curve with the ion current for this molecule suggest that our catalysts facilitate the direct pathway which goes via the dehydrogenation route; this coincides with the maximum between 0.8 and 1.0 V which is likely related to oxidation of formic acid via the direct route to form carbon dioxide.

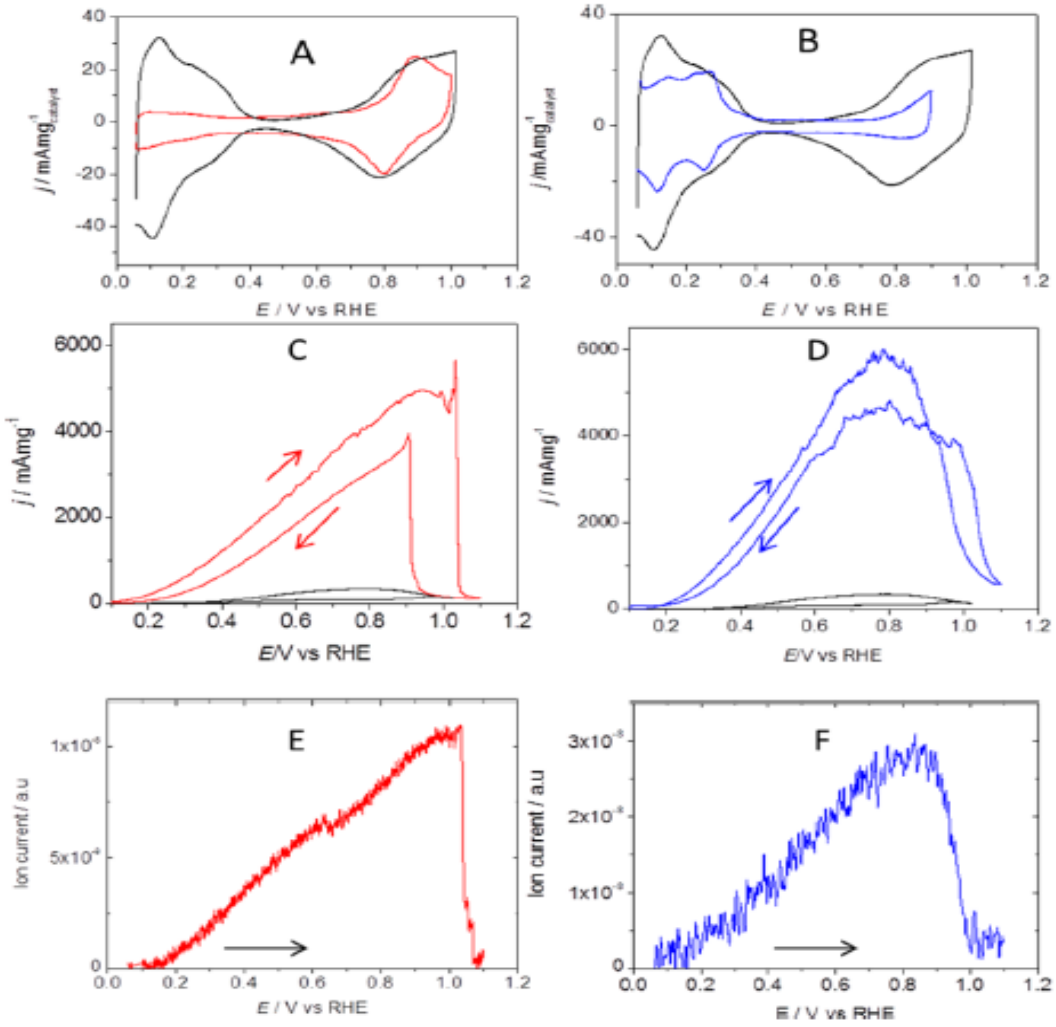


**Figure 30.** Voltammetric profiles of $Pt_{70}Bi_{30}$ and $Pt_{90}Pb_{10}$ nanoparticles in (A and B) 0.5 M $H_2SO_4$ at a scan rate of 50 mV/s and (C and D) 0.5 M $H_2SO_4$ and 1M HCOOH at a scan rate of 10 mV/s. (E and F) OLEMS in 0.5 M $H_2SO_4$ at 10 mV/s and ion/mas current of 44 ($CO_2$).

The onset potentials observed in this work were comparable to the lowest achieved by Lopez-Cudero et al.[175] at their highest Bi coverage (0.2 V) on their modified platinum (110)

single crystal electrodes, which were higher than those obtained by Macia´et al.[154] for their bismuth-modified platinum (111) electrodes (0.3 V).

Durability and stability are additional important factors for fuel cell catalyst evaluation. Chronoamperometric measurements were performed at an operating voltage of 0.3 V (versus RHE) in order to investigate the current stability over time, see Figure 31. The PtBi nanoparticles exhibit a high mass activity of 600 mA/mg whereas the PtPb nanoparticles have a lower activity of 400 mA/mg, yet show higher stability towards the formic acid oxidation at low potentials compared to PtBi which exhibits a much higher current decay.

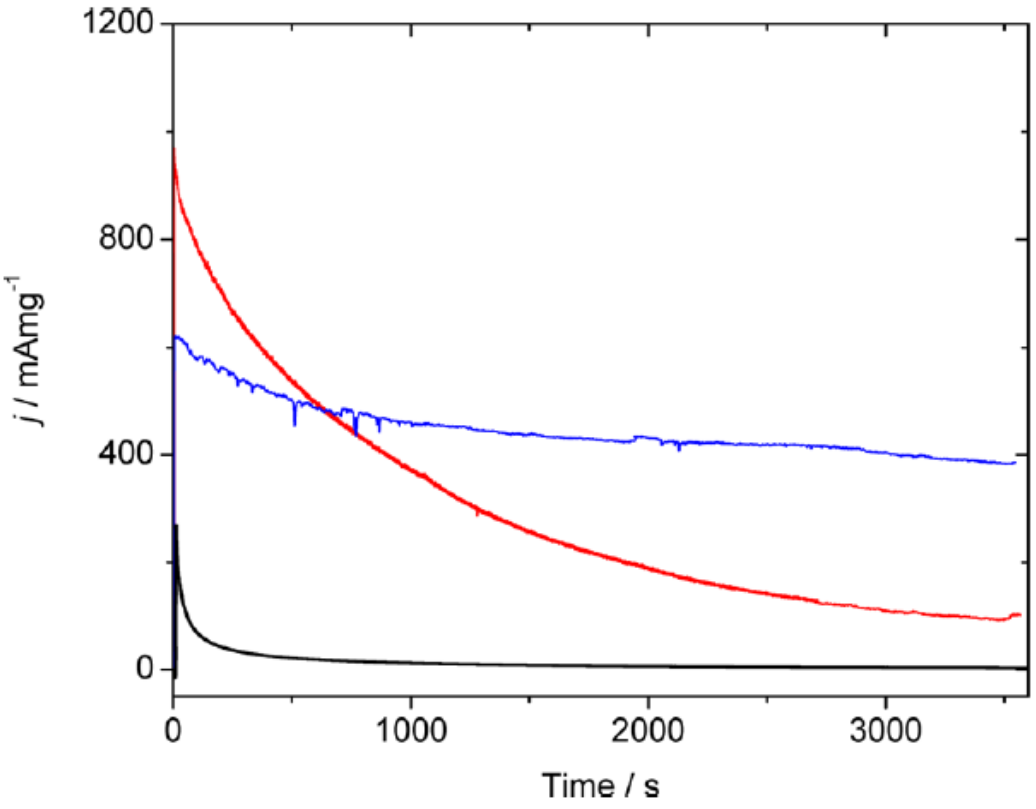


**Figure 31.** Current transients of PtPb (blue) PtBi (red) and Pt (black) nanoparticles at 0.3 V in 0.5 M $H_2SO_4$ and 1 M HCOOH at a scan rate of 10 mV/s.

## 3.4 Conclusion

In this chapter, binary PtBi and PtPb nanoparticles were synthesised via the cathodic corrosion method. Metal composition was confirmed by EDX, XPS and XRF and TEM showed homogeneous dispersion. These catalysts exhibited extraordinary activity in the formic acid

oxidation. Factors including durability, onset potential, activities, and products formed relating back to the mechanism including reasoning for elevated activity will all be discussed in this section.

Our catalysts exhibit extraordinary current densities two orders of magnitude greater than those observed for pure Pt. For $Pt_{70}Bi_{30}$ and $Pt_{90}Pb_{10}$, activities of 630 mA/mg and 800 mA/mg were achieved respectively; these results are improved on those obtained for the state of the art catalysts.[164] The $Pt_{70}Bi_{30}$ catalyst displayed the lowest onset potential for the formic acid oxidation, at 0.1 V, compared to an onset of 0.2 V for the $Pt_{90}Pb_{10}$ catalyst. This is significantly improved from the onset potential of pure Pt on which formic acid oxidation takes place at 0.4 V vs RHE.

Online electrochemical mass spectrometry was employed to detect the products formed from the formic acid oxidation on our catalysts. Carbon dioxide formation was confirmed by following the signal for m/z 44 on the spectrometer. It can be seen in Figure 29 how the onset of $CO_2$ formation correlates with the onset on the voltammogram. The lack of hysteresis between the forward and backward scan upon cycling in the range 0.06 - 1.00 V is indicative of the mechanism proceeding via the direct pathway. This agrees with the results from the OLEMS. Stability is an important factor when assessing catalysts for use in fuel cells. Chronoamperometry was used to evaluate their performance. As was mentioned above in Section, $Pt_{90}Pb_{10}$ showed both higher activity in the formic acid oxidation and stability for currents recorded at 0.3 V over the course of 50 minutes.

As mentioned in detail in Chapter One and earlier in this chapter, the direct pathway consists of direct conversion of HCOOH to $CO_2$ via the active intermediate. Hence, our catalysts avoid the conversion of HCOOH into adsorbed CO due to electronic effects. In summary, the elevated activity of our catalysts in comparison to previous systems can be attributed to the composition of the metal alloy, the reduced particle size (5.3 ± 1.2 nm for PtBi and 4.2 ± 0.7 nm for the $Pt_{90}Pb_{10}$ catalyst) and quite importantly, the level of cleanliness of the catalyst.

# Chapter 4

# $Pt_{90}Rh_5Pd_5$ nanoparticles as catalysts for glycerol oxidation

## 4.1 Introduction

### 4.1.1 Discussion of the glycerol electro-oxidation mechanism

The oxidation of glycerol is able to proceed under ambient conditions using catalysts and produces many fine chemicals, as is shown in Figure 32 below.

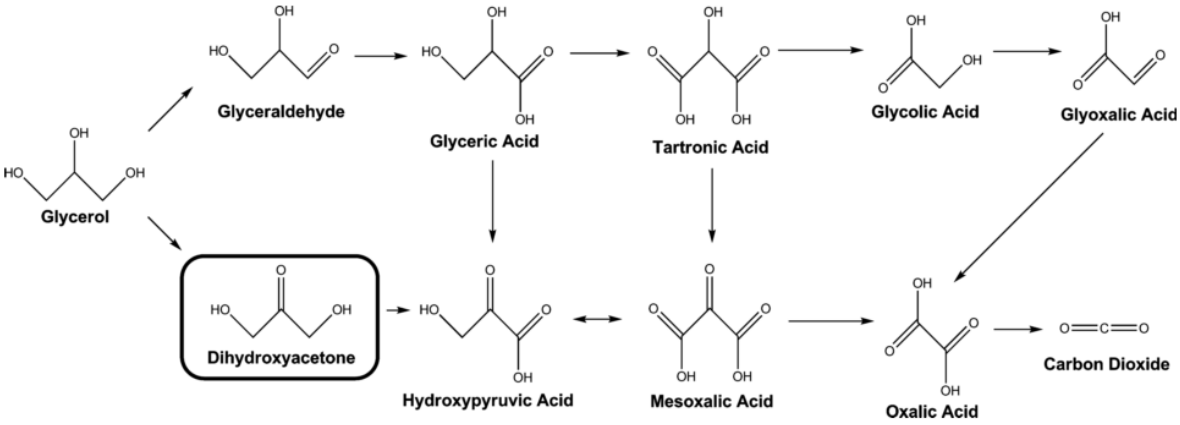


**Figure 32.** The range of fine chemicals that can be produced from the glycerol oxidation.[50]

Glyceric acid and dihydroxyacetone (DHA) are often the major products. DHA is the product with the most commercial applications; it is as an intermediate in synthesis and has applications in nutrition where, when combined with pyruvate, it is a supplement that helps to promote lean muscle growth and in the cosmetics industry as a safer tanning alternative to sunbeds.[176] A complex reaction pathway exists, since glycerol is a highly functionalised molecule. Many catalysts and reaction conditions have been tried for the various routes, generally, under acidic conditions, hydroxypyruvic acid and DHA are formed whereas under alkaline conditions, glyceric acid is formed.[177]

For example, Fordham et al.[178] reported conversion of mesoxalic acid from tartronic acid in 65 % yield and 80 % conversion using a PtBi catalyst, temperature of 60 °C and pH 5.[178] Kimura et al.[53] also found success using a PtBi catalyst, where DHA was formed from glycerol with 80 % selectivity compared to just 10 % using pure Pt. This reaction was done in acid media (pH 2-4).[53]

Bearing in mind that the large field of electrocatalysis concerns the area of organic electrosynthesis, in which topics of focus are to understand reaction mechanisms and determine kinetic laws, there are surprisingly few investigations into the mechanism of the glycerol electro-oxidation. The main current challenge in this reaction is production of partial oxidation products arising from the difficulty in cleaving the C-C-C bond. Koper and Kwon[179] studied the reaction on Pt and Au electrodes comparatively, since in alkali, the reaction can take place on both metals whereas in acidic media, only Pt is active for this reaction. Roquet et al.[180] studied the kinetics and mechanism of the glycerol oxidation on Pt in acid and alkali media. They proposed two possible reaction pathways proceeding oxidation of the glycerol to form glyceraldehyde in both acid and alkali media. The first suggested pathway, also thought to be the main one, involves oxidation of glycerol to glyceraldehyde by the following reaction:

$$C_3H_8O_3 \rightarrow C_3H_6O_3 + 2H^+ + 2e \qquad (30)$$

On the other hand, an alternative possible route involves interaction of adsorbed glycerol with an adsorbed hydroxyl to form glyceric acid. In alkaline media, Roquet et al.[180] found glyceraldehyde to be the main reaction product in contrast with the findings from the Koper[179] group who did not observe this species and thought it to be due to the instability of aldehydes in alkali solution.

Gomes and Tremiliosi-Filho[181] studied the oxidation of glycerol on Pt and Au electrodes in both acid and alkaline media and determined products and intermediates formed by use of FTIR spectroscopy. The glycerol oxidation on Pt is known to be independent of pH, forming glycolic, glyoxylic, formic, tartronic acid and carbon dioxide in both media whereas with Au

the pH affects which products are formed.[181] They found that both metals were more active in alkali than acidic media with Au being the more active metal.

Very recently, Zhu et al.[182] reported the use of PtRhPd nanotruncated octahedrons (NTOs) and nanocubes (NCs) prepared by a hydrothermal method in the oxidation of ethanol to carbon dioxide. Despite being a one-pot method, their synthesis of the PtRhPd NCs involves use of many reagents of which include PVP and organics and a high temperature of 180 C for 4 h. The preparation of the NTOs is similar and with an elevated reaction time of 12 h. An additional cleaning step was necessary to remove the PVP capping agent; this was done by the use of ozone generated by a mercury lamp. Average particle sizes were obtained from TEM and reported to be 12 nm for the PtRhPd nanocubes (NC)s. Chronoamperometric experiments were conducted and it was observed that PtPd lost much more of its initial activity (~40 %) than the PtPd catalyst (15 %). They proposed that addition of Pd imparted stability along with increased activity towards the PtRh catalysts. The reason for the improved stability is thought to be due to the weakened interaction of Rh with C upon alloying with Pd.[183] The strong interaction of Rh with C can deactivate Rh catalysts, therefore alloying with Pt and Pd facilitates removal of C compounds.

Grace and Pandian[184] reported PtPd nanoparticles supported on a polyaniline support and ITO glass as an efficient electrocatalyst for the oxidation of glycerol whereas Marilia et al.[185] observed low onsets and good stability for their $Pt_3Rh$ catalysts relative to pure Pt for this same reaction. These PtRh nanoparticles were between 4 and 7 nm in size. The state of the art catalyst for this reaction is the PdBi catalyst prepared by Zalineeva et al.[186] Despite their large surface areas and very high activities as illustrated in Figure 34, their preparation involves several steps, one such step involving a reduction under hydrogen gas which is performed at a temperature of 300 °C for 2 hours. Their method produces catalysts with a particle size of 5 nm, comparable to those in this work which were 4 nm.

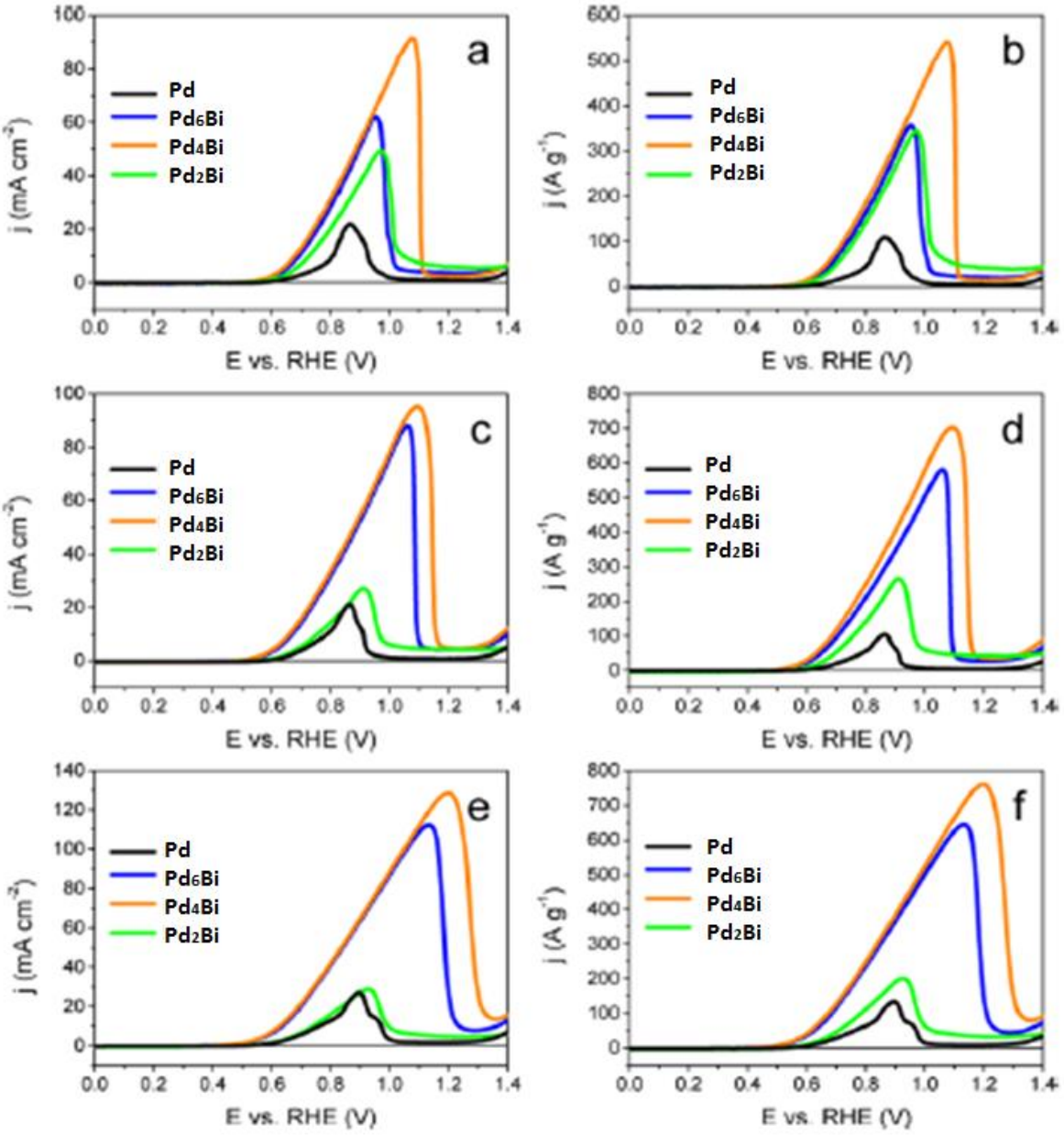


**Figure 33.** Polarisation curves of the glycerol electro-oxidation on PdBi catalysts in 0.1 M glycerol and 1 M KOH at a-b) 5 mV/s, c-d) 20 mV/s e-f) 100 mV/s. PdBi catalysts shown include $Pd_2Bi$ (green), $Pd_4Bi$ (orange), $Pd_6Bi$ (blue) and Pd (black).[186]

A mixture of products, predominantly glyceraldehyde is obtained from the oxidation of glycerol on Pt in acid media. On the other hand, addition of bismuth was found to give high selectivity towards DHA.[50] Nanostructured PdBi catalysts prepared by the sacrificial support method are the state of the art catalysts for this reaction, with the optimal Bi to Pd ratio being 1 to 4 (see Figure 33).[186] It was proposed by these authors that the improved adsorption of OH at sites adjacent to Bi was the reason for the enhanced activity observed

with this catalyst. The $BiPd_4$ catalyst was observed to be selective for DHA and glyceraldehyde from the corresponding peaks in the in-situ FTIR spectra at 1335 and 1070$cm^{-1}$, respectively (see Figure 34 below).

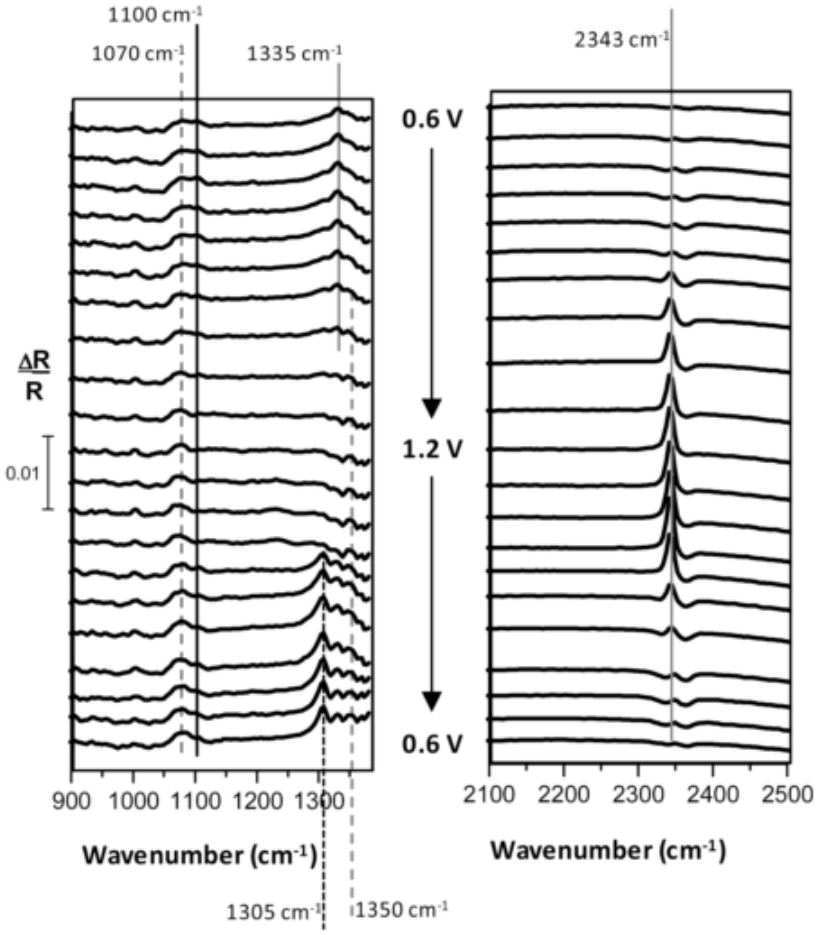


**Figure 34.** In-situ FTIR spectra of the oxidation of glycerol on a self-supported $Pd_4Bi$ catalyst at a potential range of 0.6 V to 1.2 V (RHE) and to 0.6 V in 1 M KOH + 0.1 M glycerol solution at 10 mV/s. Figure taken from Zalineeva et al.[186]

To summarise this section, more research needs to be conducted on this reaction, in particularly to identify adsorbed intermediates and products and determine mechanisms. To fully understand the mechanism, it's necessary to relate the species formed with the geometry and electronic properties of the metal catalyst, concentration of fuel and electrolyte used. With this knowledge, more active, selective and poison tolerant catalysts can be designed for the glycerol electro-oxidation for direct alcohol fuel cell applications. There have been a few reports in the literature of this alloy being used for the ammonia oxidation,[79,187] a stage in the production of nitric acid which is used in making plastics,

whereas its binary counterparts PtRh[7] and PtPd[188] have been reported as being employed in the nitrate reduction[7] and oxidation of alcohols,[189] in particular ethanol and glycerol.[188,184] The Pt component of the catalyst facilitates bond cleavage, whereas Rh and Pd are known to aid stability and improve yield.[187] There have however been no reports of the ternary PtRhPd alloy used for the ethanol and glycerol oxidation reactions to date.

## 4.2 Experimental

Synthesis and Characterisation

A $Pt_{90}Rh_5Pd_5$ gauze was separated into individual wires, one of these wires was submerged into 10 ml of a 10 M NaOH solution. AC, square wave voltages of -5.5 – +0.5 V, -7.5 - +0.5 V and -10 – 0 V were applied between the $Pt_{90}Rh_5Pd_5$ working electrode and the platinum counter electrode to produce different samples. A non-rotating cathodic corrosion setup with a micrometric screw was used and the nanoparticles were cleaned in the same way detailed previously. X-ray diffraction, XRF and electrochemistry experiments were performed as mentioned previously, EDX spectra were performed on a JEOL 2100 SEM.

## 4.3 Results and discussion

$Pt_{90}Rh_5Pd_5$ nanoparticles were prepared by cathodic corrosion, as detailed in the experimental section above. The XRD, XRF, SEM and EDX data obtained for this alloy will be presented and discussed in the following along with the blank voltammograms and activity towards the electro-oxidation of glycerol.

### 4.3.1 Physical characterisation

The following will discuss the XRD, XRF, SEM and EDX results of the $Pt_{90}Rh_5Pd_5$ catalyst, with focus on particle size, composition and homogeneity.

Figure 35 below shows the XRD diffractogram for the $Pt_{90}Rh_5Pd_5$ nanoparticles, with the reflections for the appropriate Pt, Rh and Pd reflections labelled in the legend. An average particle size of 4 nm was estimated from the peak widths via the EVA software. The small bump around 69 2 θ is assigned to the crystal, as this was present was a ‘blank’ of the crystal

containing no sample was performed. This is significantly smaller than the 12 nm reported as the average particle size for the PtRhPd NCs prepared by Zhu et al.[182]

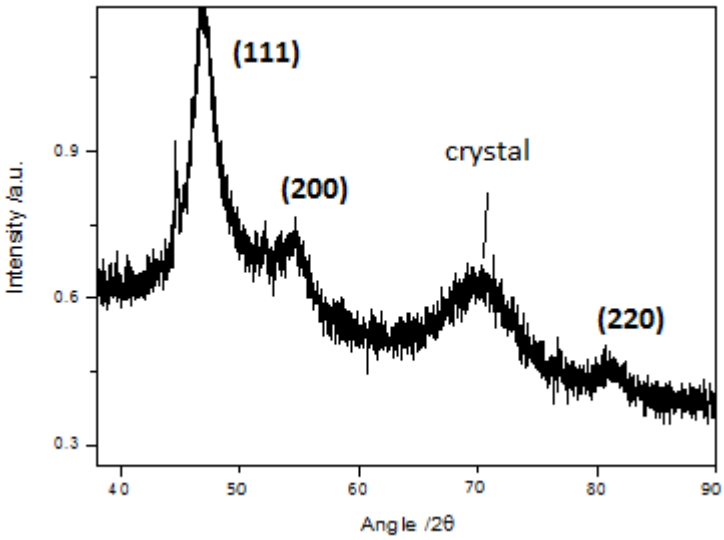


**Figure 35.** XRD diffractogram of $Pt_{90}Rh_5Pd_5$ nanoparticles prepared at a voltage of ±5 V and an offset of -5 V.

An estimated particle size of 4 nm was determined using the EVA software for the samples in Figure 42. This is the same particle size as that obtained for the sample prepared between -10 and 0 V in Figure 35. It can therefore be concluded that for this alloy, in 10 M NaOH, changing between these voltages does not affect particle size significantly. The bump around 70 2θ is attributed to the crystal and was confirmed by running a 'blank' diffractogram of the crystal containing no sample.

**Table 2.** Table to show metals and their respective lattice parameters.

| **Metal** | **Lattice parameter /$10^{-10}$ m** |
|---|---|
| Pt | 3.916 |
| PhRhPd[a] | 3.886 |
| PhRhPd[b] | 3.886 |

[a]Sample created using conditions of ±5 V offset -5 V

[b]Sample created using conditions of ±3 V offset -2.5 V

All three metals in Table 2 showed cubic crystal systems, for this reason, it is not mentioned within the table itself.

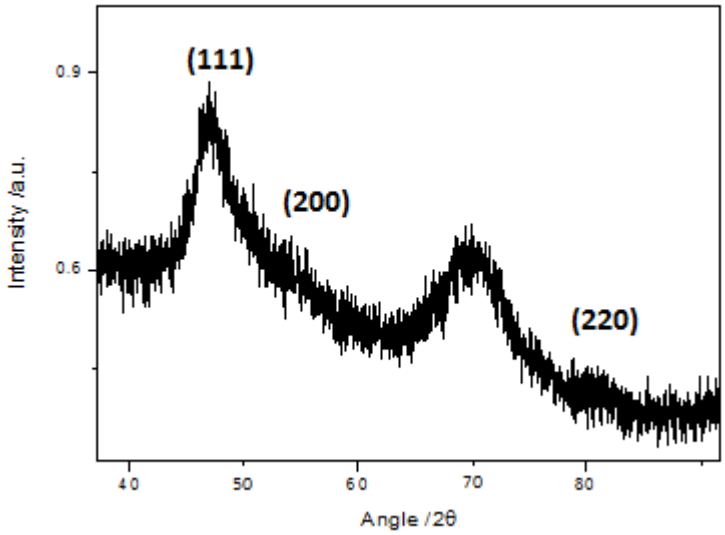


**Figure 36.** XRD diffractogram of $Pt_{90}Rh_5Pd_5$ nanoparticles prepared at a voltage of ±3.5 V and an offset of -2.5 V.

An XRF spectrum was measured (Figure 37) in order to observe whether the PtRhPd nanoparticles retained the same composition as the $Pt_{90}Rh_5Pd_5$ alloy. The percentage of Pt was confirmed to be 90 %, however the XRF was unable to quantify the percentages of Rh and Pd due to a small amount of sample and the low quantities of these elements present. EDX was performed on this sample (Figure 38) to accurately determine the composition of Rh and Pd. Images were obtained from the SEM, since the detection limit of the microscope is ~20-30nm. The images showed a homogeneous sample in terms of particle dispersion.

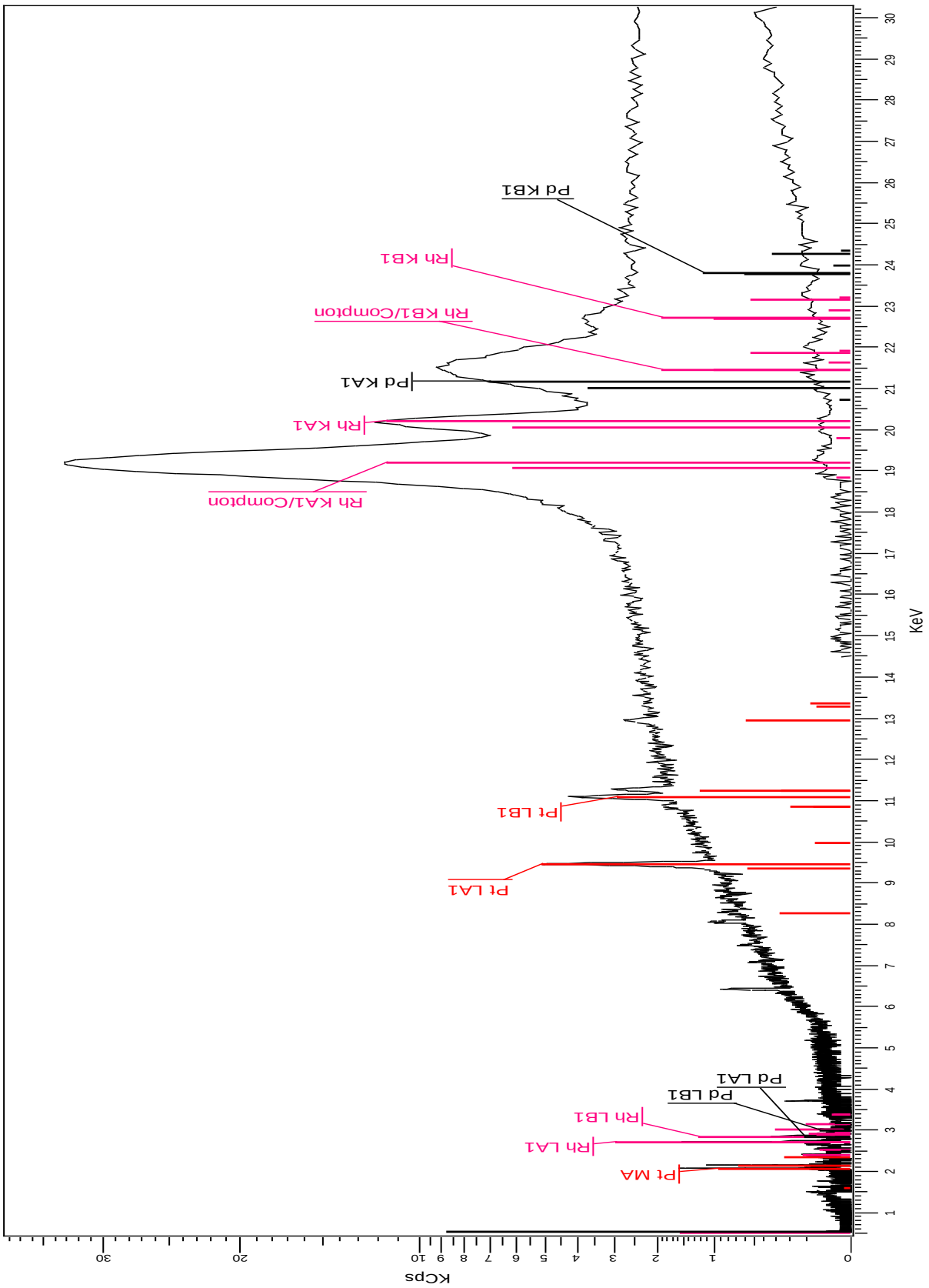


**Figure 37.** XRF spectrum of $Pt_{90}Rh_5Pd_5$ alloy nanoparticles. In the simulated XRF spectrum (thin vertical lines), the red lines represent Pt, pink lines represent Rh and and black lines represent Pd.

Table 3 below shows the composition detected by EDX (by weight percent) of the ternary alloy.

**Table 3.** Table to show elemental composition of the area of sample shown in Figure 32 by SEM/EDX analysis.

| Element | Weight /% | Atomic weight /% |
|---|---|---|
| Pt | 91.86 | 85.85 |
| Rh | 3.38 | 5.99 |
| Pd | 4.76 | 8.15 |

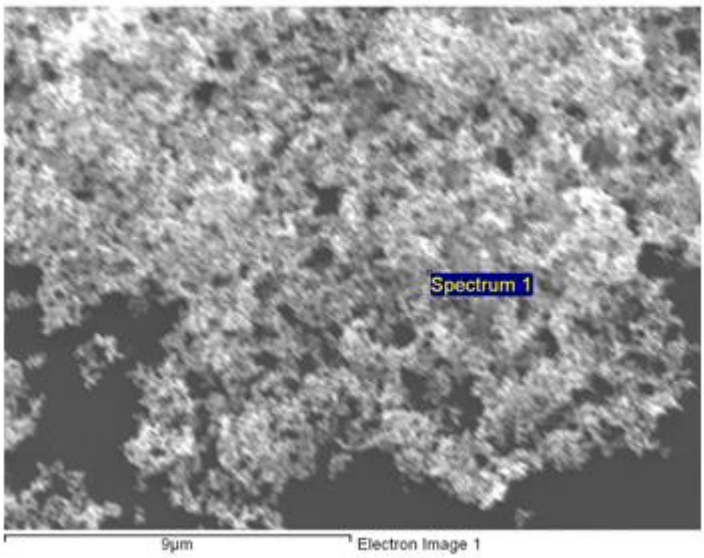


**Figure 38.** SEM image of $Pt_{90}Rh_5Pd_5$ nanoparticles.

EDX analysis (Figure 39) demonstrated that the atomic ratio of PtRhPd was 85:6:8 whereas the weight ratio was 91:4:5, respectively (average of four areas scanned). This is in agreement with the compositional data obtained from XRF. In all areas scanned, the amount of Pd was slightly higher than that of Rh. The large peak at the far left is carbon, since a glassy carbon (GC) disc was used on which to deposit the sample. This EDX pattern agrees with those in the literature of other ternary alloys.[60]

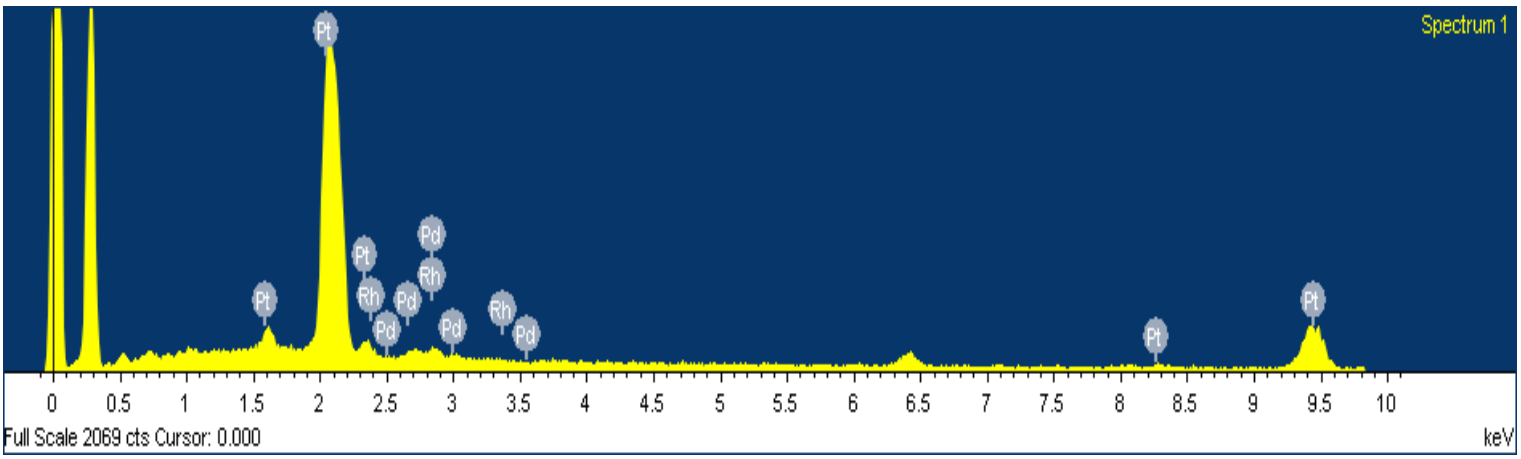


**Figure 39.** EDX pf $Pt_{90}Rh_5Pd_5$ nanoparticles.

As explained in Chapter Two Section Six, EDX, being a function of the SEM, is a surface analysis technique. Therefore, it should be borne in mind that only the first few surface layers of the sample will have been analysed by this technique. This may well explain the slightly higher amount of Pd compared to Rh in all areas scanned. For this reason, surface segregation will now be discussed.

A phenomenon known as surface segregation can influence the structure and hence the properties of an alloy. This means it is possible for the composition of the surface to be different from that of the bulk. The main driving forces for segregation are difference in surface energy, atomic radius and a tendency for some components to either mix or separate when in the bulk.[190] This is illustrated in Figure 40. Figure 40 shows what is known as a 'depth profile', in which the distribution of the atoms in the first three layers near the surface are shown, produced by Monte Carlo and MAEAM simulations. In the uppermost surface layer, no rhodium is present. Our results from EDX showing that Pd is mostly at the surface whereas Rh is in the bulk agrees with the literature. [191] Therefore our results are similar to those shown in Figure 39.

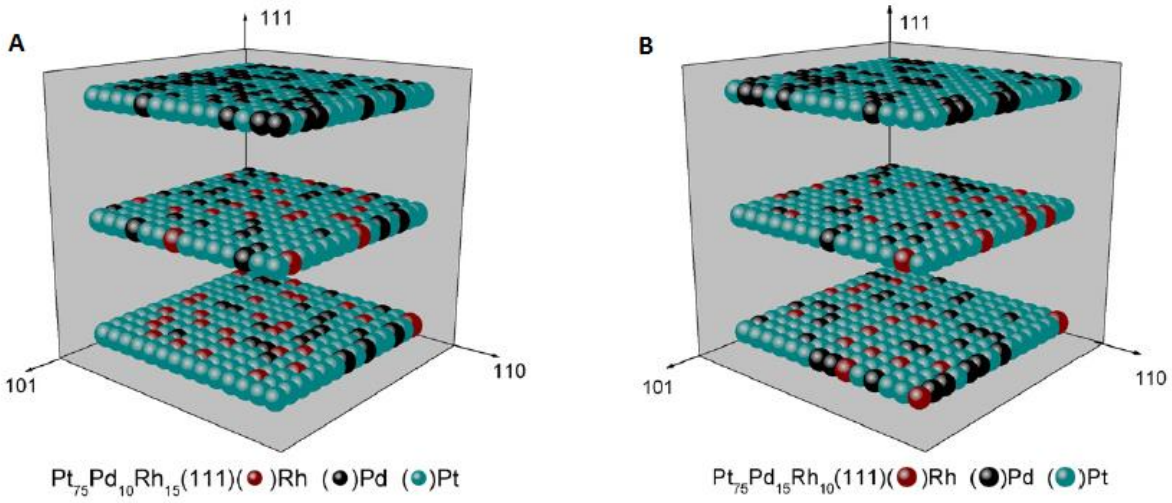


**Figure 40.** Graphical representation of the first three layers of A) $Pt_{75}Pd_{10}Rh_{15}$ and B) $Pt_{75}Pd_{15}Rh_{10}$ ternary alloys.[191]

Figure 40 shows an absence of Rh in the first, uppermost layer, whereas in the second and third (bulk) layers, rhodium is well regulated around platinum. Since the amount of Pt is around five times as much compared to amount of Rh in the alloys shown in Figure 40, this means that the likelihood of a position being occupied by Rh is around 1 in 5, if assumed that the atoms are disordered. This can be explained as the temperature set for the calculations was 927 °C, at which temperature a disordered structure would form and random distribution of atoms in the bulk layers would occur, as illiustrated.[191]

**Table 4**. Surface energies[192] and radii[193] of Pt, Rh and Pd in an fcc crystal structure.

| Property | Pt | Rh | Pd |
|---|---|---|---|
| Atomic radius[a] /x$10^{-10}$ m | 1.380 | 1.345 | 1.376 |
| Surface energy[b] /mJ/m $^2$ | 2.203 | 2.350 | 2.050 |

[a] Tyson

[b] Emsley

Table 4 shows the surface energy and atomic radii of the three metals in the ternary alloy, Pt Rh and Pd. Atomic radius and surface energy are two properties which can have an impact on where the atoms reside in a structure; as such, they can aid understanding of segregation. Surface energy can be defined as the 'surface excess free energy per unit area of a particular crystal'.[194] Looking at Table 4 it can be seen that Rh has the highest surface

energy; this means Rh is expected to reside within the bulk while Pd, having the lowest surface energy is expected to be present at the surface. This agrees with our results from EDX analysis (Figure 38). The additional motive for segregation is the nature of the metal-metal bond; whether it is exothermic or endothermic in nature. This of course is also affected by temperature.[191,195] To further investigate the PtRhPd surface, techniques such as LEED, AES and SXRD could be utilised, this will be touched upon again in the final conclusion and outlook.

### 4.3.2 Electrochemical characterisation

Following physical characterisation, particles were analysed electrochemically by cyclic voltammetry. Points of discussion will focus on the onset potential and mass activity from the oxidation voltammograms. Blank voltammograms with defined hydrogen adsorption features were not obtained in time as part of this work. The hydrogen adsorption and desorption features would be expected between 0.1 and 0.3 V while the area within 0.4 and 0.9 V would be expected to show desorption of hydroxyl species on rhodium.[182,185]

Figure 41 shows the voltammetric profile of the glycerol oxidation on the $Pt_{90}Rh_5Pd_5$ alloy nanoparticles in comparison with pure Pt nanoparticles prepared under similar conditions, is presented. As can be seen, the $Pt_{90}Rh_5Pd_5$ nanoparticles are highly active for the glycerol oxidation, displaying a mass activity of 50 mA/mg, eight times higher than that observed for Pt under the same conditions.

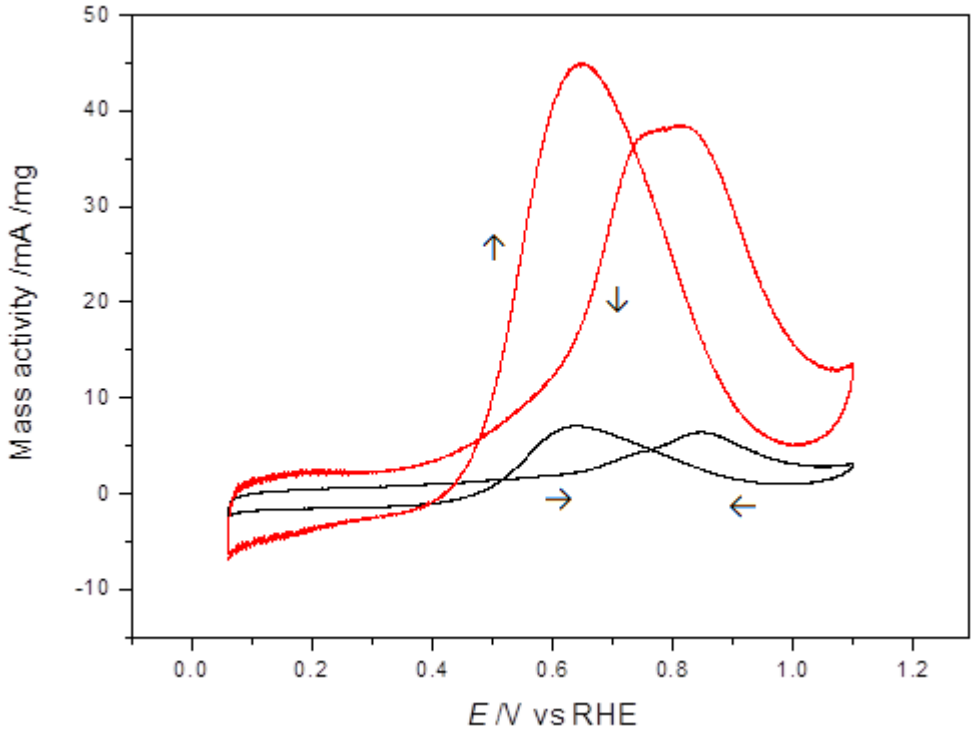


**Figure 41.** Voltammetric profile of PtRhPd nanoparticles (red) compared to Pt nanoparticles (black) in 0.5 M $H_2SO_4$ and 1 M glycerol at 10 mV/s.

The voltammetric profiles shown in Figure 40 are typical of multi-step reactions, as can be seen by the increase and then decrease in activity. This corresponds to either presence of competitive species or formation and consumption of said species. For both Pt and PtRhPd nanoparticles, the area between 0.6 V and 0.35 V on the voltammogram shows an absence of peaks corresponding to hydrogen adsorption/desorption. This is due to glycerol decomposing into species which then adsorb onto the catalyst surface. The onset potential is shifted to a slightly lower value for PtRhPd (~0.44 V) compared to Pt (~0.46 V). To explain the increase in activity, the synergistic effect of the alloy metals will be briefly mentioned. The higher activity of the ternary alloy compared to Pt is due to a change in the electronic structure of Pt by the addition of Rh and Pd, rendering the alloy a more active catalyst than Pt alone.[196] It must be noted, however, that the currents observed in this work, though significantly higher than pure Pt, are much lower than the state of the art PdBi catalyst which reached currents of 700 A/g in 0.1 M glycerol and 1 M KOH at a scan rate of 20 mV/s.

## 4.4 Conclusion

In this chapter, we have proved that the cathodic corrosion method is a versatile method capable of preparing ternary nanocatalysts with the same metal composition as the starting material bulk alloy. The particles were small, measuring less than 5 nm and homogeneously dispersed, as evidenced by the approximation from the XRD software and SEM results, respectively (see Figures 36 and 38).

The voltammetry results show the alloy to be an effective catalyst towards the glycerol electro-oxidation, exhibiting increased activity of around eight times that of pure Pt combined with a lower onset potential of 0.4 V compared to 0.5 V using Pt nanoparticles prepared under similar conditions. However, the activities obtained were still significantly lower than those from the state of the art catalysts prepared by Zalineeva et al.[186] The increased catalytic effect of our ternary alloy compared to Pt can be explained by the third body effect along with the synergistic effect of the three metals, as described in Chapter 1, Section 1.3.2.2 and briefly mentioned in this chapter.

In order to confirm the approximate particle size obtained from XRD, TEM could be used to analyse the sample. Additionally, product analysis could be undertaken using techniques such as HPLC for soluble species and OLEMS for gaseous species such as $CO_2$. Alternatively, a combined DEMS/ATR-FTIRS set up could be used, EMIRS has also been reported in the literature as a technique used to monitor the products of this reaction.[197] The durability of the catalyst could also be assessed using chronoamperometry. Additionally, XPS could be performed in order to further investigate the nature of the catalyst surface, perhaps to identify oxidation states of the metals and confirm the presence or absence of oxidised species ($PtO_x$).

Ultimately, these results are proof of principle that cathodic corrosion can be used to successfully prepare ternary alloys. Further improvements can be made by optimising parameters such as concentration of synthesis solution, frequency and voltage.

# Chapter 5

# Preparation of $Pt_{20}Ta_{80}$ nanoparticles

## 5.1 Introduction

### The PtTa system

Waterstrat[198] reported the phase diagram for PtTa in 1981 as illustrated in Figure 42. He wrote the main phases of the alloy to be Pt, $Pt_3Ta$, $Pt_2Ta$, PtTa and Ta in alloys with an atomic tantalum concentration of 0-19 %, 24-25.5 %, 32-33.3 %, 48.5-50 %, 65- 85 %, 84.5-86.5 % and 90.5 – 100 %, respectively. The phase diagram below shows that the PtTa alloy is formed at temperatures around 2000 °C, however this work reports preparation of a $Pt_{20}Ta_{80}$ alloy at room temperature via the cathodic corrosion method.

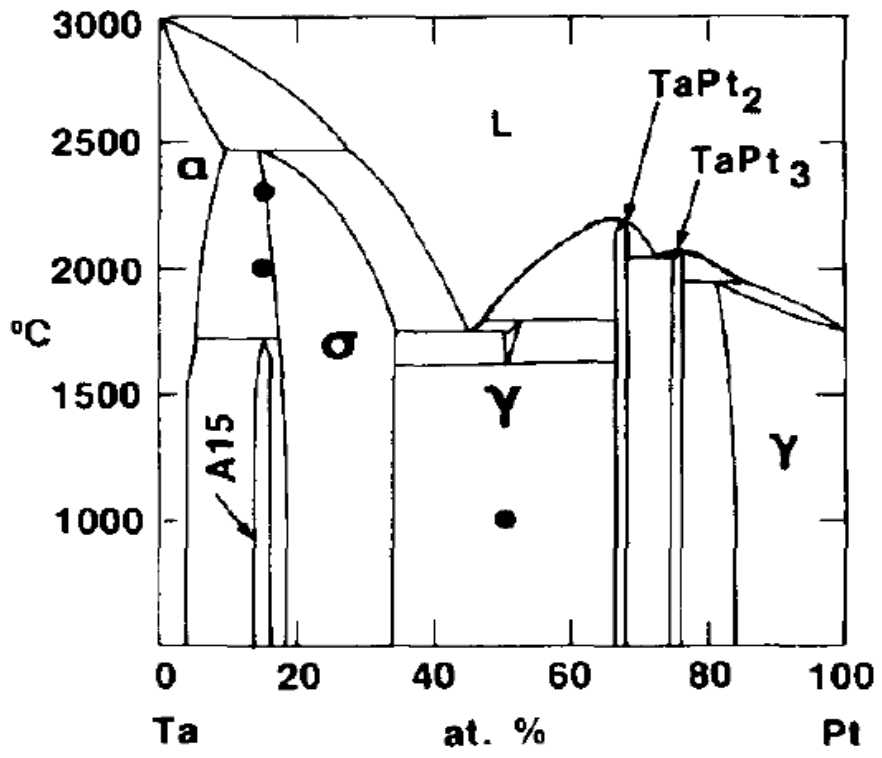


**Figure 42.** Schematic of the phase diagram for the PtTa alloy system.[198]

When two metals are not completely soluble in one another, they create separate phases, as can be seen here. This can be due to differences in atomic radii or different crystal

structures. Ta has either a tetragonal or bcc crystal structure of metallic radius 146 pm whereas Pt has a ccp crystal structure with an atomic radius of 139 pm.[199]

Since the difference in atomic radii is not hugely significant, the solid solution formed is likely to be substitutional as oppose to interstitial. ϒ and α represent different solid phases. The solid terminal phase, α, exists near the edge of the diagram at very low composition of Ta, whereas ϒ is an intermediate phase, since it exists at an intermediate composition of Ta. The α phase is a single solid phase region which is Ta rich. This phase diagram is indicative of an immiscible system, where the two metals are insoluble in one another. The eutectic point is visible at around 1700 °C, this composition (around 45 % Pt) will freeze at a lower temperature than all other compositions and this temperature is the minimum melting temperature of the PtTa alloy. L stands for liquidus which is a liquid phase region consisting of both Pt and Ta, everything below this is solid.

To date, there have been no reports of PtTa alloys being used as oxidation catalysts for PEMFCs. In 1985, an article was published by Couturier and Kirk[200] on preparation of a PtTa alloy by the co-sputtering method and its application in the oxygen reduction reaction.[200] Since then, more recent literature has mainly focused on the use of Ta as a support[95] or tantalum oxide modified platinum catalysts.[201] Preparation of $Pt_{70}Ta_{30}$ intermetallic catalysts has also been reported by Gregoire et al.,[202] these catalysts showed improved activity in the methanol and formic acid oxidation compared to platinum. This is shown in Figure 43 below where the solid lines and the dashed lines represent the forward and reverse scans, respectively.

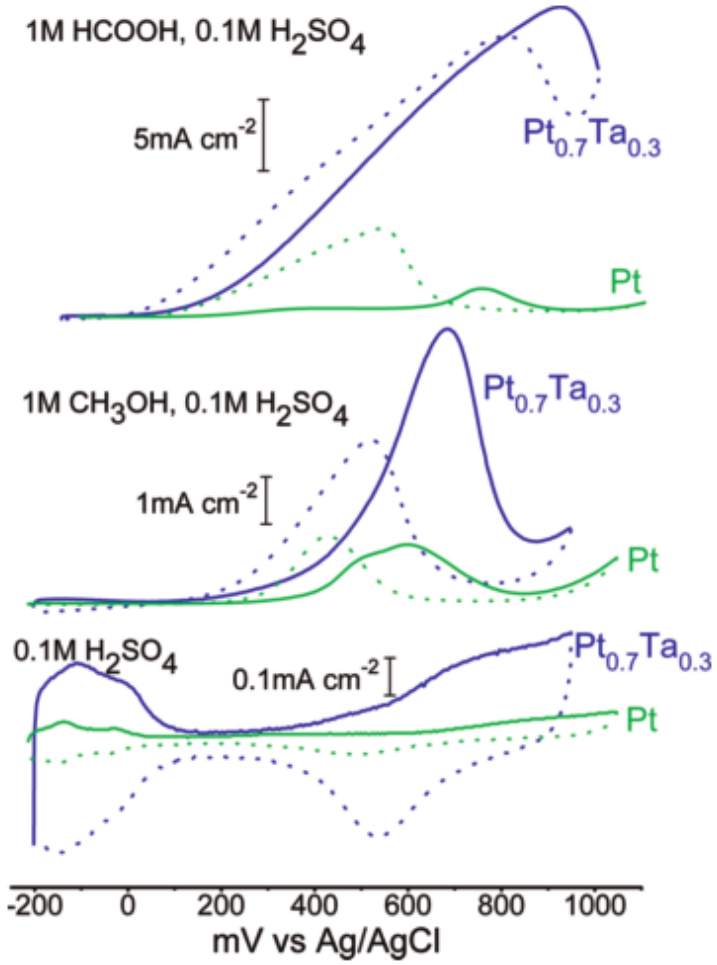


**Figure 43.** Blank and oxidation cyclic voltammograms of Pt compared with $Pt_{0.7}Ta_{0.3}$ in 0.1 M $H_2SO_4$ and 1 M HCOOH (top), 0.1 M $H_2SO_4$ and 1 M $CH_3OH$ (middle) and 0.1 M $H_2SO_4$ (bottom) .[202]

The PtTa alloy is difficult to prepare; the catalysts synthesised by Gregoire et al.[202] were formed via a multi-step sputter codeposition method. This process involved high temperatures of up to 500 °C along with the vacuum apparatus; this is costly in terms of energy and time. Toyoda et al.[203] prepared a Pt/$TaB_2$ catalyst also by a vacuum method using high temperatures of up to 1000 °C for the annealing process. Garsany[204] and Baturina[205] et al. prepared PtTa oxyphosphate and PtTa oxide catalysts, respectively, which also utilised very time inefficient multi-step processes lasting over several days.

In Figure 43, the voltammetric profile in the sulphuric acid solution shows the hydrogen adsorption/desorption and redox behaviour of the PtTa electrode, similar to a pure Pt electrode. The oxidation of methanol on the PtTa alloy starts approximately 80 mV earlier compared with the pure Pt electode. Higher current densities were achieved for both

oxidation reactions with the PtTa catalyst compared to pure Pt, this was thought to be due to presence of the Ta surface oxide.[202]

The objectives of this part of the project were to prepare and characterise PtTa catalysts using different parameters such as electrolyte, electrolyte concentration, voltage and using either the porous or non-porous part of initial PtTa alloy. Different techniques for characterisation were employed such as XRD, XRF and TEM to investigate the particle size and shape and whether the composition of the initial alloy was retained upon formation of nanoparticles.

## 5.2 Experimental

Synthesis and Characterisation

The source of the alloy was a TaPt 80:20 % wt metal block from HMW-Hauner. This block was broken into pieces using a hammer and one of these pieces was used as the working electrode for cathodic corrosion. It was observed that the outside of the alloy was smooth whereas the inside of the alloy was highly porous and brittle. Cathodic corrosion was performed on both the smooth outer part of the alloy and the inner porous part, for comparison. A piece of $Pt_{20}Ta_{80}$ metal was inserted into a beaker containing 10 ml of a 10 M NaOH solution. Nanoparticles were prepared using both the smooth outer sides of the metal and the porous bulk of the alloy. AC, square wave voltages of -10 – 0 V and -12 – 0 V were applied between the $Pt_{20}Ta_{80}$ working electrode and the platinum counter electrode to create two different nanoparticle samples. A non-rotating setup was used, with a micrometric screw to lower the wire into solution. Following synthesis, the nanoparticles were cleaned using Milli-Q water. X-ray diffraction, XRF and TEM analyses were carried out as detailed in the experimental sections of previous chapters.

## 5.3 Results and Discussion

Two sets of $Pt_{20}Ta_{80}$ nanoparticles were prepared, as detailed in the experimental section above. The working electrode was a PtTa alloy with a thin outer layer of smooth metal covering a porous bulk. It was observed that when the porous bulk was inserted into the solution, the metal disintegrated. This was thought to be due to bubbles forming within the

porous structure and hence causing it to fall apart. In contrast, when the smooth outer layer was carefully placed in contact with the solution, nanoparticles formed with no metal disintegration. The characterisation of these two samples will be presented and discussed in the following.

### 5.3.1 Physical Characterisation

This section will discuss the XRD, XRF and TEM results of the $Pt_{20}Ta_{80}$ catalysts. Focus will be on particle size, composition and homogeneity of the sample.

Figure 44 shows the XRD and XRF analyses of the source of PtTa and of the PtTa nanoparticles; from the compositional data from both the XRD and XRF software, it can be shown that the nanoparticles maintain the same composition as the source. (The XRD showed the composition of the nanoparticles to be $Pt_{0.2}Ta_{0.8}$ while the XRF showed it to be $Pt_{17}Ta_{83}$. The metal source was labelled as $Pt_{20}Ta_{80}$ and analyses were also run on this sample, giving exactly the same results for both XRD an XRF as those stated for the nanoparticles above).

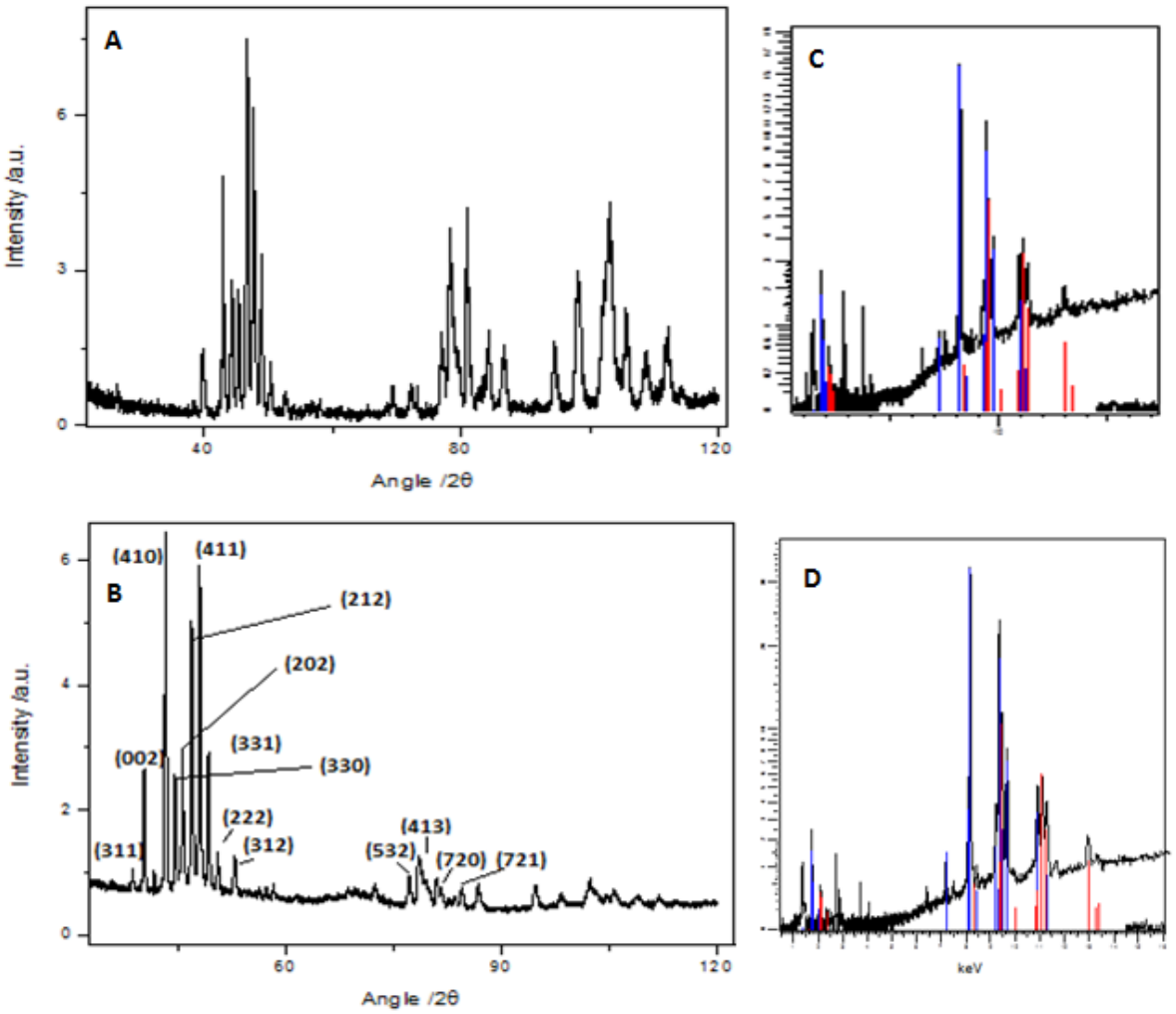


**Figure 44.** (A,B) XRD patterns of the initial $Pt_{20}Ta_{80}$ metal block and the PtTa nanoparticles, respectively. (C,D) XRF spectra of the initial $Pt_{20}Ta_{80}$ metal block and the PtTa nanoparticles, respectively. In the simulated XRF spectrum (thin vertical lines), the red lines represent Pt and blue lines represent Ta.

Figure 45 shows the XRD patterns of the initial metal source and the nanoparticles, as shown above although in Figure 45 they are overlaid for simpler visual comparison. It can be seen that both the initial source and the nanoparticles show the same reflections, although there is a difference in relative intensity of some of the reflections upon conversion of the metal source to nanoparticles. For example, reflections at lower values of 2θ remain of similar intensity, whereas those at higher values of 2θ (> 80 2θ) decrease in intensity when the metal is converted to nanoparticles. This could simply be due to not grinding the metal finely enough or the powder not being completely uniform, since texture can produce an effect on the pattern. The fine particles in the nanoparticles are difficult to compare with the more coarse particles from the initial alloy, so all that can be drawn from this is that the composition is retained.

The pattern of the peaks proved the formation of the alloy, since this corresponded to the compound $Pt_{0.2}Ta_{0.8}$, in agreement with the compositional data obtained from XRF (Figure 44). The $Pt_{20}Ta_{80}$ nanoparticles prepared were analysed by XRF analysis by pipetting a small amount (typically 200 µl) of catalyst dispersed in 1 ml of water onto a glassy carbon disc. The nanoparticles were observed to retain the initial composition of the alloy (17 % Pt and 83 % Ta).

The difference between using the two parts (smooth outer surface and porous interior) of the initial alloy metal during synthesis, could be observed in terms of particle size; the XRD of the $Pt_{20}Ta_{80}$ sample made using the porous metal (not shown) gave rise to broader peaks (indicative of smaller particle size and estimated to be 52 nm) and appeared to have a smaller average particle size as observed by TEM (see below). This was in contrast with the $Pt_{20}Ta_{80}$ sample prepared using the smooth, non-porous edges of the metal which exhibited sharper peaks in the XRD (with an estimated average particle size of 61 nm) and showed generally larger, agglomerated particles by TEM.

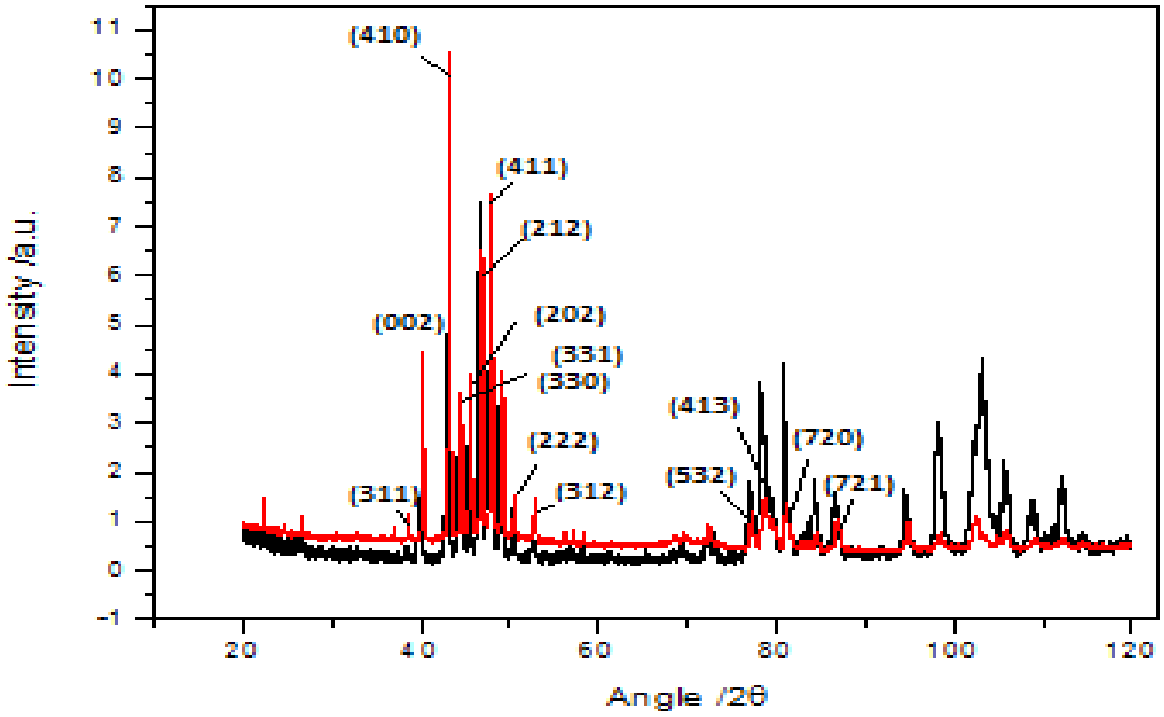


**Figure 45.** XRD diffractograms of the $Pt_{20}Ta_{80}$ alloy nanoparticles (red) prepared using the smooth, non-porous edges of the metal at ± 5 V offset -5 V and the initial metal sample ground to a powder (black).

**Table 5**. Table to show metals with their associated lattice parameter and crystal system

| **Metal** | **Lattice Parameter /$10^{-10}$ m** | **Crystal system** |
|---|---|---|
| Pt | 3.916 | cubic |
| PtTa | 10.02 | tetragonal, cubic |

TEM analysis (Figure 46) has been performed on the $Pt_{20}Ta_{80}$ catalyst prepared under conditions of 10 M NaOH with an applied voltage of ±6 V and an offset of -6 V. This catalyst was prepared using the porous bulk of the PtTa alloy working electrode, due to the porous nature of the metal, bubbles formed inside the structure and blew off small parts of the metal, leading to some physical disintegration. Therefore metal particles were present along with nanoparticles.

Figure 46 reveals some cubic shaped particles in the range of 84 - 171 nm in size, along with some darker areas within these structures which could be the nanoparticles. This is in agreement with the particle size from XRD analysis, since the estimate provided from XRD gives an average particle size. On the other hand, thought data from the XRD agreed that cubic nanoparticles were present; the information seemed to suggest that the majority of the PtTa nanoparticles in the same were within a tetragonal crystal system. However, this is not surprising since cubic and tetragonal are very similar, differing only by the one unequal axis in tetragonal, while both structures share the similarity of having all angles 90 ° (see Table 5). The TEM images A and B in Figure 46 clearly show the presence of the 90 ° angles typical of cubic nanoparticles.

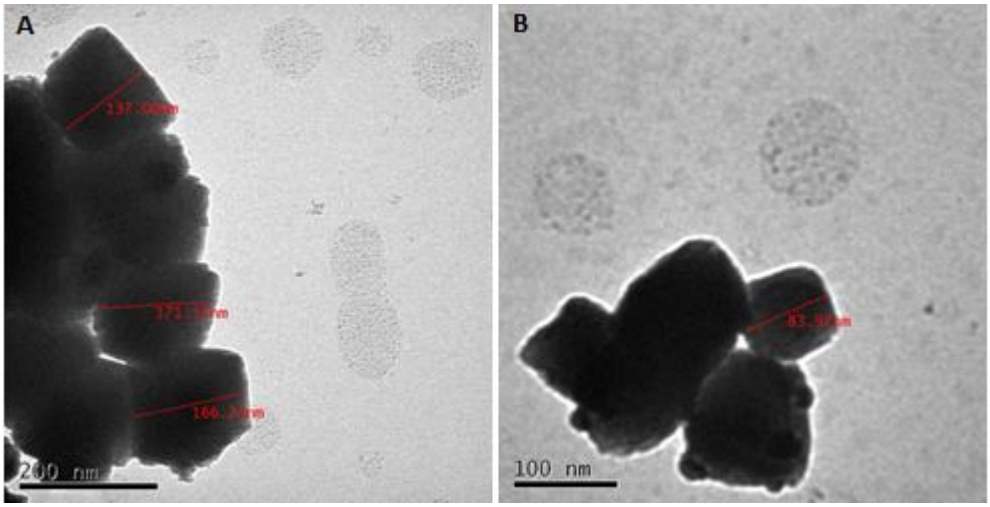


**Figure 46.** TEM images of different areas of the $Pt_{20}Ta_{80}$ alloy sample (synthesis conditions of 10 M NaOH ±6 V offset -6 V using porous bulk).[a]

[a] The initial PtTa alloy sample consisted of a smooth outer layer of metal and a porous interior. We prepared nanoparticles using both parts of this metal for comparison.

Cathodic corrosion is known to form preferentially (100) oriented nanoparticles, the presence of (100) sites can be evidenced through running blank voltammograms.[17] The cubic nanoparticles, with their (100) facets are actually the least catalytically active.[206] Therefore future work adjusting parameters in synthesis should focus on methods likely to reduce the number of (100) facets present. The presence of (100) facets would not be surprising since the cation can influence what facets are formed. It is documented that using high concentrations of NaOH in the cathodic corrosion method facilitate (100) site formation while lower concentrations e.g. 1 M would form polycrystalline nanoparticles.[15] A high concentration of 10 M was indeed used to prepare these nanoparticles.

## 5.4 Conclusion

$Pt_{20}Ta_{80}$ nanoparticles were synthesised by the cathodic corrosion method and characterised by XRD, XRF and TEM. The nanoparticles were found to retain the initial composition of the starting alloy; however they exhibited an inhomogeneous particle size distribution as can be observed from the TEM images. The nanoparticles prepared using the porous part of the metal had a smaller average particle size of 52 nm compared with the value of 61 nm obtained for the sample prepared using the non-porous edges of the metal.

Offsets of up to -6 V were used in this work, the greater the offset, the more likely nanoparticles are to form. However a DC offset more negative than -6 V is an inefficient use of energy. Offsets were negative, since nanoparticles are more likely to form at negative potentials and this ensures the potential is kept negative during the whole cycle. Use of a DC offset also increases the amount of (100) sites which are known to be the most catalytically active (yet most easily poisoned, however this is counteracted by the effect of the alloying metal).[15] The offset was changed slightly during the synthesis of the PtTa nanoparticles to observe if this had an effect on either particle size and/or shape. In order to judge whether this was indeed the case, a larger range of potential conditions would need to be used for comparison, however the PtTa nanoparticles could only be synthesised within a very small voltage window and many were attempted. The results from TEM were also inconclusive; ideally the TEM experiments could be repeated.

It is known that different phases can exist due to temperature and pressure changes or even because of the synthesis method. The possible reconstruction of the crystal can be classed as a first order solid-solid phase transition. The existence of phase transition or existence of two different crystal phases within the sample can be evidenced from the splitting of the diffraction peaks. To elucidate whether the peak splitting is assigned to another crystal structure in the material, different compositions of PtTa nanoparticles could be prepared and analysed by XRD, and the appearance of this peak monitored according to the composition. Additionally, high temperature X-ray diffraction could be used to decipher whether the splitting is because of a secondary phase. Before applying these particles to electrochemical reactions, it was intended to optimise the synthesis conditions. Therefore,

further optimising of parameters and application of these nanoparticles in fuel cell reactions will be part of future investigation.

## 6. Conclusion and outlook

In summary, we reported the preparation of PtBi and PtPb electrocatalysts of varying composition along with PtTa and the ternary alloy PtRhPd via the cathodic corrosion method. This work has demonstrated the two different approaches of cathodic corrosion; one method in which the alloy is in the solution (PtBi and PtPb) and one method is which the alloy is the working electrode (PtTa and PtRhPd). It should be emphasised that aspects such as time, process cost, energy and loss of precious metal are all minimal. These three sets of alloy nanoparticles exhibited small particle sizes in the range of 4-5 nm,(significantly smaller than most of those reported in the literature) and showed some degree of shape control which was manipulated through reaction conditions including the voltage offset and electrolyte used.

Homogeneity of the PtBi and PtPb nanoparticle samples were evaluated through TEM and they showed a homogeneous particle size distribution (5.3 ± 1.2 nm and 4.2 ± 0.7 nm, respectively). Shape was confirmed through TEM and XRD. It is difficult to say whether the shapes obtained from the TEM agree with those from the XRD. This is because many factors would need to be monitored, such as how/if the composition affects lattice parameter and shape, whether voltage and offset also affect shape and all phases and crystal systems present would also need to be taken into account. Perhaps investigation into some of this could be included in future work for this project.

The PtTa nanoparticles had a much larger lattice parameter than the other alloys. This is because Ta has the largest atomic radii (146 pm) out of all the other alloying metals, so it is not surprising. The sample with the smallest lattice parameter was PtRhPd, this was smaller than pure Pt, which is reasonable since Rh and Pd have slightly smaller radii than Pt. Lead and bismuth are adjacent in the periodic table and so will have similar atomic radii. However, the lattice parameters vary significantly, as do the shapes, with the value for PtPb

being closer to that of Pt than PtBi. This is likely due to the fact that both Pt and PtPb have cubic structures, whereas PtBi is hexagonal and therefore has a larger lattice.

Bulk composition was analysed by EDX and XRF for the PtBi, PtPb and PtRhPd nanoparticles. Differences between bulk and surface composition of the PtRhPd and PtPb catalysts suggest a degree of surface segregation. Surface segregation phenomena will be discussed in some detail as part of this work, since not only is it an interesting concept but also a very important issue to consider in catalyst design. It can have a huge influence on surface properties and hence activity of the catalyst; it therefore reveals opportunities for optimisation of catalytic activity, which is certainly of interest to this work. The driving force for segregation is thermodynamic stability; a reduction in surface energy of the particle. There are several theories of segregation which include the Langmuir-McLean theory [207,208]and free energy of grain boundary segregation in binary systems.[208]

Small gas molecules such as diatomic oxygen and diatomic hydrogen can adsorb to the surface of nanoparticles, thereby lowering the energy of the nanoparticle surface. To relate this to the work described here an also show the competition between surface free energy and chemical affinity, the PtRhPd alloy will be briefly discussed. Rhodium has a higher surface energy than Pt and Pd, however since Rh forms stable oxide compounds, under oxidising conditions this causes Rh to migrate to the surface as was observed in this work (See Chapter Three). Formation of stable oxide species reduces the surface energy. Techniques to analyse composition (XRF and EDX) were conducted for the PtPb, PtBi[100] and PtRhPd nanoparticles. For the PtRhPd sample, EDX was found to be a more sensitive bulk analysis technique, where it managed to determine the weight % of Pd and Rh exactly, whereas XRF did not, it only confirmed their presence and that the percentage of Pt was ninety, therefore the percentage of the two alloying metals must add up to ten. The EDX of PtBi and PtPb, as with the results for Pt in PtRhPd showed figures of Bi and Pb slightly higher than those obtained from XRF. This was possibly due to the sample thickness; the sample used for XRF was thicker than that used for EDX.

Moving onto electrochemistry of the alloys, the PtPb nanoparticles showed the highest activity (800 mA/mg) out of all the samples towards the reactions tested, compared to PtBi

(630 mA/mg)[100] and PtRhPd (45 mA/mg). All three catalysts achieved an activity greater than that of pure platinum; PtRhPd was nine times more active than Pt nanoparticles prepared under the same conditions when used in the glycerol oxidation, while PtBi and PtPb were an astounding two orders of magnitude greater in activity than platinum alone. This enhanced activity of the alloys compared to the single metal is due to the third body effect. All three alloys also exhibited lower onset potential than pure platinum; that of PtRhPd was around 0.40 V whereas that of Pt was around 0.52 V in the glycerol oxidation. For the formic acid oxidation, PtBi showed an onset of 0.1 V and PtPb 0.2 V compared to 0.4 V for platinum. In terms of durability, the top performer was PtPb, which displayed steady currents, in contrast to PtBi, whose activity started off higher but then decayed more quickly. Durability of the PtRhPd catalyst would be interesting to assess in future work.

Relating this to future work, further experimental techniques could be employed to study composition and segregation behaviour of the alloy catalysts in more detail. Such techniques could include HAADF, EELS, AES, LEIS, FTIR and XAS.[209,210] Sizes obtained from TEM and/or XRD could be further backed up by SAXS.[209] In situ surface experiments would be beneficial to look into the change that the catalyst may undergo during the reaction. These results could be compared to durability tests which are achieved through constant cycling within a specific potential range. Due to time constraints, unfortunately these avenues could not be looked into as part of this project. It would also be interesting to correlate lattice parameter with varying compositions of each of the metal catalysts and see whether it follows Vergard's Law.[60] Future work could also focus on preparation of another ternary alloy such as PtRuPd. Platinum alloyed with ruthenium has been known to have high activity towards the oxidation of small organic molecules such as formic acid and methanol.[59] Finally, and most importantly, more fine tuning of the parameters (voltage, frequency, concentration, choice of electrolyte) is needed to fully investigate these effects on the shape and activity of our nanoparticles.

The outlook for this area of work is promising. Work within this group has shown that $BiVO_4$ can also be prepared by our method, along with some other metal oxides, with intention to prepare more alloys such as PdSn for application in $CO_2$ reduction. Cathodic corrosion is not without its limits, for example it is not effective for all metals, such as titanium. More

generally, further data is needed to continue to improve our understanding on this topic if we are to make sustained progress in catalyst design and application, with a view to commercialisation of fuel cells. On the whole, there is every reason that shape controlled alloy nanoparticles will play a leading role in development of promising anode catalysts and the commercialisation of fuel cells, thereby moving the world towards a greener future.

## References


1 S. J. Peighambardoust, S. Rowshanzamir and M. Amjadi, *Int. J. Hydrogen Energy*, 2010, **35**, 9349–9384.

2 R. L. Borup, J. R. Davey, F. H. Garzon, D. L. Wood and M. A. Inbody, *J. Power Sources*, 2006, **163**, 76–81.

3 U. Lucia, *Renew. Sustain. Energy Rev.*, 2014, **30**, 164–169.

4 S.-H. Yang, C.-Y. Chen and W.-J. Wang, *J. Power Sources*, 2010, **195**, 2319–2330.

5 D. S. Falcão, V. B. Oliveira, C. M. Rangel and a. M. F. R. Pinto, *Renew. Sustain. Energy Rev.*, 2014, **34**, 58–70.

6 A. I. Yanson, P. Rodriguez, N. Garcia-Araez, R. V Mom, F. D. Tichelaar and M. T. M. Koper, *Angew. Chem. Int. Ed. Engl.*, 2011, **50**, 6346–50.

7 P. Rodriguez, F. D. Tichelaar, M. T. M. Koper and A. I. Yanson, *J. Am. Chem. Soc.*, 2011, **133**, 17626–9.

8 P. Rodriguez, D. Plana, D. J. Fermin and M. T. M. Koper, *J. Catal.*, 2014, **311**, 182–189.

9 U.N., *World Population Prospects: The 2015 Revision*, 2015.

10 G. Rothenburg, *Catalysis: Concepts and Green Applications*, Wiley-VCH, Germany, 2008.

11 B. Braunchweig, D. Hibbitts, M. Neurock and a. Wieckowski, *Catal. Today*, 2013, **202**, 197–209.

12 J. R. H. Ross, *Heterogeneous Catalysis: Fundamentals and Applications*, Elsevier, 2012.

13 H. S. Taylor, *Proc. R. Soc.*, 1925, **108**, 105.

14 G. A. Somorjai, *Acc. Chem. Res.*, 1976, **9**, 248–256.

15 M. Duca, P. Rodriguez, A. I. Yanson and M. T. M. Koper, *Top. Catal.*, 2013, **57**, 255–264.

16 Y. I. Yanson and A. I. Yanson, *Low Temp. Phys.*, 2013, **39**, 304–311.

17 M. Duca, M. C. Figueiredo, V. Climent, P. Rodriguez, J. M. Feliu and M. T. M. Koper, *J. Am. Chem. Soc.*, 2011, **133**, 10928–39.

18 T. H. M. Housmans, A. H. Wonders and M. T. M. Koper, *J. Phys. Chem. B*, 2006, **110**, 10021–10031.

19 F. J. Vidal-Iglesias, J. Solla-Gullón, V. Montiel, J. M. Feliu and A. Aldaz, *J. Phys. Chem. B*, 2005, **109**, 12914–9.

20 J. F. Gomes, F. B. C. de Paula, L. H. S. Gasparotto and G. Tremiliosi-Filho, *Electrochim. Acta*, 2012, **76**, 88–93.

21 C. Bartholomew, *Kirk-Othmer Encycl. Chem. Technol.*, 2003, **5**, 255–322.

22 W. M. Grove, *London Edinburgh Philos. Mag.*, 1839, **14**, 127–130.

23 C. Russell, *Chem. World*, 2003.

24 D. McDonald and L. B. Hunt, *A History of Platinum and its Allied Metals*, Johnson Matthey, London, 1982.

25 Royal Society (Great Britain), *Proceedings of the Royal Society of London*, RareBooksClub, 2012.

26 W. Ostwald, *Electrochemistry: History and Theory*, 1896.

27 Q. Li, R. He, J. O. Jensen and N. J. Bjerrum, *Chem. Mater.*, 2003, **15**, 4896–4915.

28 M. Z. F. Kamarudin, S. K. Kamarudin, M. S. Masdar and W. R. W. Daud, *Int. J. Hydrogen Energy*, 2013, **38**, 9438–9453.

29 EPA, *Pollinator Prot.*, 2016.

30 ICIS, *ICIS Chem. Bus.*, 2003.

31 H. Kieczska and W. Reutemann, in *Ullman's Encyclopedia of Industrial Chemistry*, Wiley-VCH, Weinheim, 2002.

32 T. Stavrakou, J.-F. Müller and J. Peeters, *Nat. Geosci.*, 2012, **5**, 26–30.

33 S. N. Bizzari and M. Blagoer, in *Chemical economics handbook*, SRI consulting, 2013.

34 P. G. Jessop, *Handbook of Homogeneous Hydrogenation*, Wiley-VCH, Weinheim, 2007.

35 P. G. Jessop, F. Joo and C.-C. Tai, *Coord. Chem. Rev*, 2004, **248**, 2425.

36 F. D. Chattaway, *J. Chem. Soc. Trans.*, 1914, **105**, 151–156.

37 J. Albert, R. Wölfel, A. Bösmann and P. Wasserscheid, *Energy Environ. Sci*, 2012, 7956.

38 Y. Kang and C. B. Murray, in *Encyclopedia of Applied Electrochemistry*, 2014, pp. 895–901.

39 H. R. Corti and E. R. Gonzalez, Eds., *Direct Alcohol Fuel Cells: Materials, Performance, Durability and Applications*, Springer Netherlands, 1st edn., 2014.

40 S. R. Ragsdale and C. Ashfield, *ECS Trans.*, 2008, **16**, 1847–1854.

41 C. H. Zhou, H. Zhao, D. S. Tong, L. M. Wu and W. H. Yu, *Catal. Rev.*, 2013, **55**, 369–453.

42 M. Pagliaro and M. Rossi, *The Future of Glycerol*, RSC Publishing, 2nd edn., 2010.

43 R. Christoph, B. Schmidt, U. Steinberner, W. Dilla and R. Karinen, in *Ullmann's Encyclopedia of Industrial Chemistry*, Wiley-VCH, 2006.

44 J. N. Chheda, G. W. Huber and J. A. Dumesic, *Angew. Chem., Int. Ed.*, 2007, **46**, 7164–7183.

45 B. Katryniok, H. Kimura, E. Skrzyńska, J.-S. Girardon, P. Fongarland, M. Capron, R. Ducoulombier, N. Mimura, S. Paul and F. Dumeignil, *Green Chem*, 2011, **13**, 1960–1979.

46 *Sci. Am.*, 2008.

47 R. Van Noorden, *Chem. World*, 2007, **4**, 8–19.

48 P. S. Fernández, M. E. Martins and G. a. Camara, *Electrochim. Acta*, 2012, **66**, 180–187.

49 D. Nilles, *Biodiesel Mag.*, 2005.

50 W. Hu, D. Knight, B. Lowry and A. Varma, 2010, 10876–10882.

51 M. Namiki, *Adv. Food Res.*, 1988, **32**, 115–184.

52 R. Garcia, M. Besson and P. Gallezot, *Appl. Catal., A,* 1995, **127**, 165–176.

53 H. Kimura and K. Tsuto, *Appl. Catal., A,* 1993, **96**, 217–228.

54 H. Kimura and D. Keiichi, *Appl. Catal., A,* 1993, **96**, 217–228.

55 A. Brandner, K. Lehnert, A. Bienholz, M. Lucas and P. Claus, *Top. Catal.*, 2009, **52**, 278.

56 L. Xie and J. Hainan, *Nat. Sci.*, 2007, **20**, 251.

57 S. Demirel, K. Lehnert, M. Lucas and P. Claus, *Appl. Catal., B,* 2007, **70**, 637.

58 A. M. Sheikh, P. S. Correa, E. L. da Silva, I. D. Savaris, S. C. Amico and C. F. Malfatti, in *International Conference on Renewable Energies and Power Quality*, Spain, 2013.

59 L. Feng, L. Yan, Z. Cui, C. Liu and W. Xing, *J. Power Sources*, 2011, **196**, 2469–2474.

60 F. Colmati, E. Antolini and E. R. Gonzalez, *J. Alloys Compd.*, 2008, **456**, 264–270.

61 R. Ferrando, J. Jellinek and R. L. Johnston, *Chem. Rev.*, 2008, **108**, 845–910.

62 R. L. Johnston, *Atomic and Molecular Clusters*, Taylor & Francis, London, 2002.

63 F. E. Kruis, H. Fissan and A. Peled, *J. Aerosol Sci.*, 1998, **29**, 511–535.

64 C. Stoffelsma, P. Rodriguez, G. Garcia, N. Garcia-araez, D. Strmcnik and N. M. Markovic, 2010, 16127–16133.

65 J. Perez, V. a. Paganin and E. Antolini, *J. Electroanal. Chem.*, 2011, **654**, 108–115.

66 H. Yano, J. Inukai, H. Uchida, M. Watanabe, P. K. Babu, T. Kobayashi, J. H. Chung, E. Oldfield and A. Wieckowski, *Phys. Chem. Chem. Phys.*, 2006, **8**, 4932–9.

67 C.-H. Jung, T. Zhang, B.-J. Kim, J.-D. Kim, C.-K. Rhee and T.-H. Lim, *Bull. Korean Chem. Soc.*, 2010, **31**, 1543–1550.

68 D. Wang and Y. Li, *Adv. Mater.*, 2011, **23**, 1044–60.

69 A. Dehghan Banadaki and A. Kajbafvala, *J. Nanomater.*, 2014, **2014**, 1–28.

70 H. Y. Chen and N. Savvides, *J. Cryst. Growth*, 2010, **312**, 2328–2334.

71 J.-Y. Wang, *Int. J. Hydrogen Energy*, 2009, **34**, 3771–3777.

72 D. a. Ramirez, L. E. Murr, S. J. Li, Y. X. Tian, E. Martinez, J. L. Martinez, B. I. Machado, S. M. Gaytan, F. Medina and R. B. Wicker, *Mater. Sci. Eng. A*, 2011, **528**, 5379–5386.

73 T. Chen, C. Ge, Y. Zhang, Q. Zhao, F. Hao and N. Bao, *Int. J. Hydrogen Energy*, 2015, **40**, 4548–4557.

74 Y. Kwon, Y. Birdja, I. Spanos, P. Rodriguez and M. T. M. Koper, *ACS Catal.*, 2012, **2**.

75 Y. Kang, L. Qi, M. Li, R. E. Diaz, D. Su, R. R. Adzic, E. Stach, J. Li and C. B. Murray, 2012, 2818–2825.

76 X. Yu and P. G. Pickup, *Int. J. Green Energy*, 2009, **6**, 571–582.

77 Y.-W. Lee, A.-R. Ko, S.-B. Han, H.-S. Kim and K.-W. Park, *Phys. Chem. Chem. Phys.*, 2011, **13**, 5569–72.

78 J. C. Bauer, X. Chen, Q. Liu, T.-H. Phan and R. E. Schaak, *J. Mater. Chem.*, 2008, **18**, 275–282.

79 C.-M. Hung, *Int. J. Hydrogen Energy*, 2012, **37**, 13815–13821.

80 L. Demarconnay, S. Brimaud, C. Coutanceau and J.-M. Léger, *J. Electroanal. Chem.*, 2007, **601**, 169–180.

81 R. L. Johnston, *Metal Nanoparticles and Nanoalloys*, Elsevier Science, Oxford, 1st Editio., 2012, vol. 3.

82 A. V Ruban, H. L. Skriver and J. K. Norskov, *Phys Rev B*, 1999, **59**, 15990.

83 A. M. Molenbroek, S. Haukka and B. S. J. Clausen, *1998*, **102**, 10680.

84 S. P. E. Smith, K. F. Ben-dor and D. Abrun, *Langmuir*, 2000, **16**, 787–794.

85 J. Jellinek, in *Metal-ligand Interactions*, 1996, pp. 325–360.

86 N. M. Markovic, in *Catalysis and Electrocatalysis at Nanoparticle Surfaces*, Marcel Dekker, New York, 2003, p. 911.

87 A. E. Russell and A. Rose, *Chem. Rev.*, 2004, **104**, 4613–4635.

88 B. E. Conway and B. V Tilak, *Electrochim. Acta*, 2002, **47**, 3571–3594.

89 M. W. Breiter, *Reaction mechanisms of the H2 oxidation/evolution reaction*, 2010.

90 M. A. Montero, J. L. Fernández, M. R. Gennero de Chialvo and A. C. Chialvo, *J. Power Sources*, 2014, **254**, 218–223.

91 M. Wesselmark, KTH, Sweden, 2010.

92 E. Skulason, V. Tripkovic, M. Bjorketun and S. Gudmundsdottir, *J. Phys. Chem.*, 2010, **114**, 110913.

93 N. M. Markovic, B. N. Grgur and P. N. Ross, *J. Phys. Chem. B*, 1997, **5647**, 5405–5413.

94 J. Monzó, M. T. M. Koper and P. Rodriguez, *Chemphyschem*, 2012, **13**, 709–15.

95 Y. Chen, J. L. G. Fierro, T. Tanaka and I. E. Wachs, *J. Phys. Chem. B*, 2003, **107**, 5243–5250.

96 M. Inaba, M. Ando, A. Hatanaka, A. Nomoto, K. Matsuzawa, A. Tasaka, T. Kinumoto, Y. Iriyama and Z. Ogumi, *Electrochim. Acta*, 2006, **52**, 1632–1638.

97 A. I. Yanson and Y. I. Yanson, *Low Temp. Phys.*, 2013, **39**, 312.

98 J. Ghilane, C. Lagrost, M. Guilloux-Viry, J. Simonet, M. Delamar, C. Mangeney and P. Hapiot, *J. Phys. Chem. C*, 2007, **111**, 5701–5707.

99 A. Karpov, M. Konuma and M. Jansen, *Chem. Commun. (Camb).*, 2006, 838–40.

100 E. Bennett, J. Monzo, J. Humphrey, D. Plana, M. Walker, C. Mcconville, D. Fermin, A. Yanson and P. Rodriguez, *ACS Catal.*, 2016, **6**, 1533–1539.

101 S. C. Sevov, *Zintl Phases in Intermetallic Compounds, Principles and Practice: Progress*, John Wiley & Sons. Ltd, 2002.

102 M. Jansen, *Solid State Sci.*, 2005, **7**, 1464–1474.

103 J. Simonet, *Electrochem. commun.*, 2015, **53**, 15–19.

104 J. Simonet, E. Labaume and J. Rault-Berthelot, *Electrochem. commun.*, 1999, **1**, 252–256.

105 A. Karpov, J. Nuss, U. Wedig and M. Jansen, *Angew. Chem. Int. Ed*, 2003, **42**, 4818 –4821.

106 H. K. Herglotz, *J. Colloid Interface Sci.*, 1985, **105**, 447–455.

107 R. E. Davis, D. L. Rousseau and R. D. Board, *Science*, 1971, **171**, 167–170.

108 C. Corti and R. Holliday, Eds., *Gold: Science and Applications*, CRC Press, 2010.

109 J. Kohler and J.-H. Chang, *Angew. Chem*, 2000, **112**, 2077.

110 J. Köhler and J.-H. Chang, *Angew. Chemie Int. Ed.*, 2000, **39**, 1998–2000.

111 J. Köhler and J.-H. Chang, *Referateband*, 1997, **12**.

112 J. Kohler, J.-H. Chang and M.-H. Whangbo, *J. AM. CHEM. SOC*, 2005, **127**, 2277–2284.

113 F. J. Vidal-Iglesias, J. Solla-Gullón, E. Herrero, V. Montiel, a. Aldaz and J. M. Feliu, *Electrochem. commun.*, 2011, **13**, 502–505.

114 C. Aliaga, J. Y. Park, Y. Yamada, H. S. Lee, C. Tsung, P. Yang and G. a Somorjai, 2009, 6150–6155.

115 N. Robotti, *Rend. Lincei*, 2012, **24**, 7–18.

116 B. B. He, *Two-Dimensional X-ray Diffraction*, John Wiley & Sons. Ltd, 2009.

117 U. Holzwarth and N. Gibson, *Nat. Nanotechnol.*, 2011, **6**, 21027.

118 J. W. Niemantsverdriet, *Spectroscopy in Catalysis*, VCH, 1995.

119 D. Basu and S. Basu, *Electrochim. Acta*, 2011, **56**, 6106–6113.

120 A. R. Denton and N. W. Ashcroft, *Phys. Rev. A*, 1991, **43**, 3161.

121 D. R. Baer, D. J. Gaspar and P. Nachimuthu, *Anal Bioanal Chem*, 2010, **396**, 983–1002.

122 K. Watts, 2013.

123 Z. Embong, *XPS, AES and laser raman spectroscopy: A fingerprint for a materials surface characterisation*, 2011.

124 J. C. Yang, M. W. Small, R. V Grieshaber and R. G. Nuzzo, *Chem. Soc. Rev.*, 2012, **41**, 8179–94.

125 A. K. Datye, *J. Catal.*, 2003, **216**, 144–154.

126 E. F. Schumacher, *Am. Lab.*, 2014, **46**, 24–26.

127 H. Taube, *Electron Transfer Reactions of Complex Ions in Solution*, Academic Press: New York, 1970.

128 A. J. Bard, *J. Am. Chem. Soc.*, 2010, **132**, 7559–7567.

129 G. A. Mabbott, *J. Chem. Educ.*, 1983, **60**, 697–702.

130 P. T. Kissinger, W. Lafayette and W. R. Heineman, 702–706.

131 F. Scholz, *Electroanalytical Methods: Guide to Experiments and Applications*, Springer-Verlag, Berlin, 2nd edn., 2010.

132 J. M. Feliu and E. Herrero, *Science (80-. ).*, 2010, **6**, 161–172.

133 H. Baltruschat, *J. Am. Soc. Mass Spectrom.*, 2004, **15**, 1693–1706.

134 J. Koryta, J. Dvorak and L. Kavan, *Principles of Electrochemistry*, Wiley, New York, 1993.

135 A. Capon and R. Parsons, 1973, **44**, 239–254.

136 H. Wang, L. Alden, F. J. DiSalvo and H. D. Abruna, *Phys. Chem. Chem. Phys.*, 2008, **10**, 3739–3751.

137 K. Kunimatsu, *J. Electroanal.*, 1986, **213**, 149–157.

138 J. Clavilier, *J. Electroanal. Chem.*, 1987, **236**, 87–94.

139 J. Heitbaum, *Electrochim. Acta*, 1985, **31**, 943–948.

140 S. G. Sun, J. Clavilier and A. Bewick, *J. Electroanal. Chem.*, 1988, **240**, 147–159.

141 M. T. M. Koper, *Fuel Cell Catalysis: A surface science approach*, Wiley, New Jersey and Canada, WILEY SERI., 2009.

142 J. Xu, D. Yuan, F. Yang, D. Mei, Z. Zhang and Y.-X. Chen, *Phys. Chem. Chem. Phys.*, 2013, **15**, 4367–76.

143 A. Cuesta, G. Cabello, M. Osawa and C. Gutie, *ACS Catal.*, 2012, **2**, 728–738.

144 Y. Chen, M. Heinen, Z. Jusys and R. J. Behm, *Langmuir*, 2006, **22**, 10399–10408.

145 M. Orio, D. A. Pantazis and F. Neese, *Photosynth Res.*, 2009, **102**, 443–453.

146 W. Gao, J. A. Keith, J. Anton and T. Jacob, *JACS*, 2010, **132**, 18377–18385.

147 C. Hartnig, J. Grimminger and E. Spohr, *J. Electroanal. Chem.*, 2007, **607**, 133 – 139.

148 I. Bako and G. Palinkas, *Surf. Sci*, 2006, **600**, 3809.

149 W. Gao, J. A. Keith, J. Anton and T. Jacob, *Dalt. Trans.*, 2010, **39**, 8450–8456.

150 N. R. Avery, *Appl. Surf. Sci.*, 1982, **11**, 774–775.

151 N. Avery, *Appl. Surf. Sci.*, 1983, **14**, 149–150.

152 M. R. Columbia and P. A. Thiel, *Surf. Sci.*, 1990, **235**, 53–55.

153 M. R. Columbia, A. M. Crabtree and P. A. Thiel, *J. Am. Chem. Soc*, 1992, **114**, 1231.

154 M. D. Macia´, E. Herrero and J. M. Feliu, *J. Electroanal. Chem.*, 2003, **554-555**, 25–34.

155 W. Gao, J. E. Mueller, Q. Jiang and T. Jacob, *Angew. Chem. Int. Ed.*, 2012, **51**, 9448 –9452.

156 H. Okamoto, *J. Phase Equilibria*, 1991, **12**, 207–210.

157 A. V. Tripković, K. D. Popović, R. M. Stevanović, R. Socha and A. Kowal, *Electrochem. commun.*, 2006, **8**, 1492–1498.

158 M. Yang, *J. Power Sources*, 2013, **229**, 42–47.

159 D.-J. Chen, Z.-Y. Zhou, Q. Wang, D.-M. Xiang, N. Tian and S.-G. Sun, *Chem. Commun. (Camb).*, 2010, **46**, 4252–4.

160 Y. Huang, S. Zheng, X. Lin, L. Su and Y. Guo, *Electrochim. Acta*, 2012, **63**, 346–353.

161 E. Casado-Rivera, D. J. Volpe, L. Alden, C. Lind, C. Downie, T. Vázquez-Alvarez, A. C. D. Angelo, F. J. DiSalvo and H. D. Abruña, *J. Am. Chem. Soc.*, 2004, **126**, 4043–9.

162 L. R. Alden, D. K. Han, F. Matsumoto, D. Abrun, F. J. Disalvo and N. York, 2006, 6667–6672.

163 X. Ji, K. T. Lee, R. Holden, L. Zhang, J. Zhang, G. a Botton, M. Couillard and L. F. Nazar, *Nat. Chem.*, 2010, **2**, 286–93.

164 X. Ji, K. T. Lee, R. Holden, L. Zhang, J. Zhang, G. a Botton, M. Couillard and L. F. Nazar, *Nat. Chem.*, 2010, **2**, 286–93.

165 S. Maksimuk, S. Yang, Z. Peng and H. Yang, *J. Am. Chem. Soc.*, 2007, **129**, 8684–5.

166 C. Song and J. Zhang, in *PEM fuel cell electrocatalysts and catalyst layers*, ed. J. Zhang, Springer London, London, 2008, pp. 89–134.

167 C. . Parkinson, M. Walker and C. . McConville, *Surf. Sci.*, 2003, **545**, 19–33.

168 A. V. Tripković, K. D. Popović, R. M. Stevanović, R. Socha and A. Kowal, *Electrochem. Commun.*, 2006, **8**, 1492−1498.

169 U. W. Hamm, D. Kramer, R. S. Zhai and D. M. Kolb, *Electrochim. Acta*, 1998, **43**, 2969−2978.

170 D. R. Blasini, D. Rochefort, E. Fachini, L. R. Alden, D. F. J., C. R. Cabrera and H. R. Abruña, *Surf. Sci.2*, 6AD, **600**, 2670−2680.

171 E. Bertin, S. Garbarino and D. Guay, *Electrochim. Acta*, 2014, **134**, 486–495.

172 E. R. Gonzalez and S. Srinivasan, *Electrochim. Acta*, 1983, **28**, 691–697.

173 A. Sáez, E. Expósito, J. Solla-Gullón, V. Montiel and A. Aldaz, *Electrochim. Acta*, 2012, **63**, 105–111.

174 A. S. Bauskar and C. Rice, *Electrochim. Acta*, 2013, **93**, 152–157.

175 A. López-Cudero, F. J. Vidal-Iglesias, J. Solla-Gullón, E. Herrero, A. Aldaz and J. M. Feliu, *J. Electroanal. Chem.*, 2009, **637**, 63–71.

176 T. Stanko, L. Tietze and E. Arch, 1992.

177 C. L. Bianchi, P. Canton, N. Dimitratos, F. Porta and L. Prati, *Catal. Today*, 2005, **102-3**, 203–212.

178 P. Fordham, M. Besson and P. Gallezot, *Catal. Letters*, 1997, **46**, 195–199.

179 Y. Kwon and M. T. M. Koper, *Anal. Chem.*, 2010, **82**, 5420–5424.

180 L. Roquet, E. M. Belgsir, J.-M. Léger and C. Lamy, *Electrochim. Acta*, 1994, **39**, 2387–2394.

181 J. F. Gomes and G. Tremiliosi-Filho, *Electrocatalysis*, 2011, **2**, 96–105.

182 W. Zhu, J. Ke, S.-B. Wang, J. Ren, H.-H. Wang, Z.-Y. Zhou, R. Si, Y.-W. Zhang and C.-H. Yan, *ACS Catal.*, 2015, **5**, 1995–2008.

183 Y. Choi and P. Liu, *Catal. Today*, 2011, **165**, 64–70.

184 a. Nirmala Grace and K. Pandian, *Electrochem. commun.*, 2006, **8**, 1340–1348.

185 M. M. S. Pupo, F. E. López-Suárez, A. Bueno-López, C. T. Meneses, K. I. B. Eguiluz and G. R. Salazar-Banda, *J. Appl. Electrochem.*, 2014, **45**, 139–150.

186 A. Zalineeva, A. Serov, M. Padilla, U. Martinez, K. Artyushkova, S. Baranton, C. Coutanceau and P. Atanassov, *JACS*, 2014, **136**, 3937–3945.

187 P. a. J. Bagot, K. Kruska, D. Haley, X. Carrier, E. Marceau, M. P. Moody and G. D. W. Smith, *J. Phys. Chem. C*, 2014, **118**, 26130–26138.

188 Y. Li, F. Hao, Y. Wang, Y. Zhang, C. Ge and T. Lu, *Electrochim. Acta*, 2014, **133**, 302–307.

189 Y.-N. Wu, S.-J. Liao, H.-F. Guo and X.-Y. Hao, *J. Power Sources*, 2013, **235**, 135–141.

190 G. Treglia, B. Legrand, F. Ducastelle, A. S. A, C. Gallis, I. Meunier, C. Mottet and A. Senhaji, *Comput. Mater. Sci.*, 1999, **15**, 196–233.

191 Y. Chen, S. Liao and H. Deng, *Appl. Surf. Sci.*, 2007, **253**, 6074–6079.

192 W. R. Tyson and W. A. Miller, *Surf. Sci.*, 1977, **62**, 267.

193 J. Emsley, *The elements*, Oxford University Press, New York, 2nd edn., 1991.

194 L. Vitos, a. V. Ruban, H. L. Skriver and J. Kollár, *Surf. Sci.*, 1998, **411**, 186–202.

195 J. Luyten and C. Creemers, *Surf. Sci.*, 2008, **602**, 2491–2495.

196 S. Alayoglu, A. Nilekar, M. Mavrikakis and B. Eichhorn, *Nat Mater*, 2008, **7**, 333–338.

197 M. Avramov-Ivic, J.-M. Léger, B. Beden, F. Hahn and C. Lamy, *J. Electroanal. Chem.*, 1993, **351**, 285–297.

198 R. M. Waterstrat and H. Foundation, 1981, **80**, 31–36.

199 P. T. Moseley and C. J. Seabrook, *Acta Crystallogr. Sect. B*, 1973, **29**, 1170–1171.

200 G. Couturier and D. W. Kirk, 1985.

201 J. Masud, M. T. Alam, Z. Awaludin, M. S. El-Deab, T. Okajima and T. Ohsaka, *J. Power Sources*, 2012, **220**, 399–404.

202 J. M. Gregoire, M. E. Tague, S. Cahen, S. Khan, H. D. Abruña, F. J. DiSalvo and R. B. van Dover, *Chem. Mater.*, 2010, **22**, 1080–1087.

203 E. Toyoda, R. Jinnouchi, T. Ohsuna, T. Hatanaka, T. Aizawa, S. Otani, Y. Kido and Y. Morimoto, *Angew. Chemie - Int. Ed.*, 2013, **52**, 4137–4140.

204 Y. Garsany, A. Epshteyn, A. P. Purdy, K. L. More and K. E. Swider-Lyons, *J. Phys. Chem. Lett.*, 2010, **1**, 1977–1981.

205 O. a. Baturina, Y. Garsany, T. J. Zega, R. M. Stroud, T. Schull and K. E. Swider-Lyons, *J. Electrochem. Soc.*, 2008, **155**, B1314.

206 C. Burda, X. Chen, R. Narayanan and M. a El-Sayed, *Chemistry and properties of nanocrystals of different shapes.*, 2005, vol. 105.

207 E. E. Benson, C. P. Kubiak, A. J. Sathrum and J. M. Smieja, *Chem. Soc. Rev*, 2009, **38**, 89.

208 H. Liao, A. Fisher and Z. J. Xu, *Small*, 2015, **11**, 3221–3246.

209 A. Agbabiaka, M. Wiltfong and C. Park, *J. Nanoparticles*, 2013, **2013**, 1–11.

210 I. Dutta, M. P. B. Michael K Carpenter and M. H. A. N. P. I. Joseph M Ziegelbauer, Thomas E Moylan, *J Phys Chem C Nanomater Interfaces*, 2010, **114**, 16309–16320.